Performance of Composite Material and Composite Structures to Attenuate Dynamic Loads

A Dissertation

Presented in Partial Fulfillment of the Requirements for the

Degree of Doctor of Philosophy

with a

Major in Civil Engineering

in the

College of Engineering

University of Idaho

by

Mahmoud Mohamed Mahmoud Mohamed

Major Professor: Ahmed Ibrahim, Ph.D.

Committee Members: Richard J. Nielsen, Ph.D., S. J. Jung, Ph.D.,

Ay. Suat, Ph.D.

Department Chair: Fritz R. Fiedler, Ph.D.

August 2021

Authorization to Submit Dissertation

This dissertation of Mahmoud Mohamed Mahmoud Mohamed, submitted for the degree of Doctor of Philosophy with a Major in Civil Engineering and titled "Performance of Composite Material and Composite Structures to Attenuate Dynamic Loads," has been reviewed in final form. Permission, as indicated by the signatures and dates below, is now granted to submit final copies to the College of Graduate Studies for approval.

Major Professor: _____   Date: _____
             Ahmed Ibrahim, Ph.D.

Committee Members: _____   Date: _____
             Richard J. Nielsen, Ph.D.

                              _____   Date: _____
             S. J. Jung, Ph.D.

                              _____   Date: _____
             Ay. Suat, Ph.D.

Department
Chair: _____   Date: _____
             Fritz R. Fiedler, Ph.D.

Abstract

Protecting structures against accidental or intentional blast events is a sophisticated task in structural engineering. If vital civilian critical structures (buildings, bridges, embassies, etc.) are threatened, the main concern lies in developing an effective rescue plan and rapid intervention. The integrity of the structure itself is rarely considered. However, explosion events devasting civilian buildings and structures have been increased during the last few decades (bomb attacks World Trade Centre (1993), Oklahoma (1995), US embassy Kenya (1998), sugar factory explosion in Georgia (2008), Beirut (2020)), to name a few. Consequently, shielding structures against blast hazards has become an active area for research for many years. Numerous efforts were devoted to suggesting appropriate solutions to this problem. Among these solutions, sandwich panels providing a quite promising approach for blast mitigation techniques for their high strength, lightweight, and superb energy absorption capabilities compared with single metallic plates with equivalent weight.

Sandwich panels typically have three layers; two outer plates made of metals or composite materials and a core layer in-between. The plate facing blast wave distributes the blast pressure uniformly across the core layer, which progressively deforms and absorbs a large amount of blast energy, thus the pressure transferred to the structure is attenuated. The efficiency of these sacrificial layers depends mainly on the quantity of energy absorbed by their core. This research aimed to improve the blast performance of sandwich structures by introducing novel core layers that can absorb an enormous amount of energy.

This research presents an innovative energy absorbing component applicable to energy absorption applications. The developed structure comprises a superposition of two different energy absorption techniques to enhance the energy absorption capacity of a novel core structure. The proposed core structure can be applied to extensive blast-resistant and crash-worthiness applications. Thus, experimental and numerical investigations have been conducted to investigate the influence of applying internal stiffeners and wrapping composite layers on the behavior of aluminum (AL) thin-walled tubes. Single, double, and quadruple thin-walled metallic and hybrid tubes were tested under axial quasi-static compression test. The specimens were fabricated from unidirectional CFRP, epoxy resin, and aluminum alloy T6061-T6. Various crashworthiness parameters were assessed, such as the absorbed crash energy, specific energy absorption, crush force efficiency, average crushing load, and peak load absorbed to highlight the effectiveness of the novel configurations.

The hybrid quadrable multi-cell structure showed the highest energy absorption capabilities compared to the other proposed configurations. Its energy absorption improved by 116% compared to the solo hollow AL tube.

In addition, nonlinear finite element analysis (FEA) using the commercial ANSYS/LS-DYNA Workbench software was utilized to verify the experimental results. Numerical simulations show a proper verification with the experimental results as the discrepancy percentage for the energy absorption varied between 4.14 to 10.69 and 3.41 to 8.30 for the peak crushing force. So, it is impressive to adopt the novel energy absorbers components in a sacrificial cladding structure to enhance the blast performance of reinforced concrete panels.

This research also presents a new core topology for sandwich structures named ribbon core configuration. The purpose of this configuration is to provide a sandwich structure with the following advantages: very light, less expensive, simple to manufacture, great flexibility, and the ability to construct curvature in two directions. The dynamic performance of the new shape numerically investigated for metallic sandwich structure panels exposed to blast loading. The FE models' accuracy was verified using experimental results that can be accessed in the literature that used trapezoidal corrugated core configurations. Results indicate that the conducted finite element models are effective to simulate the dynamic behavior of structures subjected to blast loading. The ribbon-core sandwich panel (RCSP) blast behavior and the trapezoidal corrugated-core sandwich panel (TCCSP) were compared. The results imply that RCSP experienced superior blast resistance than the TCCSP. Findings were used as a guideline for designing sandwich structures under the impact of blast loading.

Acknowledgements

I would like to express my deep thanks and sincere appreciation to Dr. Ahmed Ibrahim for being my mentor throughout the planning and enhancement of this thesis. Dr. Ahmed was eager to provide support and encouragement with patience for me during my research period. Without his endless guidance and constructive advice, this work would not have been accomplished. It is a great honor for me to be his Ph.D. student. This experience enhanced my experience, knowledge and was an amazing success story in my educational journey. I sincerely wish Dr. Ahmed every success in his life and career endeavors.

I would also like to extend my thanks to the respectable committee members, Dr. Richard Nielsen, Dr. S.J. Jung, and Dr. Ay. Suat for being part of my esteemed committee and for providing me with their valuable comments and feedback for improving my work's quality.

I lovingly would like to extend my truly grateful to my parents. Without their love, dedication, endless support, and prayers, it would have been impossible to achieve so much in my life. Last but not least, truly unbounded thanks are due to my generous wife for her continuous support, encouragement, and being patient in difficult times. I would also like to sincerely apologize to my son because for being busy at work all the time, and I hope he appreciates it one day that this was for the good of us all.

Also, special thanks to Dr. S.J. Jung and Don Parks for their technical supports. Without their help and constant support, it would not be possible for me to execute the experimental program.

I greatly appreciate all the support provided by the Department of Civil and Environmental Engineering at the University of Idaho to complete this research. I expand my thanks and appreciation to the University of Idaho for the support it provided for this research through its facilities and gave me the opportunity to pursue my graduate studies and realize my dream.

Finally, I am really grateful to my professors in Egypt, Prof. Sherif Mazek and Dr. Sameh Ahmed were very supportive during my thesis and continue to support me during my Ph.D. trip. They are always ready to transfer his deep knowledge and experience to me wherever needed.

Dedication

This dissertation is dedicated to my beloved parents, my beloved wife, and my beloved son

Ryan; they were and will always be my greatest support in life.

Table of Contents

List of Figures

List of Tables

Nomenclature

Symbols

AL	Aluminum
CFRP	Carbon fiber reinforced polymer
P_o	Atmospheric pressure
P_s^+	Maximum positive overpressure
P_s^-	Maximum negative pressure
T^+	Positive time duration
T^-	Negative time duration
P_{so}	Peak overpressure
t_a	Time of arrival
ρ	Density
μ	Poisson's ratio
E	Young's modulus
σ_{y0}	Initial yield stress
σ_u	Ultimate tensile strength
P	Load
Δ	Displacement
m	Mass
P_{avg}	Average crushing load
δ	Post-crushing displacement
E_c	Absorbed energy in the post-crushing zone
σ_n	Normal stress
σ_s	Shear stresses
E_1	Young's modulus X direction
E_2	Young's modulus Y direction
E_3	Young's modulus Z direction
ν_{12}	Poisson's ratio XY
ν_{23}	Poisson's ratio YZ
ν_{13}	Poisson's ratio XZ
G_{12}	Shear modulus XY
G_{23}	Shear modulus YZ
G_{13}	Shear modulus XZ

X_T	Axial tensile strength
X_C	Axial compressive strength
e	Internal energy
$\boldsymbol{\gamma}$	Ideal gas constant
T	Temperature

X_T Axial tensile strength

X_C Axial compressive strength

e   Internal energy

$\boldsymbol{\gamma}$ Ideal gas constant

T   Temperature

xvi

Abbreviations

AL	Aluminum
CFRP	Carbon fiber reinforced polymer
T6061-T6	Aluminum alloy
TNT	Trinitrotoluene
FEA	Finite element analysis
RCSP	Ribbon-core sandwich panel
TCCSP	Trapezoidal corrugated-core sandwich panel
GLARE	Glass laminate aluminum reinforced epoxy
FML	Fiber metal laminate
TW	Thin walled
Al-SCT	AL single-cell tube
Al-DCT	AL double-cell tube
Al-QCT	AL quadruple-cell tube
H-SCT	Hybrid single-cell tube
H-DCT	Hybrid double-cell tube
H-QCT	Hybrid quadruple-cell
MTS	Material testing machine
EA	Energy absorbed
SEA	Specific absorption energy
CFE	Crush force efficiency
CCRIT	Critical distance
SoD	Standoff distance

Chapter 1: Introduction

1.1 Problem statement

Usually, common structures were not prepared to withstand explosion threats, so it is imperative to design and retrofit structures against blast loads. A few of the available solutions for protecting structures from blast hazard are as follows:

a) Containment of steel structures is with a thick concrete covering layer. This approach has many flaws, such as a large deadweight added to the structure. In addition, explosion tests showed that concrete completely pulverizes and causes casualties due to fragmentations [6].

b) LINE-X or POLYUREA is used to coat the internal walls of a structure. This technique is very expensive.

c) Another alternative is glass laminate aluminum reinforced epoxy (GLARE), which is a fiber metal laminate (FML) consisting of several very thin layers of metal (usually aluminum) combined with layers of composite materials (usually prepreg glass-fiber), glued together with a matrix such as epoxy. It provides very good resistance against impact, blast loading, and fire [7]. However, the material is very expensive.

d) Finally, nanomaterials have a significant function in the blast mitigation of concrete. However, producing nanomaterial is a very expensive process, and the quantities required for the construction industry are massive.

Recently, sacrificial cladding structures have attracted more attention as effective blast mitigation systems due to their superior energy absorption capabilities and low cost [8-10]. These cladding structures can alleviate blast loads and lessen the potential damage of the structure by reducing the impulsive force level and increasing the duration of the pulse.

The idea of sacrificial cladding structures is to convert a high blast load with short-duration impulse into a low load with long duration pulse, thus reducing the potential damage of the non-sacrificial structure which was installed on it. The mechanism of a cladding structure is to absorb energy through plastic deformation of its inner core layer. In order to achieve this, the failure load of the sacrificial cladding structure must be less than the failure load of the critical structural elements of civil engineering structures. Maintaining a low failure load to the inner core may be attributed to achieving plastic deformation/brittle failure during an explosion, and thus the peak force transmitted to the civil engineering structures can be minimized.

The current study investigates the failure mechanisms and the corresponding absorption energy of crushable metallic and hybrid multi-cell tubes under the effect of an axile quasi-static compressing test. It also extended to cover the dynamic performance of lightweight sandwich structures under the effect of blast load and introduces new efficient core systems for sandwich structure panels to resist blast loads. Various factors such as their lightweight, fast installation and ease of handling, high-strength lightweight structures, and decent thermal insulation properties were also considered.

Deflection and energy dissipation are the two output considered in this study. The mid span deflection used to assess the failure of the panels. Accordingly, the deflection is the primary factor that controls the design of such panels, and mainly, the deflection of the back layer as it acts as the last shield that protects occupants from blast waves [11]. Also, energy absorption is another important factor that was investigated. The target is to achieve maximum energy absorption with a minimum failure level represented by deflection.

1.2   Research Significance

The last few years have witnessed a growth in the number of accidental or intentional blast events that threaten civilian and military structures. Blast hazards lead to massive losses of lives and equipment. Blast protection and energy absorption structures have received considerable interest from military and civilian research organizations [12]. Protecting people and structures has become a significant engineering challenge. Consequently, blast mitigation of structures has become inevitable for many industrial, governmental, and military organizations. In several industries, such as cement production, coal mining, and petrochemical fields, the consequences of accidental explosions should be carefully considered. For example, in the petrochemical field, man-made accidents that occur in industrial facilities could trigger explosions that are accompanied by other phenomena such as fire and impact caused by explosion-borne missiles [13].

The governmental and military organizations use maneuverable blast walls to shield their buildings against blast loads. Maneuverable walls provide a reflective coat of blast waves that mitigate the blast impact on structures. For blast shielding, maneuverable walls are constructed around structures as the first line of defense, increasing stand-off distance. Many facilities also places blast-resistant checkpoints at their entrances or around the facility to control access. Lightweight prefabricated moveable structures can provide a robust, durable, and reliable replacement of the traditional sandbag bunkers used for temporary

checkpoints. Sandwich panels are being used to manufacture light-weight moveable structures [14].

Energy absorbers are also essential for crashworthiness design. Crashworthiness is the ability of a structure to absorb a large amount of energy and convert it into plastic strain energy when it deforms under pressure resulted from impact events. Thin-walled (TW) structures with different materials and geometries have been exploited as energy absorbers in crashworthiness applications [15].

1.3   Research objectives

The aim of this research is to develop an effective blast-resistant systems using lightweight composite structures. The findings from this research can be generalized, providing implementations in several other potential structural applications.
 Therefore, the objectives of this study are:

- Design a novel thin-walled structure with high energy absorption capabilities that could be used as a new inner core for sacrificial cladding structure.
- Assess the crashworthiness of the proposed novel energy absorber structure through experimental work.
- Investigate the blast performance of protected structures by applying sacrificial cladding structure with hybrid multi-cell tubes as an effective absorbing core.
- Develop a high-fidelity numerical model for various blast environments using the explicit finite element program (Autodyn/ANSYS), and compare and validate results with the field test results.
- Investigate various blast parameters on the performance of the novel sandwich structures and provide guidance for its design.

1.4   Contributions

In the current study, the proposed tubes indicated that the novel technique is effective for improving the energy absorptions capabilities of thin-walled structures. The new energy absorber structure can be operated standalone in crashworthiness application such as:

- A safety device attached to the front of the vehicles' hull and chassis of trains.
- As energy absorption tube in aircraft fuselage.

- Moreover, it can be used as a sacrificial cladding system for critical governmental structures. The proposed system (inner core) will enhance its non-linear dynamic behavior under the severe blast loading by dissipating energy and reducing deflection.

The proposed system showed that the impulse resistance is better than the traditional corrugated sandwich structures. The application of sandwich panels examined in this study are:

- Maneuverable checkpoints (instead of sandbags used nowadays),
- Protection wall panels which can be placed in front of any construction that must be safeguarded from blast events,
- Constructing moveable buildings against blast effect like in the gas and oil industry and military buildings like barracks and ammunition stores.
- Main structural components for military vehicles, and ship hulls.

1.5   Research Overview

This dissertation presents research work carried out towards the objectives above. The entire dissertation consists of six chapters, including this chapter.

Chapter 2 introduces the fundamentals of blast loading, the method used to predict blast loads, and a general review of the response of structures imperiled to blast loads. It is followed by discussion of the various types of composite material and the composite structures used to resist blast load. A historical review of the various retrofitting systems and protection of structures has also been conducted.

Chapter 3 introduces a novel technique to develop effective energy-absorbing structures. The new structures were hybrid multi-cell thin-walled circular tubes. Three novel configurations were introduced in this chapter. Experimental tests were executed to assess the energy absorption capabilities of the new core system. Besides, an intensive numerical study was performed to model the experimental tests utilizing commercial finite element software, LSDYNA/Workbench.

Chapter 4 applies the novel structures as blast mitigation layers in reinforced concrete elements, mainly RC slabs. Sacrificial cladding structures were attached to the RC slabs as a protection layer from the destructive effect of close-range explosions. Due to the difficulties encountered in running the blast field tests, validated available experimental test data were used to verify the 3D FEMs. The hydro-code program (AUTODYN), endorsed by the finite element program (ANSYS) has the capability to simulate explosions, and analyze

blast wave interactions. The results showed the effectiveness of using the novel sacrificial structures in protecting concrete structures.

Chapter 5 numerically investigates the use of ribbon shapes as an innovative core topology for sandwich structures subjected to blast loading. Applying the ribbon topology to the traditional corrugated core topologies improved their blast performance. Also, this chapter provides recommendations that can be utilized as a guide manual for designing metallic ribbon sandwich structures with different protection levels.

Finally, Chapter 6 offers conclusions of this study and recommendations for future works.

1.6   Dissemination of the Work Described in this study

Some of the findings from this research have been prepared for dissemination and presentation in the following peer-reviewed journals and conferences:

"Hybrid Multi-Cell Thin-Walled Tubes for Energy Absorption Applications: Blast Shielding and Crashworthiness"

Journal: Composites Part B

Corresponding author: AHMED IBRAHIM

First author: Mahmoud Mohamed

Published: 15 Feb 2020

"Metallic Ribbon-Core Sandwich Panels Subjected to Air Blast Loading"

Journal: Advances on Structural Engineering, Applied sciences, MDPI

Corresponding author: AHMED IBRAHIM

First author: Mahmoud Mohamed

Published: 29 June 2020

"Impact of Blast Hazard on Metallic Sandwich Structures" . Mahmoud Abada, Ahmed Ibrahim. 7th International Conference Integrity-Reliability-Failure.

J.F. Silva Gomes and S.A. Meguid (editors), INEGI-FEUP (2020).

"Improving Blast Performance of Reinforced Concrete Panels using Sacrificial Cladding with Hybrid-Multi Cell Tubes"

Journal: Advances in Structural Mechanics and Finite Element Modelling, Modelling, MDPI

Corresponding author: AHMED IBRAHIM

First author: Mahmoud Mohamed

Third author: SJ Jung

Chapter 2: Literature Review

Dynamic load on structures could be generated from various sources, for instance, mechanical activities (a structure that was supporting rotating machinery), wind, earthquake, high-speed impacts, and explosions (blast). Most of these loading conditions are covered by modern design (loading) codes (European Committee for Standardizations, 2006, American Society of Civil Engineers, 2002, Standards Australia, 2011). However, all principal design codes have paid limited attention to explosive loading due to the scarcity and extreme nature of the loading. The United States Army Corps of Engineers has published a series of comprehensive blast design guidelines for constructing military and storage facilities focusing on explosions [1].

The whole world suffers from explosion events that deliberately or accidentally damaged industrial, civilian, and military structures. These events have raised serious concerns about countries' ability to protect their people and structures from these persistent threats. Hence, there is an urgent demand for analyzing and design structures subjected to such tragic events to withstand harsh loading conditions. A blast load analysis must be conducted to anticipate the behavior of structure imperiled to blast loads. The blast parameters, types of blast loads, and their effects on structures are covered in this chapter. It is not economical to fortify structures to endure blast loads. Therefore, some of the strategies that could be adapted to alleviate the influence of blast hazards were also investigated. Also, the various approaches for anticipating blast loads are discussed. This chapter presents the fundamentals of blast for structural engineers and researchers.

2.1   Blast Phenomena

An explosion is a rapid expansion in volume due to an abrupt energy release in an intense manner, usually accompanied by high temperatures, pressures, and the release of gases in a short time [1]. The explosion can be categorized as physical, nuclear, or chemical depending on its cause. For physical explosions, energy is discharged from either failure of compressed gas cylinder, volcanic eruptions, or mixing of two liquids at different temperatures. In the case of nuclear explosions, energy is released due to the splitting of atomic nuclei by redistributing neutrons and protons inside the interacting nuclei. While the main reason for energy release in a chemical explosion is the instant oxidation of the fuel elements (hydrogen and carbon particles)[2].

Explosives can be grouped as gases, liquids, or solids. Explosives are also characterized according to their detonation sensitivity for primary and secondary explosives. Primary explosives can be quickly initiated with the minimal energy from a spark or impact. Lead azide and mercury fulminate are primary explosives. Secondary explosives require a more significant amount of energy compared to the primary explosive. The secondary explosive usually requires a primary explosive as a detonator to initiate the explosion. Trinitrotoluene (TNT) is a secondary explosive. Secondary explosives can be more dangerous and can cause widespread damage to surrounding infrastructures due to their quantities in storage and transport [3].

It is crucial to understand the mechanism of blast loading [4]. The blast load is created when the explosion causes the surrounding air mass to move, producing a high-velocity shock wave, as shown in Fig. 2.1 that travels in radial directions from the center of detonation. Blast loads create hundreds of times more stress than wind loads. Although blast loads have incredibly high peak pressures, the durations are extremely short. Short-duration loads reduce the impacts of such high pressures on structures. Nearby building will experience a short-term load in the form of a pulse (pressure embedded in time). The severity of this impulse depends on the following factors:

- Distance from a target (stand-off distance)
- The size of the explosive charge
- Type of wave propagation
- Open or enclosed area
- Geometry of structure (an incidence angle of 0° causes the highest load case)

Fig. 2.1: Generated shock wave due to explosion.

2.1.1   Explosions Types

Explosions are either confined (inside the structure) or unconfined (outside the structure). The confined explosion is divided into fully vented, partly vented, and totally confined, as displayed in Fig. 2.2. A fully vented bursts happen when one or more surfaces are open to the air. Accordingly, the pressure from the blast wave is sent directly into the atmosphere. For partially confined eruptions, the structure contains the explosion for a limited period before being released into the atmosphere due to the presence of a small aperture in the structure. For entirely confined explosion, the explosion is trapped within the structure. Consequently, the blast waves are reflected and amplified, creating an accumulated gas pressure [5].
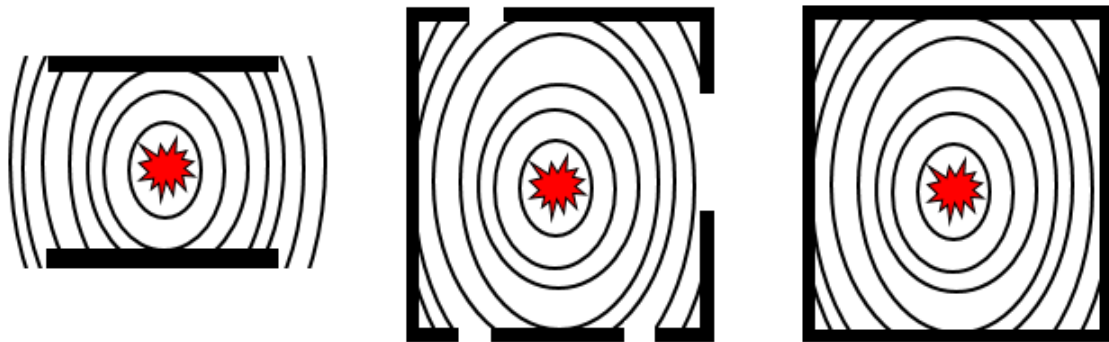
Fig. 2.2: Types of confined explosions: a) totally vented, b) partially confined, c) totally confined.

Unconfined blast loads are divided into surface burst (hemispherical surface burst), airburst, and free air burst (spherical Surface blast). Unconfined eruptions occur when the blast waves propagate from the detonation source towards the structure due to the ignition of an explosive charge in an open area. A free explosion occurs when the shock wave produced by the detonation propagates away from the source and strikes the structure just before the reflection wave occurs. For a blast in the air, the detonation occurs at a distance from a structure that allows the blast wave to be reflected off the ground before reaching the structure. Finally, with surface explosions, the detonation occurs near the ground, and the primary shock wave is amplified at this stage by shock wave reflections from the ground [5]. Figure 2.3 shows the three categories of unconfined blast loading: free air blast, air blast, and surface burst. This study deals in detail with unconfined blast loads.
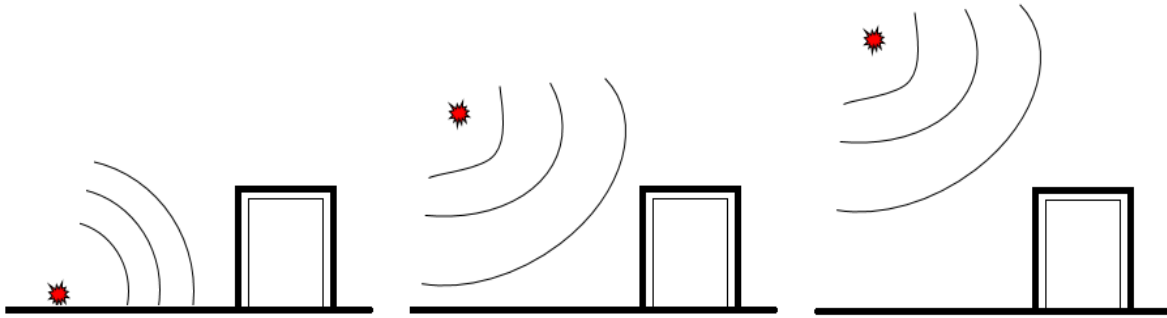
Fig. 2.3: Blast loading categories: a) surface burst, b) airburst, c) free air burst.

2.1.2 Standoff distance

The direct, unimpeded distance between the facing surface of the target and the center of the charge weight is expressed by standoff distance (*SoD*) and is illustrated in Fig. 2.4. It plays an important role in blast mitigation, as when it is increased, the intensity of the blast overpressure of the explosion decreases [6, 7]. *SoD* can be established by appropriate fencing, knee walls, and access control point to protect vital buildings [8, 9].
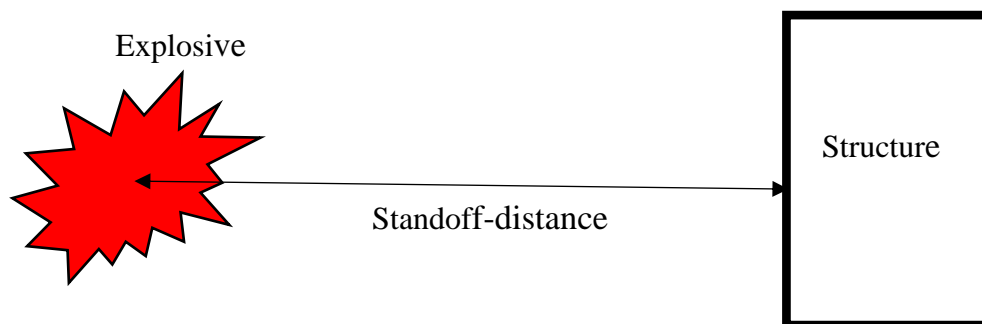
Fig. 2.4: Schematic of standoff distance.

2.1.3 TNT equivalence

The diversity of explosive materials leads engineers to adopt a global quantity that is used in all calculations of explosion strength. TNT was selected because its blast properties are similar to those of most solid explosive types. TNT equivalent weight is calculated by Equation (2.1) which relates the chosen design explosive weight to the corresponding TNT weight by taking advantage of the generated heat percentage:

$$W_e = W_{exp} \frac{H_{exp}^d}{H_{TNT}^d} \qquad\qquad (2.1)$$

Where, W_e is the equivalent TNT weight (kg),

W_{exp} is the actual weight of the explosive (kg),

H_{exp}^d is the detonation heat for the actual explosive (MJ/kg), and

H_{TNT}^d is the TNT detonation heat (MJ/kg)

Table 2 lists some of the pre-determined equivalent weight factors of TNT. These factors can be utilized to calculate the weight of the TNT charge that generates the same blast wave parameters as those produced by another explosion of a certain weight. A comparison of these parameters can be made for either pressure or pulse values; Thus table 2.1 encloses three different factors for distinctive types of explosives.

Table 2.1: TNT equivalent factors [10].

Explosive	Detonation heat (KJ/kg)	Equivalent mass factor	
		Pressure	Impulse
TNT	4.247	1.00	1.00
RDX	6.19	1.14	1.09
HMX	2.175	1.02	1.03
AMATOL	2.931	0.99	0.98
PETN	6.69	1.27	1.11
C4	5.86	1.37	1.19

2.1.4   Blast Wave Parameters

The blast loading is evaluated either by primary or secondary parameters (Overpressure, impulse, and duration are primary parameters for calculating the blast load. While the peak dynamic pressure, peak reflected pressure, and the blast wavelength are the secondary parameters). The secondary parameters are obtained from the primary parameters. Figure 2.5 displays an ideal blast wave pressure-time history [2]. It involves two stages; the positive pressure (pushing) phase, where incident pressure rises at the wavefront from

ambient pressure (P_o) to peak overpressure (Ps_o) at the time of arrival (t_a). Then follows by exponential decay until the pressure drops down to ambient pressure at the time of ($t_a + t_d$). The second phase is known as the negative (suction) phase, where pressure decrease until a negative peak pressure (P_{so}^-) at the time of (ta + t$_d$+ t$_d^-$). Typically, the duration of the pressure wave is relatively very short, for that the structure component response is mainly affected by the positive impulse which is the area under the time-pressure curve.
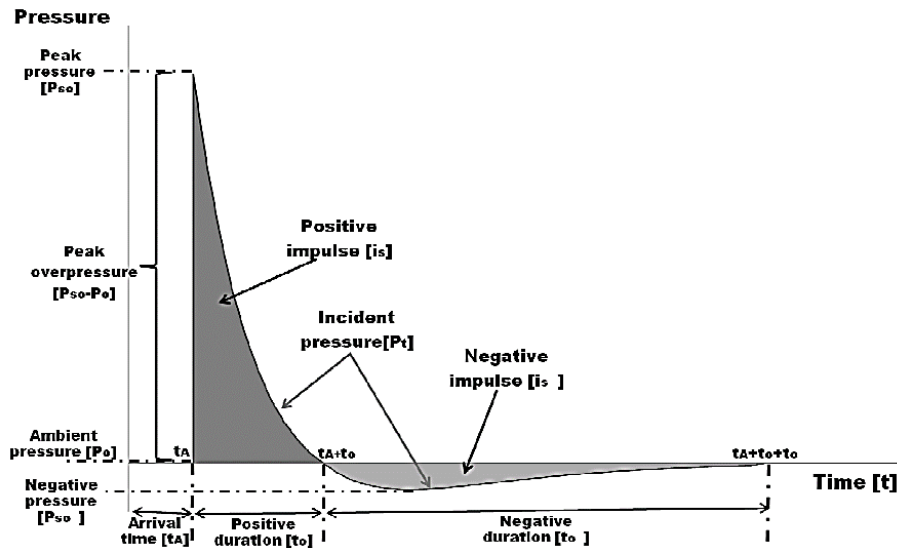
Fig. 2.5: Ideal blast wave pressure-time history.

The negative phase is usually neglected during the blast design as it has been demonstrated that the positive phase is responsible for the primary structural damage. Furthermore, pressures due to the negative phase are relatively small compared to the positive phase pressures. The negative phase does not have much influence on the integrity of buildings exposed to explosions. Even though the value of these pressures is less than the ambient pressure, they are taken into account in the overall structural performance of the building during an explosion rather than in terms of assessing its structural integrity.

The positive phase is usually described by Friedlander's equation [11], which is expressed as:

$$P(\text{t}) = P_{\text{so}}(1 - \frac{t}{t_\text{d}})e^{-\text{b}(\text{t}/t_\text{d})} \qquad (2.2)$$

Initially, atmospheric pressure is not considered during the blast pressure calculation. Therefore, this equation is further modified considering ambient atmospheric pressure and became,

$$P(\text{t}) = P_0 + P_{\text{so}}(1 - \frac{t}{t_\text{so}})e^{-\text{b}(\text{t}/t_\text{so})} \qquad (2.3)$$

This equation is known as the modified Friedlander equation and is widely used due to its accuracy. The other most widely used approach to obtain the blast pressure (Pt) was developed by Kingery et al. [12]. The equation takes the form,

$$P_t = P_r\cos^2\theta + P_i(1 + \cos^2\theta - 2\cos\theta) \tag{2.4}$$

The impulse is another essential parameter for assessing the blast load. The area describes it beneath the pressure-time curve. The impulse is divided into positive impulse i_s^+ and negative impulse i_s^- calculated by the following equations [13-15].

$$i_s^+ = \int_{t_a}^{t_a+t_d} P_{so}(t)\, dt \tag{2.5}$$

$$i_s^- = \int_{t_a+t_0}^{t_a+t_d+t_d^-} P_{so}^-\, dt \tag{2.6}$$

2.1.5 Blast Scaling Laws

In blast analysis, scaling laws are developed to model the blast wave parameters of large-scale explosions by using a small-scale explosion. There are many ways to scale blast parameters, but the most used is the Hopkinson scaling law. It states that "blast waves generated from the detonation of different charge weights of the same type and geometry of an explosive detonated with equal scaled distance *(z)* are similar". To simplify, if a charge with weight (W) and diameter (d), is detonated at a distance (R), the blast wave parameters: peak pressure (P_{SO}), impulse (I_S), and phase duration (t_d), will be the same for an explosive charge weight (W_1), with a diameter (d_1), detonated at a distance (R_1).

The relation between any two kinds of explosives can be expressed as follows:

$$W \propto d^3 \text{ and } W_1 \propto d_1{}^3$$

Where d and $d1$ are the diameters of the spherically shaped explosive charges, from this relation:

$$\frac{W}{W_1} = \left(\frac{d}{d_1}\right)^3 \text{and} \frac{d}{d_1} = \left(\frac{w}{w_1}\right)^{\frac{1}{3}} \tag{2.7}$$

A dimensional scaled distance (Z) is introduced as described by the following equation. As the constant Z increases, the charge weight decreases, generating smaller incident pressure at the identical stand-off distance.

$$\frac{R}{R_1} = \left(\frac{w}{w_1}\right)^{\frac{1}{3}} \Rightarrow \frac{R}{W^{1/3}} = \frac{R_1}{W_1^{1/3}} = \text{constant} = Z \tag{2.8}$$

where W is the equivalent TNT charge weight (kg), and R is the range (*SoD*) in meters (m) [16].

2.2   Methods used to predict blast wave parameters

The methods used for calculating the blast wave parameters are theoretical, empirical (analytical) method, and computational techniques.

2.2.1   Theoretical and Empirical Methods

The earliest records of blast pressure discoveries date back to 1870, when Rankine and Hugoniet described the normal shocks in ideal gases. Over many years, because of research associated with test programs, a number of analytical methods have been developed for predicting blast loading. Table 2.2 listed most of the analytical methods capable of predicting the blast wave parameters. These analytical techniques are introduced in many design manuals, for instance, TM 5-1300 and TM5-855-1. The US Army has established these manuals and used it for military and civilian sectors to design structures against blast loads. It contains a step-by-step analysis and design procedure. The design curves in these guides express the blast load parameters as functions of the measured scaled distance (Z) based on TNT equivalent weights. We can use charts to calculate all aspects related to the blast wave (shock wave). These charts use a reference yield of 1 kiloton (KT) or 1 megaton (MT). We can get these parameters for another yields using the scaling law. These manuals are commonly used as engineering references for predicting blast loads on the surface and buried structures.

Table 2.2: Summary of studies on blast pressure estimation

Researcher	Year	Type of Blast	Method
Von Neumann and Bethe	(1947)	Spherical free air	Theoretical
Brode	(1955)	Spherical free air	Theoretical
Newmark and Hansen	(1961)	Hemispherical	Empirical
Henrych and Major	(1979)	Spherical free air	Semi-empirical
Kingery and Bulmash	(1984)	Spherical free air and hemispherical	Empirical
Mills	(1987)	Hemispherical	Empirical

2.2.2   Computational Techniques

The previous analytical techniques have been automated in the computer programs such as CONWEP, RCBLAST, AIR3D, and BlASTX [17]. These programs are distributed through the governmentally controlled Defense Logistics Agency that monitors and controls access to these programs due to the classified material they contain. By developing computer science, numerical methods contribute to the structure design and are capable of predicting both the blast parameters and the structural response to the blast loading. These methods will be covered in detail in the following sections.

2.3   Structure response to blast loading

Analysis of the dynamic behavior of explosion-loaded structures comprises the influence of extreme strain rates, the behavior of inelastic nonlinear materials, uncertainties in blast load computations, and time-dependent deflections. Several reasonable assumptions regarding the response and loads of the structure have been proposed and widely accepted to estimate the response of structures against blast loading. An equivalent single degree of freedom (SDOF) system is used to idealize the dynamic performance of the structure, then the equation of motion is solved analytically or numerically to obtain a displacement-time history of the structure. However, this approach is based on numerous assumptions as the load and structure configuration are complicated. The discrepancies compared with the experiments may be large and may not be appropriate when more detailed information related to failure is required. Finite element models (FEM) can be used to examine the structural response due to blast loads in a more rigorous fashion [18]. The FEM considers the material geometry, dynamic properties, and nonlinearity. Numerical methods used to simulate the blasted problem typically are based upon explicit finite element methods.

2.4   Modelling Techniques

In the past few years, numerical simulations have been replaced the blast field tests in the structure design. The entire explosion event can be accurately analyzed, and the dynamic structural response can be captured utilizing finite element analysis (FEA). It is challenging to solve such problems with thousands of time steps due to the complexity of inverting stiffness matrices to solve large groups of nonlinear equations, especially for models with enormous number degrees of freedom nonlinearity is present. Explicit FEM

overcomes this because it solves problems without creating a global stiffness matrix. The explicit approach can solve large 3D models in a reasonable computational time.

Moreover, the ease of implementation and the ability to model highly nonlinear mechanical phenomena are significant advantages for this approach. Nonlinearities may occur due to the materials, contact (the interface between the load and the structure and the internal elements of the structure), and the structural deformation (buckling and collapse). Besides, the explicit approach solves through relatively small-time steps to capture the detailed structure response during time-dependent loading with maintaining consistency and stability (AUTODYN, 2014). Various software programs perform explicit dynamic analyses, (e.g., ABAQUS, LS-DYNA, AUTODYN, ANSYS AUTODYN, etc.) are available and can simulate the structure's performance under blast loading. These programs combine different techniques (finite and discrete element method) to precise failure and crack patterns of blast-loaded structures [19].

Additionally, there is an interaction between the blast wave and the target structure called fluid structure interaction (FSI). Lagrangian, Eulerian, and Arbitrary Lagrange–Euler (ALE) solvers [20] are used to simulate this kind of interaction. The Lagrange solver is employed for solid continua modeling (e.g., structure); however, the Euler solver is commonly adopted for fluids and gases modeling (e.g., air blast, underwater explosions). Lagrange solvers break the structure into small parts connected by nodes that move as the material distort, as shown in Fig .2.6 a. Euler solvers use a fixed grid in space through which materials can flow, as shown in Fig .2.6 b.
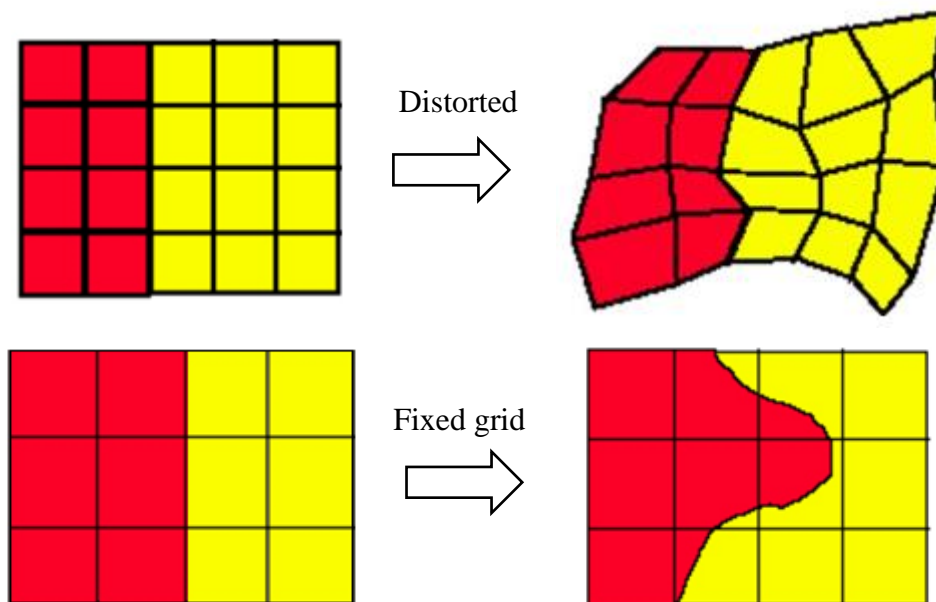
Fig 2.6: a)Lagrange mesh b) Euler mesh [21].

2.5   Blast Mitigation Techniques

Insufficient protection against blasts leads to loss of lives and economic loss due to structural damage. Therefore, various mitigation strategies are needed to safeguard the structure from primary and secondary damages. The blast mitigation strategy aims to minimize structural damage and increase the capability of the structure to function after the blast. Standoff distance is one of the important and most economic parameters in mitigation strategy, as pressure due to blast wave decays rapidly with standoff distance. When it is not possible to provide an adequate standoff distance, the structure needs to be hardened, which makes the structure uneconomical. Sometimes buildings need to satisfy design criteria for both seismic and blast loads on the structure, which can be provided by light weight and energy absorptive material. Thus, there is a need for some lightweight energy-absorbing materials to be invented [9, 13, 22]. Defense in depth is another mitigation technique, consisting of several layers that terrorists must cross before reaching the center of the asset. Physical barriers such as blast walls, anti-ram barriers, and vehicle barriers can also be constructed in standoff zone, which impedes access thereby protecting the structure [9]. Orientation and shape of the building, proper landscaping, and architectural aspects can also protect the structure against blast threats and attenuate the effective pressure [15, 23].

2.6   Mitigation Systems

There are two categories for mitigation systems active and passive mitigation systems: Active mitigation systems activated whenever a threat is detected and damage it before striking the target. These systems minimize the blast pressure, temperature, impulse and subsequently reduce the destructive effects of the blast. But the main requirement of such systems is high technology detectors. As per works of literature, these kinds of systems are not easily available. The passive mitigation systems consist of a structure with different geometric shapes and materials placed between threat and target rather than sensors to be triggered. Impedance mismatch, blast or shock wave disruption, and sacrificial cladding are different methods of passive attenuation [24]. Figure 2.7 summarizes the passive mitigation systems.
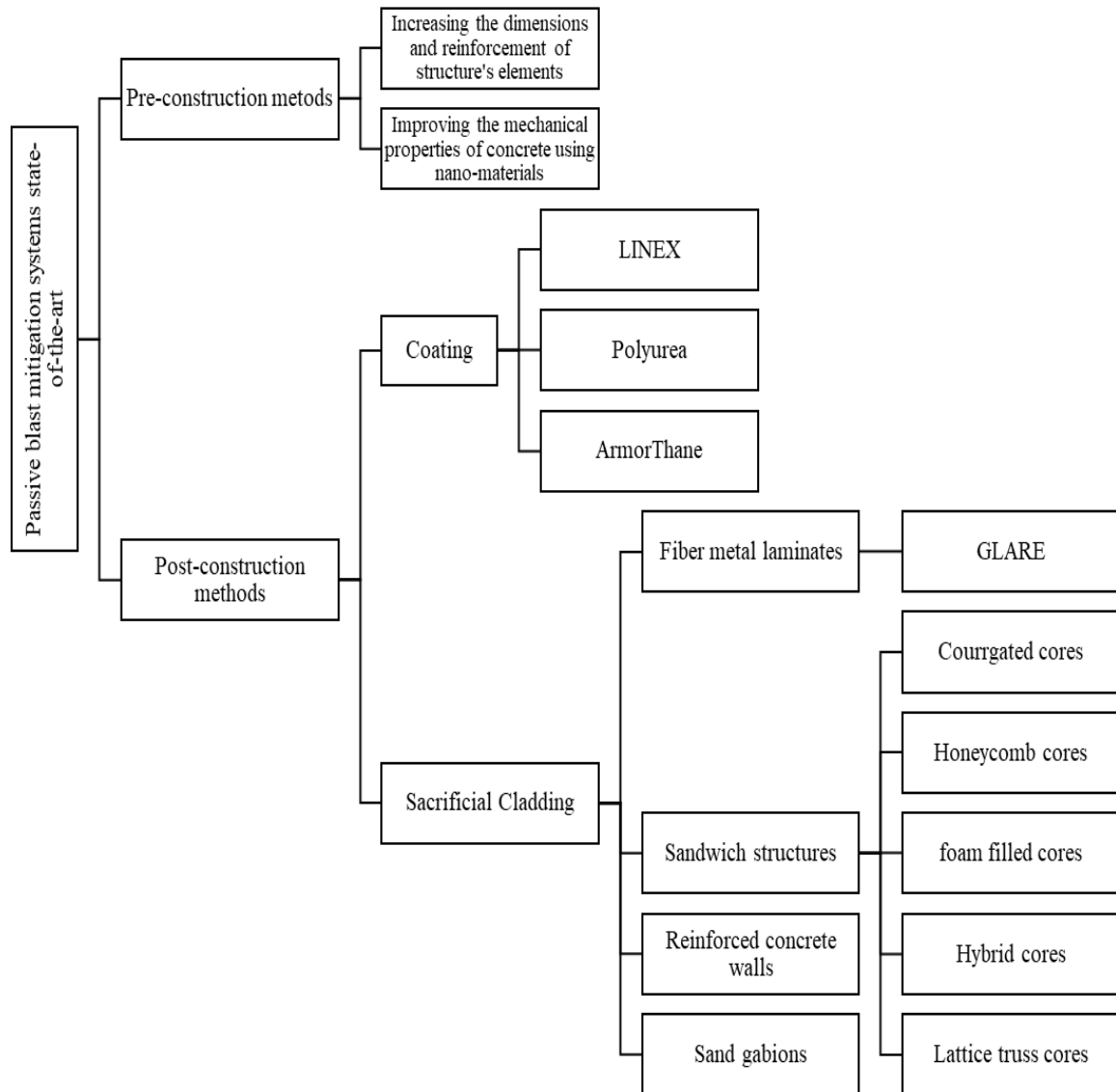
Fig 2.7: Passive blast mitigation systems state-of-the-art.

2.7   Impedance Mismatching

Impedance mismatch is done by layering different materials between the threat and the target to mitigate the impact of the shock wave or explosion. Due to impedance mismatch, there will be pressure dissipation which will act as attenuating mechanism, for instance, filling a cavity between the blast wave and the object with water [25] as illustrated in Fig 2.8.
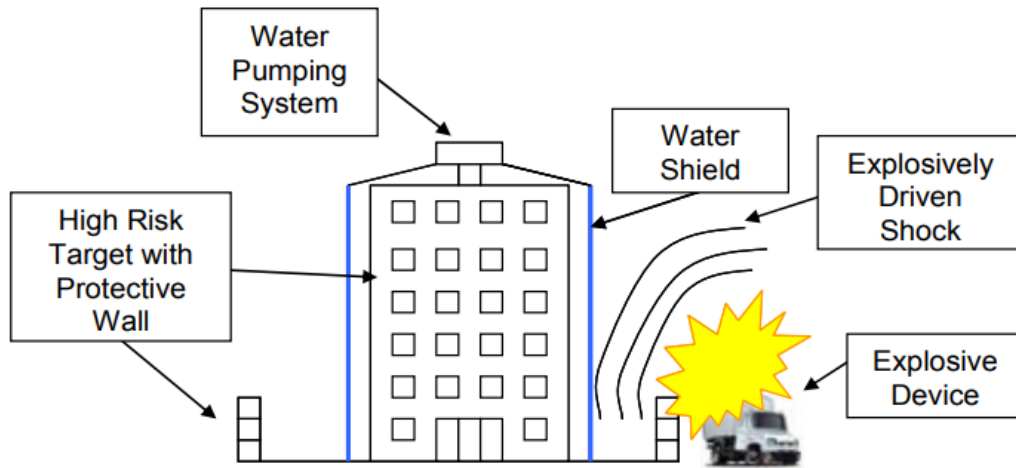
Fig 2.8: Water shields for blast mitigations.

2.8   Sacrificial Cladding

Sacrificial cladding uses multiple layers of various materials with different stress properties to absorb energy. The sacrificial cladding represented by Figure 2.9 consists of a solid shell plate and a core that absorb the impact pulse. The cover plate improves the bending ability while the core provides energy-absorbing properties [26]. These layers with different physical properties are intended to deform the plastically. Metal panels, sandwich layers, blast walls, perforated panels can be used as cladding. The literature has also noted that sandwich panels are a type of sacrificial layer and the best mitigation measure due to their superior strength and stiffness [26]. Additives can vary in sandwich panels (such as ceramic, metal foam, mesh structure, honeycomb), and highly absorbent and ballistic resistant materials [27, 28].
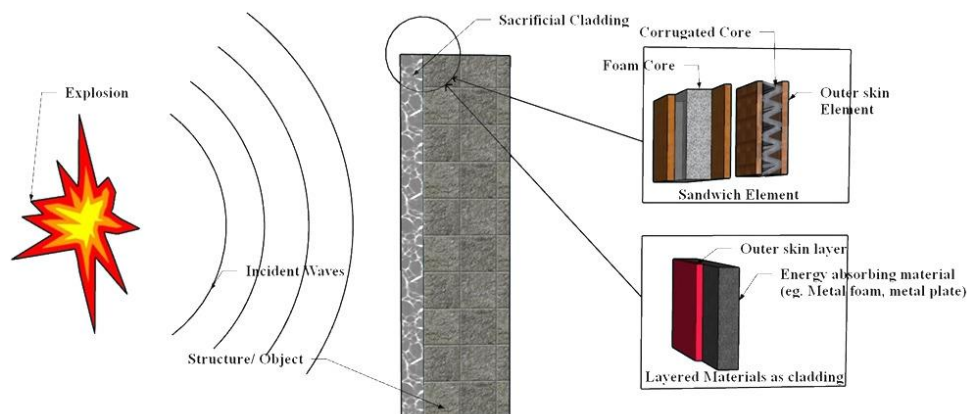
Fig 2.9: Concept of sacrificial layers.

2.9   Composite Structure Sandwich Panels (CSSPs)

The sandwich panels are comprised of two surface plates connected by a core layer. The components of the sandwich material are bonded together using either adhesives or mechanical fasteners. In a typical sandwich structure, as shown in Fig. 2.10 [29], two faces are generally fabricated from the same material and with the same thickness. The face sheets are primarily resistant to the in-plane and lateral loads. However, in particular applications, the faces may differ in thickness and material. In general, there are four types of cores: bulk foam cores, honeycomb cores, trusses cores, and web cores, as indicated in Fig .2.11.

Recently, sandwich structure configurations have been proliferated due to the urgent need for improved structural behavior without significantly increasing the weight of the structure. There are many applications for sandwich structures include explosion protection structures, satellites, automobiles, aircraft, ships, rail cars, and wind power systems [30]. The advantages of sandwich construction include.

• High bearing capacity

• High energy absorbing capability.

• Excellent thermal insulation.

• Crack progress and fracture toughness characteristics improved compared to solid bodies.

• Long life at low maintenance cost.

• Excellent blast mitigating properties.

• lighter weight for applications with weight limitation and restrictions.
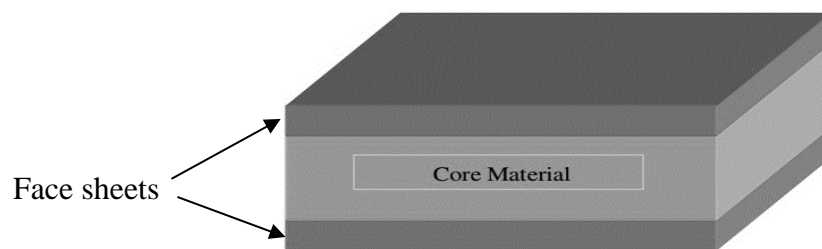
Fig. 2.10: A typical sandwich structure.
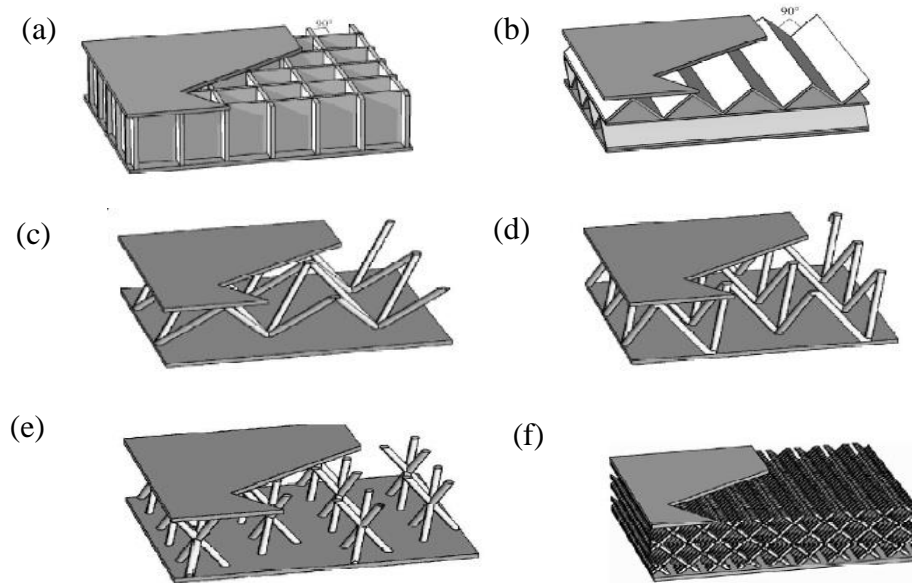
Fig. 2.11: Different types of steel core configurations. (a) Square honeycomb, (b) corrugated/diamond core (c) tetrahedral lattice, (d) pyramidal lattice, (e) kagome lattice and (f) diamond textile core [31]

2.10   Mechanism of sandwich structures to resist blast loads

Sandwich panels are often grouped into two types for blast applications. The first type are sacrificial cladding layers installed in front of the main structure to absorb impacting energy through the front face and core of the sacrificial layers. The second type is a structural element, which is used as a primary structural element. The deformation of the backing sheet mainly determines its performance. A sandwich structure subjected to blast load is exposed to a sudden velocity on the face sheet towards the blast [32]. The blast-loaded sandwich structure goes through three stages to mitigate the blast loading, as shown in Fig. 2.12. The first stage is the pulse loading stage, in which the pressure impulse strikes the structure. The front plate will rapidly move with speed (S_1) toward the backing plate. The second stage is primary crushing, in which primary crushing resists the movement of the front plate and slows down its movement; This crushing force depends on the energy absorption capabilities of the core layer. Through the second stage, the advanced face layer deforms the base material. The third stage is plate bending where the front face plate is slowed down by the core, and the back-plate deformation resists the remaining energy.
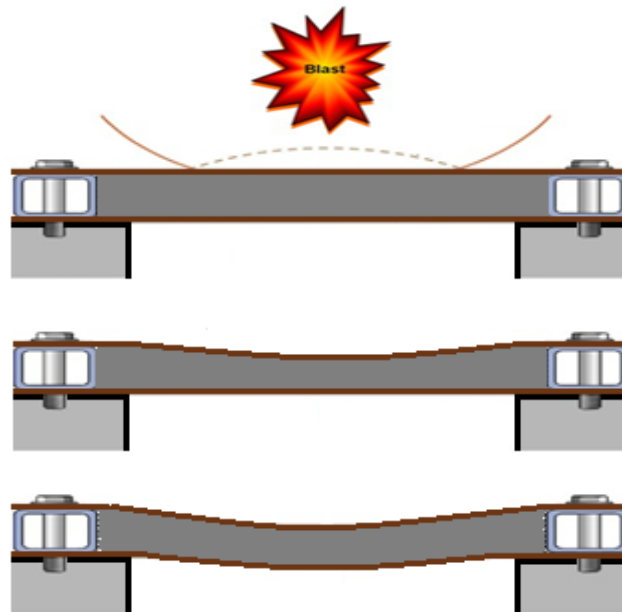
Fig. 2.12: Impact of shock wave on sandwich structure.

The efficiency of these layers depends mainly on the quantity of energy absorbed by their core [33]. Thin walled (TW) structures with different materials and geometric shapes have been exploited as energy absorbers. They absorb in a large magnitude of kinetic energy and convert it into plastic strain energy when it is deformed under stress produced by the shock load [34].

2.11   Thin-walled structures for energy absorption applications

Metals such as mild steel and aluminium alloys are the most common used materials to manufacture TW energy absorbers. The ductility of metallic alloys allows the energy to be dissipated through its plastic deformation. TW metal tubes with diverse cross-sections are extensively adopted as energy absorption structures in the industry for their low price, high strength to weight ratio, and high energy absorption. Several kinds of investigations have examined the mechanisms of TW metal tube breakdown under axial fracturing. Robertson [35] was the first to carry out experimental and theoretical studies for metallic TW tubes under axial pressure. The results showed the ability of TW tubes to absorb a large quantity of energy. Jones [36] notes that TW tubes are more suitable and desirable as an energy absorbent due to their simplicity, high energy absorption. Andrews et al. [37] experimentally studied the impact resistance of aluminium tubes under axial quasi-static pressure tests and also examined the effect of tube length on the failure mode. Song et al. [38] explore the

interaction between aluminium foaming and metal tubes under an axial pressure load through experimental tests and numerical simulations.

To reduce the weight of energy absorption components, composites have been introduced since 1970 to replace traditional metals, which provide high strength accompanied by lightweight [39]. Metals absorb energy through plastic deformation, while composites are brittle and disperse energy through various fracturing mechanisms such as loosening and breaking the fibres and cracking the matrix. Palanivelu et al. [40] studied experimentally the absorbing energy of composite tubes of different configurations handcrafted using e-glass fabric bonded with polyester matrix under a quasi-static pressure load.

Researchers also examined the behaviour of composite tubes filled with honeycomb and foams. Liu et al. [41] studied the failure mechanisms of the CFRP tubes filled with Al honeycomb under lateral and axial quasi-static crushing tests. Results showed that the absorption energy (AE) and the specific absorption energy (SAE) of the filled CFRP tubes increased by 6.56 and 4 times, respectively. Interestingly, G. Sun et al. [42] found through an experimental study that the SAE of CFRP tubes filled with foam is lower than that of the hollow CFRP, indicating the features of filled TW CFRP structures energy absorption are not fully understood.

Recently, hybrid structures have been introduced to improve the energy absorption of TW structures. Hybrid tubes maybe composite tubes reinforced with metal tubes or metal tubes wrapped with fibres. Hybrid structures are a mixture of desirable properties for each material, for example, strength to weight, stress-to-displacement ratios of composites, stable deformation, and ductility of metals. Shen et al. [43] performed experimental tests to assess the energy absorption of GFRP hybrid tubes under affective and axial compression loading. They compared the average crushing load of aluminium and composite and hybrid tubes with the same weight under axial load. The hybrid tube was found to have excellent energy absorption capabilities. Babbage and others [44] conducted experimental studies to evaluate the energy absorption of aluminium / hybrid composite tubes. The hybrid tubes increased the absorbed energy by 40%. They also investigated the influence of adding more composite layers on energy absorption. The absorption energy increases with the number of composite layers. Mirzai et al. [45] ran an experimental examination of the effect of the stacking structure of external GFRP composite tubes on the impact resistance of the aluminium / GFRP circular hybrid tubes. The results indicated that the stacking configuration has a

significant influence on the shock resistance properties. For example, exercise [90/0/0/90] absorbs 30% more energy compared to [90/90/90/90] layup. The crushing behaviour of CFRP coiled hybrid tubes and aluminium/carbon fibre reinforced plastics subjected to quasi-static axial loads was experimentally studied by Guangyoung et al. [46]. The hybrid tubes have shown more stable crushing behaviours and a larger energy absorption ability compared to the traditional tubes. All the methods adopted for improving the energy absorption capacity for the thin-walled structures are illustrated in Fig. 2.13.
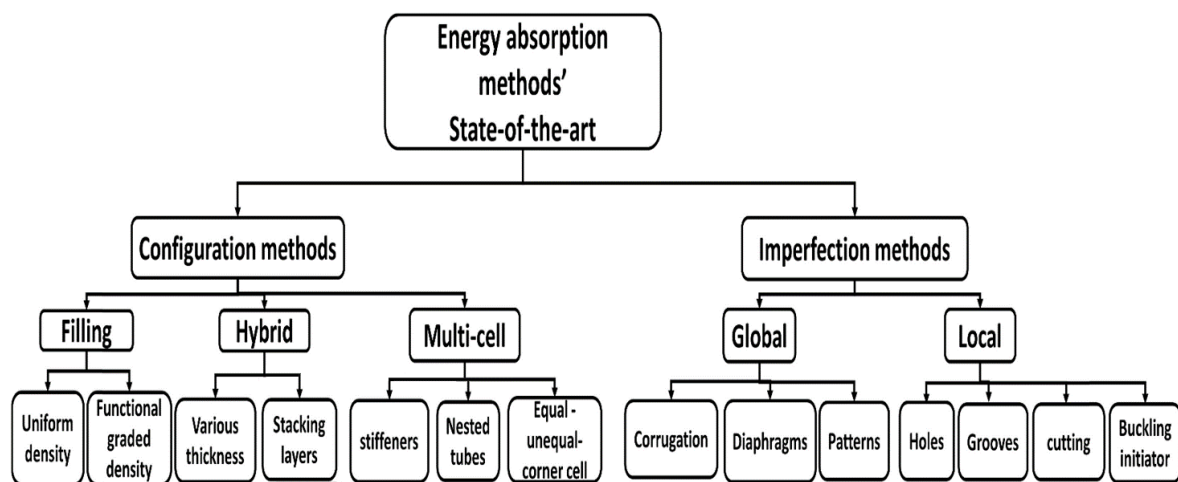
Fig. 2.13: Energy absorptions techniques state of art.

2.11.1 Axial Crushing Behaviour:

The axial crushing test is a well-known procedure for predicting the axial capacity of energy absorption in shock resistance analysis. Based on the loading rate, the crush test can be done in two ways, the Impact test, and the quasi-static test.

2.11.1.1   Impact Testing

Impact testing is performed with a hammer or impact tool, as shown in Fig. 2.14, to simulate the shock load occurring in an impact event. Sample dimensions are usually designed based on preliminary calculations to determine tube geometry to avoid torsion failure [47]. The tested specimens have typical dimensions from 50 to 125 mm long, 20-100 mm diameter / outer width, and a wall thickness in the range of 1-3 mm [48].
In addition to the loading rate applied to the sample, factors such as the stress rate sensitivity

of the material are usually taken into account. However, the overall test time is minimal. Equipment such as high-speed cameras and electronic control devices are usually used to collect test data and record sample responses. As a result, the impact test is costly; Therefore, a quasi-static test is often used to assess the energy absorption of TW structures.
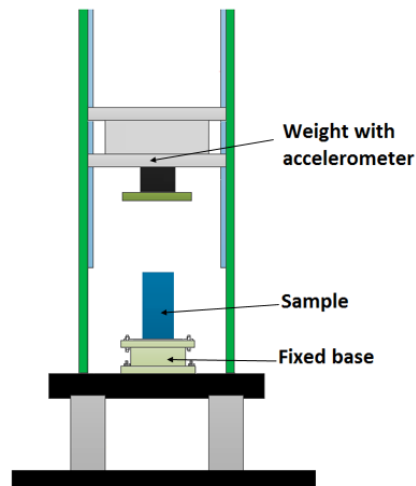
Fig. 2.14: A typical impact testing setup.

2.11.1.2   Quasi-static testing

In this test, the sample is crushed axially at a constant velocity typically between 1-10 mm/s. The test sample is compressed between two parallel level plates. One of the panels is fixed while the other is moving at a constant velocity, as shown in Fig. 2.15. The quasi-static tests are more accessible to control than the impact test. However, this type of test cannot be considered an accurate simulation of actual breakdown conditions due to the sensitivity of some materials concerning the rate of load stress. However, it can be used to obtain energy absorption and monitor failure mechanisms.
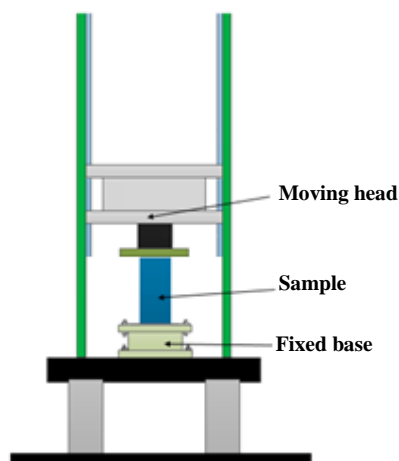
Fig. 2.15: A typical quasi-static test setup.

2.11.2 Energy Absorption Characterisation

In axial crushing tests performed by impact loading or quasi-static pressure, impact resistance parameters are determined from the load-displacement curve. The typical load-displacement of a TW tube exposed to axial quasi-static pressure is divided into three regions. The first region is the pre-fracturing region from the origin to the peak of the fracturing load. The second is the post-fracturing region, which is characterized by an average fracturing load. The third zone is the pressure zone and can be neglected.

The most-reported parameters to evaluate the energy absorption are the specific absorption energy and the crushing force efficiency. Specific absorption energy (SAE) is defined as the absorbed crush energy (AE) per the crushed specimen unit mass (m).

$$SAE = \frac{AE}{m}$$

Absorbed energy (*AE*) is the area below the load-displacement history regardless of the compaction zone.

$$AE = \int_0^{d\ max} P \ d\Delta$$

where P is the load and Δ is the displacement.

Crushing force efficiency (CFE) is also used to evaluate the behaviour of the energy absorption component and is defined as the ratio between the average crushing load and the peak load,

$$CFE = \frac{P_{avg}}{P_{max}} \text{ x } 100$$

Peak load (P_{max}) is the maximum load disregarding the compaction zone, and the average crushing load P_{avg} is the ratio of the absorbed energy in the post-crushing zone (E_c) to the post-crushing displacement (δ).

$$P_{avg} = \frac{E_c}{\delta}$$

This review facilitates the task of achieving new configurations for sacrificial cladding structures which is presented in the remaining chapters.

2.12   References:

1.   Ngo, T., et al., Blast loading and blast effects on structures–an overview. Electronic Journal of Structural Engineering, 2007. 7(S1): p. 76-91.

2.   Baker, W., et al., Explosion hazards and evaluation, 1983. Elsevier Scientific Publishing Co., Amsterdam, The Netherlands.

3.   Akhavan, J., The chemistry of explosives. 2011: Royal Society of Chemistry.

4.   Mouritz, A.P. and Y.D. Rajapakse, Explosion Blast Response of Composites. 2017: Woodhead Publishing.

5.   Committee, T. Structural Design for Physical Security: State of the Practice. 1999. ASCE.

6.   Verma, S., M. Choudhury, and P. Saha, Blast resistant design of structure. IJRET: International Journal of Research in Engineering and Technology, 2016. 5(1): p. 254-261.

7.   Zhang, C. and A.A. Mousavi, Blast loads induced responses of RC structural members: State-of-the-art review. Composites Part B: Engineering, 2020: p. 108066.

8.   Hao, H., et al., Review of the current practices in blast-resistant analysis and design of concrete structures. Advances in Structural Engineering, 2016. 19(8): p. 1193-1223.

9.   Goel, M.D. and V.A. Matsagar, Blast-resistant design of structures. Practice Periodical on Structural Design and Construction, 2014. 19(2): p. 04014007.

10.   Karlos, V. and G. Solomos, Calculation of blast loads for application to structural components. Luxembourg: Publications Office of the European Union, 2013.

11.   Baker, W.E., et al., A manual for the prediction of blast and fragment loadings on structures. 1981, Southwest Research Inst San Antonio TX.

12.   Kingery, C.N. and G. Bulmash, Airblast parameters from TNT spherical air burst and hemispherical surface burst. 1984: US Army Armament and Development Center, Ballistic Research Laboratory.

13.   Remennikov, A. and D. Carolan, Building vulnerability design against terrorist attacks. 2005.

14.   Ullah, A., et al., Review of analytical and empirical estimations for incident blast pressure. KSCE Journal of Civil Engineering, 2017. 21(6): p. 2211-2225.

15.   Badshah, E., et al., Review of blast loading models, masonry response, and mitigation. Shock and Vibration, 2017. 2017.

16.   Army, T., TM 5-1300 "Structures to Resist the Effects of Accidental Explosions"; Navy NAVFAC P-397, AFR 88-2. Washington, DC, Departments of the Army, Navy, and Air Force, 1990.

17.   Remennikov, A.M., A review of methods for predicting bomb blast effects on buildings. 2003.

18.   Türkmen, H. and Z. Mecitoğlu, Dynamic response of a stiffened laminated composite plate subjected to blast load. Journal of Sound and Vibration, 1999. 221(3): p. 371-389.

19.   Zárate, F., et al., A coupled fluid FEM-DEM technique for predicting blasting operations in tunnels. Underground Space, 2018. 3(4): p. 310-316.

20.   Abada, M. and A. Ibrahim, Metallic Ribbon-Core Sandwich Panels Subjected to Air Blast Loading. Applied Sciences, 2020. 10(13): p. 4500.

21.   AUTODYN, T., Theory Manual Revision 4.3, Concord, CA: Century Dynamics. 2003, Inc.

22.   Schimizze, B., et al., An experimental and numerical study of blast induced shock wave mitigation in sandwich structures. Applied Acoustics, 2013. 74(1): p. 1-9.

23.   Gebbeken, N. and T. Döge, Explosion protection—architectural design, urban planning and landscape planning. International Journal of Protective Structures, 2010. 1(1): p. 1-21.

24.   Langdon, G., et al., Perforated plates as passive mitigation systems. Defence Science Journal, 2008. 58(2): p. 238.

25.   Zakrajsek, A.J., Experimental and numerical analysis of water blast mitigation: Focusing on solid water barriers, water sprays, and water-sheets. 2012, Purdue University.

26.   Ding, Y., et al., Blast alleviation of cellular sacrificial cladding: A nonlinear plastic shock model. International Journal of Applied Mechanics, 2016. 8(04): p. 1650057.

27.   Goel, M.D., et al., Comparative performance of stiffened sandwich foam panels under impulsive loading. Journal of performance of constructed facilities, 2013. 27(5): p. 540-549.

28.   Codina, R., D. Ambrosini, and F. de Borbón, New sacrificial cladding system for the reduction of blast damage in reinforced concrete structures. International Journal of Protective Structures, 2017. 8(2): p. 221-236.

29. Ergönenç, Ç., Development and design of closed-cell aluminum foam-based lightweight sandwich structures for blast protection. 2008, Izmir Institute of Technology.

30. Vinson, J.R., Sandwich structures: past, present, and future, in Sandwich structures 7: advancing with sandwich structures and materials. 2005, Springer. p. 3-12.

31. Li, Z., et al., Deformation behavior and mechanical properties of periodic topological Ti structures fabricated by superplastic forming/diffusion bonding. International Journal of Lightweight Materials and Manufacture, 2019. 2(1): p. 1-30.

32. Fleck, N. and V. Deshpande, The resistance of clamped sandwich beams to shock loading. Journal of Applied Mechanics, 2004. 71(3): p. 386-401.

33. Van Paepegem, W., et al., Blast performance of a sacrificial cladding with composite tubes for protection of civil engineering structures. Composites Part B: Engineering, 2014. 65: p. 131-146.

34. Alghamdi, A., Collapsible impact energy absorbers: an overview. Thin-walled structures, 2001. 39(2): p. 189-213.

35. Robertson, A., The strength of tubular struts. Proceedings of the Royal Society of London. Series A, Containing Papers of a Mathematical and Physical Character, 1928. 121(788): p. 558-585.

36. Jones, N., Structural impact. 2011: Cambridge university press.

37. Andrews, K., G. England, and E. Ghani, Classification of the axial collapse of cylindrical tubes under quasi-static loading. International Journal of Mechanical Sciences, 1983. 25(9-10): p. 687-696.

38. Song, H.-W., et al., Partition energy absorption of axially crushed aluminum foam-filled hat sections. International Journal of Solids and Structures, 2005. 42(9-10): p. 2575-2600.

39. Ramakrishna, S. and H. Hamada. Energy absorption characteristics of crash worthy structural composite materials. in Key engineering materials. 1998. Trans Tech Publ.

40. Palanivelu, S., et al., Comparative study of the quasi-static energy absorption of small-scale composite tubes with different geometrical shapes for use in sacrificial cladding structures. Polymer testing, 2010. 29(3): p. 381-396.

41. Liu, Q., et al., Lateral crushing and bending responses of CFRP square tube filled with aluminum honeycomb. Composites Part B: Engineering, 2017. 118: p. 104-115.

42. Sun, G., et al., Experimental study on crashworthiness of empty/aluminum foam/honeycomb filled CFRP tubes. Composite Structures, 2016. 152: p. 969-993.

43. Shin, K.C., et al., Axial crush and bending collapse of an aluminum/GFRP hybrid square tube and its energy absorption capability. Composite structures, 2002. 57(1-4): p. 279-287.

44. Babbage, J. and P. Mallick, Static axial crush performance of unfilled and foam-filled aluminum–composite hybrid tubes. Composite structures, 2005. 70(2): p. 177-184.

45. Mirzaei, M., et al., Experimental, and analytical assessment of axial crushing of circular hybrid tubes under quasi-static load. Composite structures, 2012. 94(6): p. 1959-1966.

46. Sun, G., et al., Experimental investigation of the quasi-static axial crushing behavior of filament wound CFRP and aluminum/CFRP hybrid tubes. Composite Structures, 2018. 194: p. 208-225.

47. Alexander, J.M., An approximate analysis of the collapse of thin cylindrical shells under axial loading. The Quarterly Journal of Mechanics and Applied Mathematics, 1960. 13(1): p. 10-15.

48. Lau, S.T., M.a. Said, and M.Y. Yaakob, On the effect of geometrical designs and failure modes in composite axial crushing: a literature review. Composite structures, 2012. 94(3): p. 803-812.

Chapter 3: Hybrid Multi-Cell Thin-Walled Tubes for Energy Absorption Applications: Blast Shielding and Crashworthiness

3.1   Introduction

A specific concern of reducing the potential damage of structures exposed to impact loads has been raised in the last decade. Protecting structures from impact hazards drives researchers to adopt sacrificial layers [1-3]. These layers are adequate to absorb various impact loads. The protective layer systems may consist of efficient absorbing core layer, as illustrated in Fig.3.1. These cladding structures have the ability to mitigate blast loads and reduce the potential damage of the structure by reducing the impulsive force level and increasing the duration of the pulse.

Efficient mitigation systems are usually made of sandwich panels [4]. Sandwich panels typically have three layers; two outer plates made of metals or composite materials and a core layer in-between, as demonstrated in Fig.1 [5]. The plate facing the blast wave distributes the pressure load more evenly across the core layer that deforms progressively, so the pressure transferred to the structure is attenuated. The core layer can have various forms, for instance, corrugated sheets [6], woven configuration cores [7], honeycomb cores [8], trusses cores [9], and foams. The efficiency of these mitigation structures relies on the amount of energy absorbed by their core.

At this juncture, it can be predicted that the performance of sandwich structures should be more efficient if the core develops progressive crushing and yielding excellent resulting energy absorption. Hence, the objective of this study is to design a hybrid multi-cell thin-walled structure that exhibits appropriate energy absorption capabilities along with robust specific energy absorption and crush force efficiency.
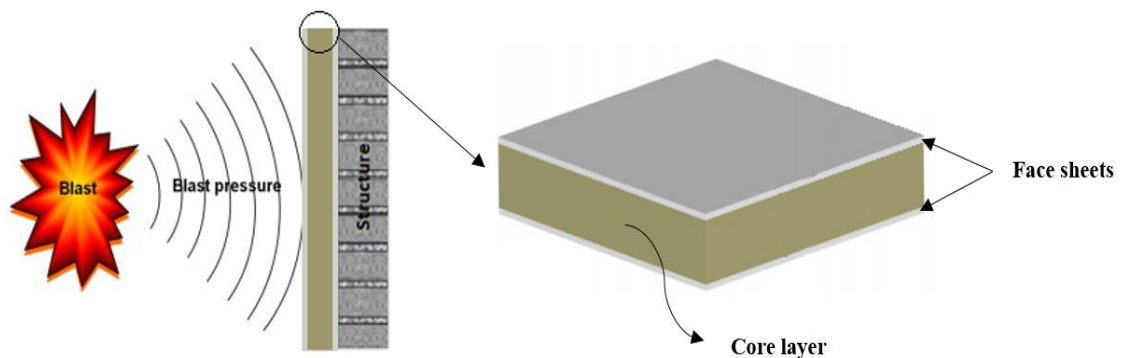
Fig. 3.1: Schematic of sacrificial cladding structures [2].

Moreover, playing a crucial role in cladding structures, energy absorbers also are essential for crashworthiness design. Crashworthiness is the ability of a structure to absorb a large amount of energy and convert it into plastic strain energy when it deforms under pressure resulted from impact events. Thin-walled (TW) structures with different materials and geometries have been exploited as energy absorbers in crashworthiness applications [10].

Numerous studies have been conducted to understand and assess the energy absorption capabilities of TW structures. They can be produced with different cross-sections such as circular, square, hexagonal, octagonal, oblong, conical, taper, frusta, corrugation and S-shaped [11-16]. Among these, circular thin-walled tubes have been significantly utilized as a crashworthy component due to their outstanding crashworthiness characteristics, low cost, lightweight, and ease of manufacturing. Multi-cell tubes have been raised as an effective method to boost the energy absorption adequacy while at the same time maintaining the weight efficiency of the structure [17-20].

Besides the abovementioned multi-cell tubular structures, hybrid structures with simple configurations have gained considerable interest due to their better energy absorption than the simple hollow unfilled tubes. Therefore, several studies had focused on the performance of hybrid thin-walled structures as crashworthiness mitigative structures. Mirzaei et al. [21] demonstrated that staking sequence of the outer GFRP composite tube has a significant effect on crashworthiness of circular aluminum/GFRP hybrid tubes. For instance, layup [90/0/0/90] absorbs 30% more energy compared to [90/90/90/90] layup.

Zhu et al. [22] conducted an extensive study on the behavior of different three AL/CFRP hybrid tubes configurations; aluminum tube externally wrapped with CFRP tube, CFRP tube surrounded by aluminum tube, AL/CFRP/AL sandwiched tubes. They concluded that the CFRP tube surrounded by an aluminum tube displayed the best crashworthiness capabilities. Furthermore, in the same energy absorption, this type of hybrid tube reduces the cost by 32.1% compared to the standalone CFRP tube and could reduce weight by 33.6% compared to the standalone aluminum tube. Guangyoung et el. [23] experimentally studied the crushing performance of filament wound CFRP and aluminum/CFRP hybrid tubes under axial quasi-static loads. Hybrid tubes expressed more stable crushing performance and better energy absorption capacity compared to conventional tubes.

Based on the aforementioned literature, most of the previous research focused on the metallic multi-cell structures or on hybrid structures with empty or filled hollow profiles. Introducing multi-cell profiles to the hybrid tubular structures will provide a proper

technique to provide lighter weight, excellent crashworthiness performance, and an acceptable price. The current work presents a new configuration for the hybrid multi-cell thin-walled circular tubes as an attempt to improve their energy absorption characteristics. The new configurations are double and quadruple cell tubes wrapped with CFRP sheets. Six configurations of metallic and hybrid multi-cell thin-walled circular tubes were constructed to investigate their energy absorptions characteristics. Numerical analysis was performed to simulate the crushing performance of the proposed tubes using finite element software (ANSYS-WORKBENCH/ LS-DYNA) [24]. All numerical models were implemented under the axial quasi-static compression load. The numerical and the experimental results were compared. Finally, a comparative study was carried out to compare the energy absorption characteristics and the deformation modes among the metallic/hybrid conventional and multi-cell thin-walled circular tubes.

3.2 Experimental setup

3.2.1 Preparation of specimens

This study includes two categories of multi-cell tubes, as demonstrated in Fig.3.2. The first is metallic multi-cell tubes as control samples, while the second is hybrid multi-cell tubes. The AL specimens were used as control samples. Table 3.1 illustrates the summary of all specimens used in this study.

3.2.1.1 Metallic multi-cell tubes

The metallic specimens tested in the present work were fabricated from aluminum alloy 6061-T6. The stress-strain curve of the AA6061-T6 was obtained by performing tensile tests with the standard dimensions specified in ASTM E8M-04. The engineering stress-strain curve of AA6061-T6 and the specimen are shown in Fig.3.3. The mechanical properties are given as follows; $\rho = 2.7 \times 10^3 \, \text{kg/m}^3$, Poisson's ratio $\mu = 0.33$, Young's modulus $E = 69 \, \text{GPa}$, initial yield stress $\sigma_{y0} = 230 \, \text{MPa}$, and the ultimate tensile strength is $\sigma_u = 345 \, \text{MPa}$.

The cross-sectional dimensions of the AL tubes are illustrated in Fig.3.2., where all the cells were designed to avoid global buckling failure. The length of all specimens was 120 mm, while the inner diameter of the tube was 60 mm. The thickness of the tube wall and the interior stiffeners were 1.6 mm. A gas tungsten arc welding technique was applied to

assemble the AL plates inside the tubes to get the desired configuration and to clamp the component during the test.

3.2.1.2 CFRP/AA6061 multi-cell tubes

Hybrid tubes were manufactured by wrapping unidirectional CFRP sheets around the AA6061-T6 tubes. Simpson-Strong-Tie's CFRP sheets and the manufacturer epoxy resin with the recommended curing process were used in this study. Tensioning was applied during the fabrication process to guarantee that all samples have the required thickness with no trapped air between the wrapped CFRP sheets and the Al tubes. The ends of the tubes were ground to ensure that the tubes ends were even to avoid eccentricity loading during the test.

Two different-Hybrid AL/CFRP samples were prepared to select the proper layout of CFRP plies that attains more energy absorption capacity. Sample A consisted of four CFRP layers with [0°/90°/0°/90°] layout while sample B was composed of the same number of plies with [90°/0°/90°/0°] layout. The total thickness of the CFRP layers was 1.6 mm. Results showed that hybrid tubes with [0°/90°/0°/90°] CFRP layers achieved 35% more energy absorption as illustrated in Fig. 3.4.

Consequently, the new hybrid multi-cell tubes were fabricated by wrapping four unidirectional CFRP sheets with orientation [0°/90°/0°/90°] around AA6061-T6 multi-cell tubes as shown in Fig. 3.2. The hybrid tubes were crushed with the aforementioned quasi-static uniaxial compression test. The dimensions of the hybrid tubes were the same as the metallic tubes. The dimensions of the cross-sections of the hybrid tubes are shown in Fig. 3.2.
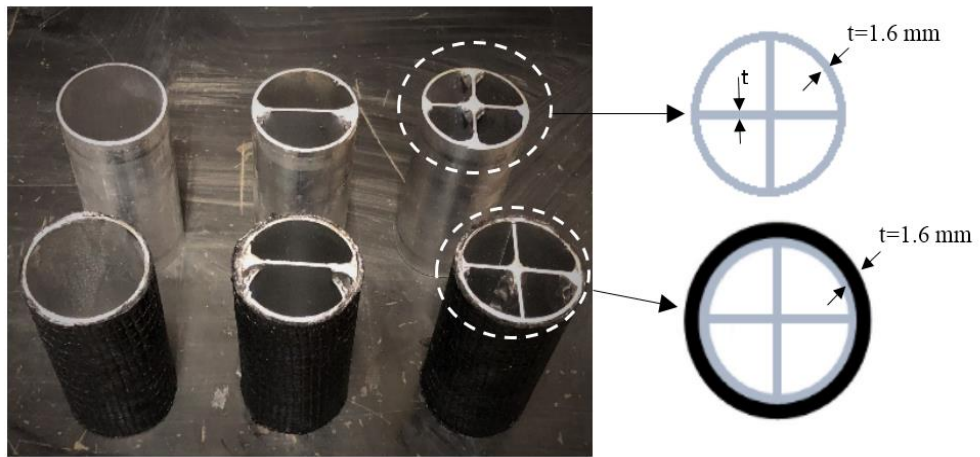
Fig. 3.2: Metallic and hybrid multi-cell tubes
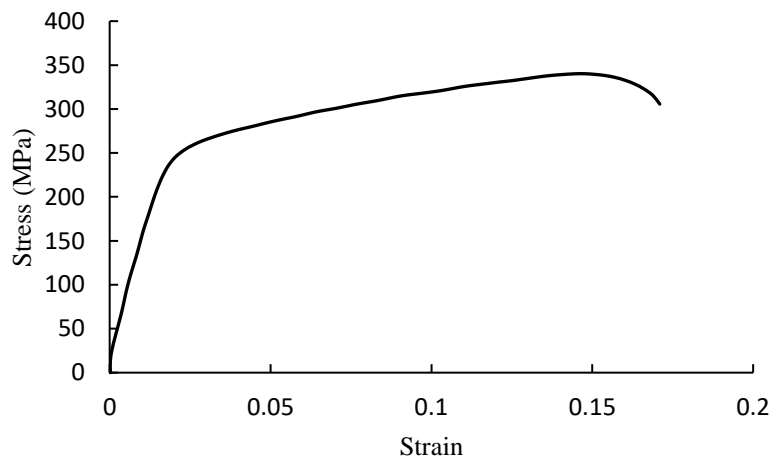
Fig. 3.3: Engineering stress-strain curve for AA6061-T6.
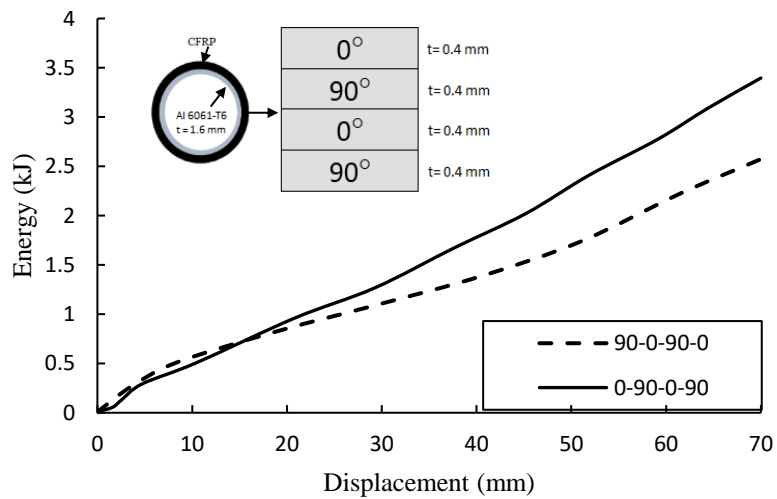
Fig. 3.4: Energy absorbed by two different lamina layouts.

Table 3.1 Specimens description used in the study.

Specimen	Configuration	Weight (g)	Length (mm)	Materials
AL single-cell tube (Al-SCT)		106	120	AA 6061
AL double-cell tube (Al-DCT)		130	120	AA 6061
AL quadruple-cell tube (Al-QCT)		157	120	AA 6061
Hybrid single-cell tube (H-SCT)		152	120	AA 6061-CFRP
Hybrid double-cell tube (H-DCT)		176	120	AA 6061-CFRP
Hybrid quadruple-cell tube (H-QCT)		203	120	AA 6061-CFRP

3.2.2   Experimental test

In order to investigate the crushing behavior of the specimens depicted in Fig. 3.2, the crushing behavior is determined through a quasi-static test. The quasi-static axial compression test was performed by a material testing machine (MTS) with computer control and data acquisition systems, as shown in Fig. 3.5. The specimen was aligned with the machine head and compressed at a constant loading rate of 8 mm/min. the total crushing displacement was set to be 70 mm to avoid excessive loading of the testing machine.

Fig. 3.5: Material testing machine (MTS) used for Quasi-static tests.

3.2.3   Experimental results

3.2.3.1 Deformation mode

All the tested specimens were crushed progressively with the formation of folds. Figure 3.6 depicts the deformed shapes of the metallic multi-cell tubes. The diamond mode was observed for the AL-SCT, concertina mode was noticed for the AL-DCT, while the AL-QCT deformed in a mixed-mode as shown in Fig. 3.6.

Deformation modes of the hybrid specimens were more sophisticated than those of the metallic specimens. They developed progressive crushing accompanied by the formation of fronds which propagated outward, as illustrated in Fig. 3.7. These failure modes

correspond to the ''splaying'' and ''lamina bending'' types of composites' stable brittle fracture. Once the peak load is attained at the end of the linear elastic limit, the progressive failure modes of the samples were initiated with cracks formation parallel to the longitudinal axis of the specimens, which produced local stress concentration. The emerged cracks were followed by an abrupt drop in the compressive load as well as its progressive crushing parallel to the longitudinal axis of the specimen. Based on the experimental observations, the energy dissipated that is related to the collapse mode could be combined with any of the following failure characteristics; Composite lamina bundle, splaying and fragmentation of the composite skins, and cracks that grow in the longitudinal direction of the specimens as noticed from Fig. 3.7.
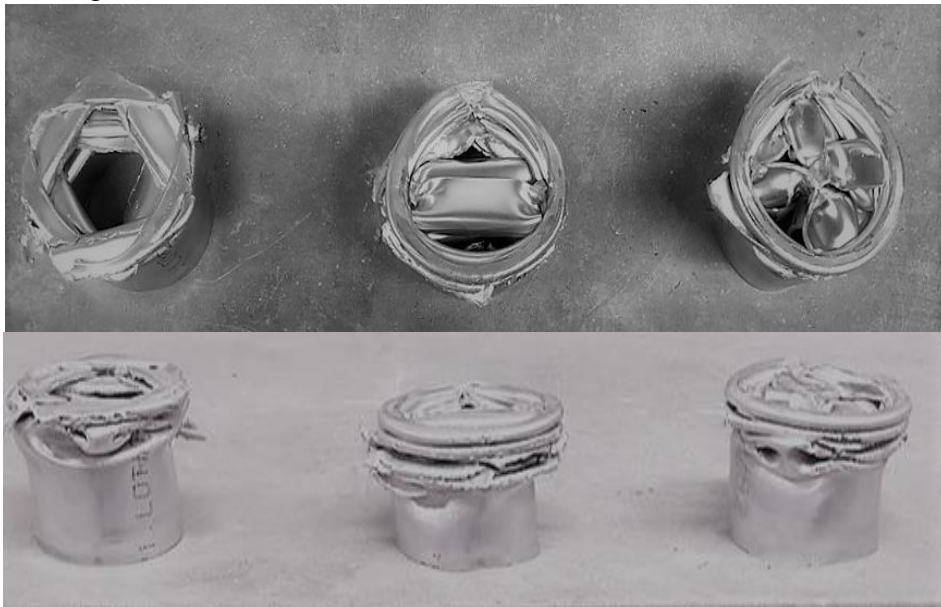
Fig. 3.6: Metallic specimens after axial crushing.

Fig. 3.7: Hybrid specimens after axial crushing.

3.2.3.2 Energy absorption

An automatic data acquisition system recorded Load-displacement histories. The following crashworthiness parameters were determined from the recorded load-displacement curves: the peak load (P_{max}) is the maximum load achieved by the specimen before crushing. The energy absorbed (*EA*) is the area under the load-displacement history disregarding the compaction zone.

$$EA = \int_0^{d\ max} P d\Delta \tag{3.1}$$

where *P* is the load and Δ is the displacement.

The specific absorption energy (*SAE*) is defined as the absorbed crush energy (*EA*) per the unit mass of the crushed specimen (*m*).

$$SEA = \frac{EA}{m} \tag{3.2}$$

Crush force efficiency (*CFE*) is also used to assess the behavior of the energy absorption component and is defined as the ratio between the average crushing load and the peak load,

$$CFE = \frac{P_{avg}}{P_{max}} \ x \ 100 \tag{3.3}$$

Peak load (P_{max}) is the maximum load neglecting the compaction zone; and the average crushing load P_{avg} is the ratio of the absorbed energy in the post-crushing zone (E_c) to the post-crushing displacement (δ).

$$P_{avg} = \frac{E_c}{\delta} \tag{3.4}$$

In this study, load-displacement and energy-displacement curves of the metallic and hybrid tested samples are demonstrated in Fig. 3.8. The details of the performance parameters of the tested samples are tabulated in Table 3.2. These parameters indicate that the total energy absorbed and specific energy absorption of the H-QCT is around 6 kJ and 29 kJ/kg, respectively. These values highlight the outstanding performance of the new proposed configurations. Hybrid multi-cell components are an efficient energy absorber structure.
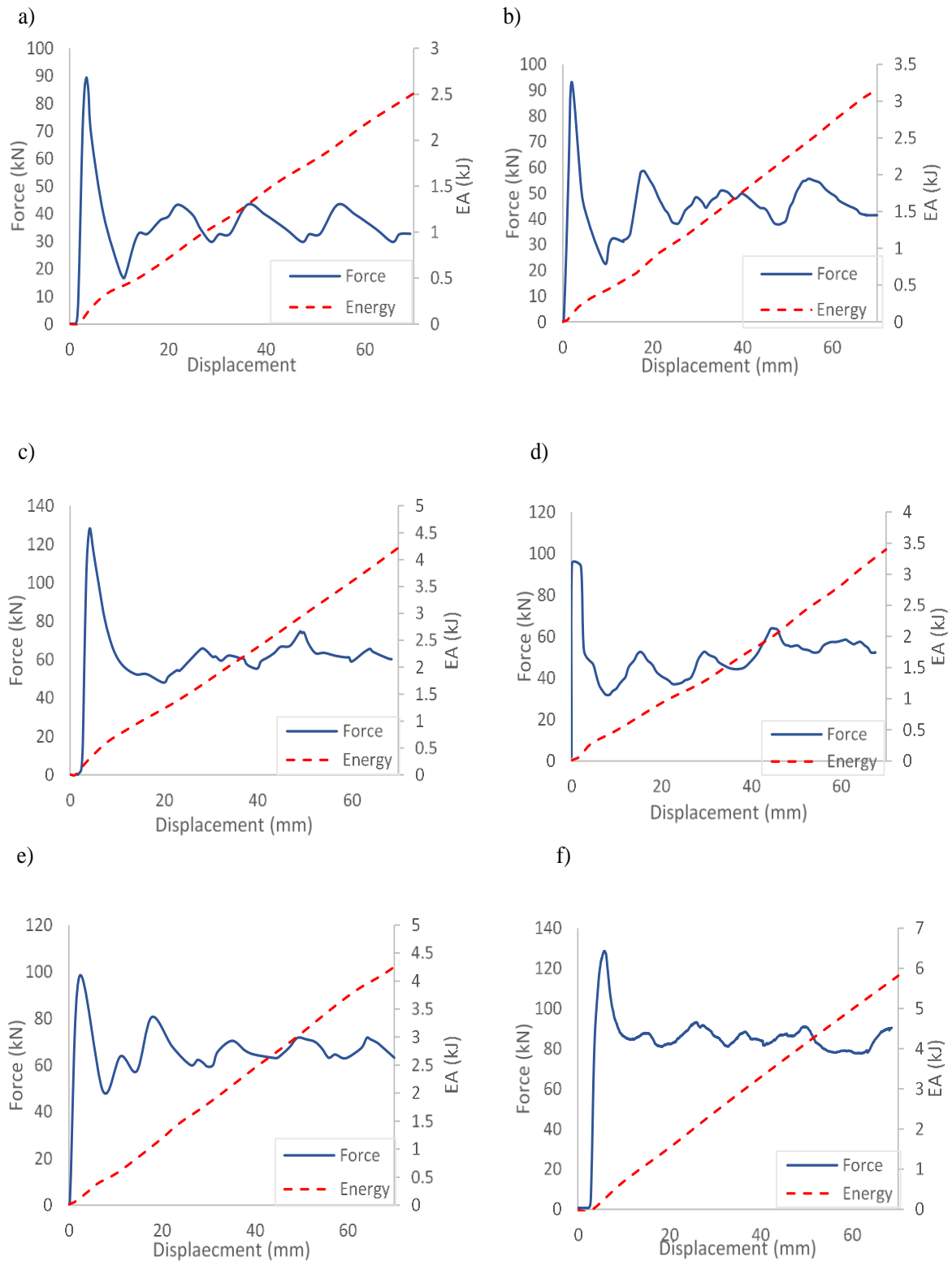
Fig. 3.8: Experimental Force-displacements histories and energy absorption a) AL-SCT, b) AL-DCT, c) AL-QCT, d) H-SCT, e) H-DCT, f) H-QCT.

Table 3.2 Crashworthiness parameters of the specimens used in the study.

Specimen ID	Energy absorbed (kJ)	Specific energy absorbed (kJ/kg)	*CFE*	Average crush force P_{avg} (kN)	Peak crush force P_{max} (kN)	Improvement *(%)*
Al-SCT	2.505	23.6	0.41	36	89.4	Control Sample
Al-DCT	3.164	24.34	0.49	46	93.01	26.30%
Al-QCT	4.25	27.07	0.697	68	97.64	69.70%
H-SCT	3.385	22.27	0.49	46	94.05	35.10%
H-DCT	4.193	23.82	0.51	65	126.29	67.40%
H-QCT	5.803	28.59	0.7	90	128.6	131.70%
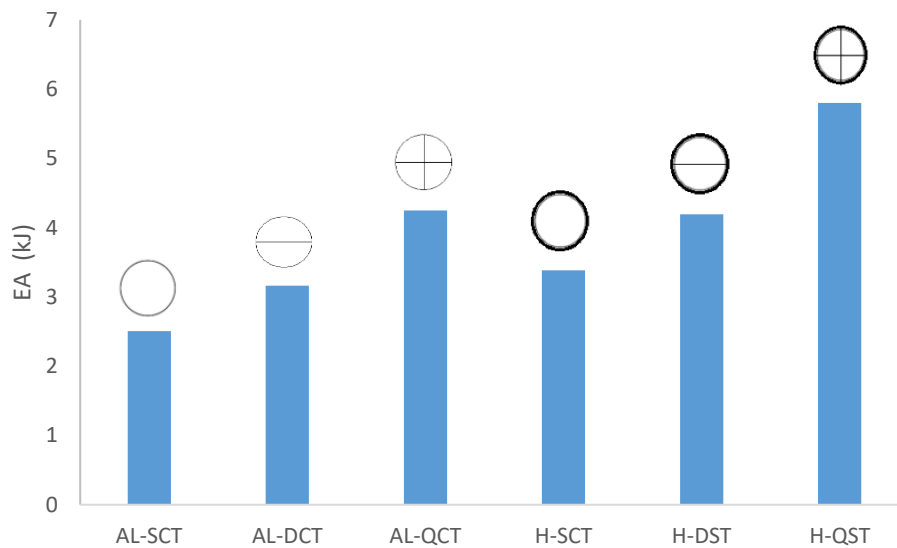
Fig. 3.9: Energy absorption for different configurations multi-cell thin-walled tubes.

3.3 Finite Element Analysis

The explicit non-linear finite element code LS-DYNA/WORKBENCH ANSYS [23] was adopted to investigate the energy absorption behavior of the presented multi-cell tubes subjected to axial quasi-static compression load. The parameters of the AA6061-T6 and the CFRP sheets, besides the interface between the AA6061 and CFRP parts, are demonstrated below.

3.3.1   FEM of the AA6061 multi-cell tubes:

The AA6061-T6 tube was generated by extrusion. The dimensions of the tubes were 1.6 mm in thickness, 60 mm for the inner diameter, and 120 mm in length. The internal ribs were constructed to fit the inner diameter of the tubes and obtain the desired configuration of the multi-cell tube. The sidewall of the tube was modeled by using the Belytschko-Tsay four-node shell elements with five integration points through the thickness and one integration point in the element plane, enabling a sufficiently accurate stress profile [24]. Stiffness-based hourglass control was adopted to avoid spurious zero-energy modes usually arising due to the usage of reduced integration elements [25]. A mesh sensitivity study was conducted in order to minimize the computational time while maintaining an accurate response of the numerical model. The AL-SCT was used to perform the convergence study using different element sizes of 5.0, 4.0, 3.5, 3.0, 2.5, 2.0, and 1.0 mm, as shown in Fig.3.10. These values were chosen to assess the numerical accuracy, and convergence for all configurations was considered in the present investigation. A mesh size of 3.0 mm is found to be sufficient to simulate the tubes with good accuracy (Fig. 3.10).

Coarse meshing is used to model the plates, as they are defined as rigid parts. The material model MAT_123 'MAT_MODIFIED_PIECEWISE_LINEAR_ PLASTICITY' in LS-DYNA library was used to model the aluminum material [25]. It is an elastoplastic material with an arbitrary stress-strain constitutive relationship and strain-rate values [23, 26]. The stress-strain curve shown in Fig.3.3, was utilized to describe the mechanical properties for AA6061. All the tubes and the internal ribs were made of aluminum alloy (AA6060-T6). Aluminum alloys' strain rate effect shows little sensitivity to the strain rate [27]. Thus, the strain rate effect was neglected in FE modeling. The FE models were placed between two rigid plates modeled as illustrated in Fig. 3.11. The upper plate was constrained in all degrees of freedom except for the applied velocity direction. The lower plate was fixed, so it was constrained in all degrees of freedom. A rigid body impacts the finite element model with 100 kg and an initial velocity of 100 mm/s. Three different types of contacts were used to simulate the interaction between surfaces. The first one was used to model the interfaces between the walls of the tube and the top and rigid bottom plates by using 'AUTOMATIC_ SURFACE _TO_SURFACE.' The second contact type was adopted between the moving plate and the tube to prevent the interpenetration between them during fold formation by using 'AUTOMATIC_SINGLE_SURFACE'. The contacts between all surfaces were described as 'FRICTIONAL', with a dynamic coefficient equal to 0.25 [28]. The friction coefficient was based on various trial values, and 0.25 was found to be a good prediction for

the studied cases. While the last contact is bonded defined to model the bond between the internal ribs and the sidewalls of the tubes.
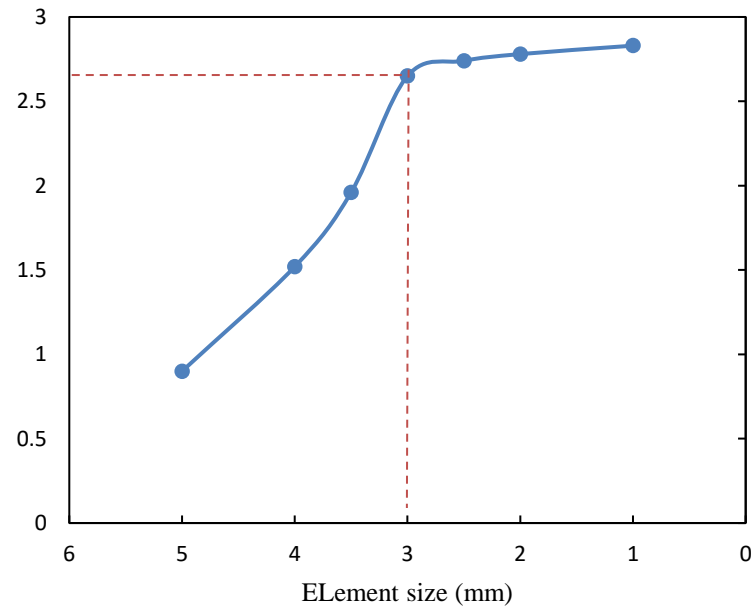
Fig. 3.10: Mesh sensitivity for AL-SCT.
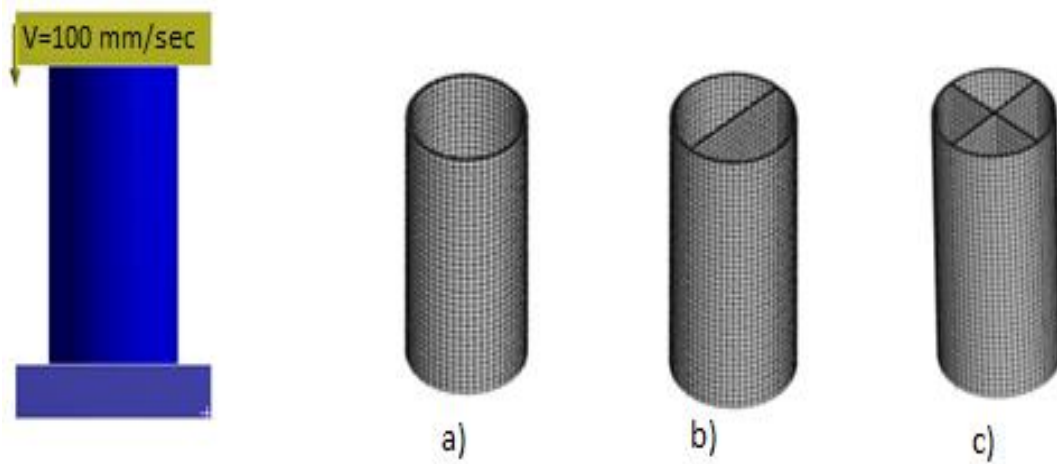
Fig. 3.11: Finite element models for the quasi-static axial compression test and the metallic specimens; a) Al-SCT, b) Al-DCT, and c) Al-QCT.

3.3.2   FEM of the hybrid multi-cell tubes

The hybrid CFRP/AA6061 tubes were fabricated by wrapping CFRP sheets around the AA6061 tube as shown in Fig.3.12. The wrapped CFRP placed outside the inner AL multi-cell tubes was simulated by combining the FEM of the AL tubes with the CFRP model. Material model 54 (MAT54) was utilized to simulate the performance of the CFRP under axial compression load. MAT54 is mainly designed to model the behavior of orthotropic materials such as unidirectional composite laminates [26]. MAT54 uses the Chang-Chang failure criterion to define the individual CFRP ply failure [26, 29-31]. The material parameters of CFRP were displayed in Table 3.3. The CFRP meshed with Belytschko-Tsay reduced-integration shell elements with four integration points through the thickness. Each ply is defined by one integration point along with the thickness, with the proposed orientation [0/90].
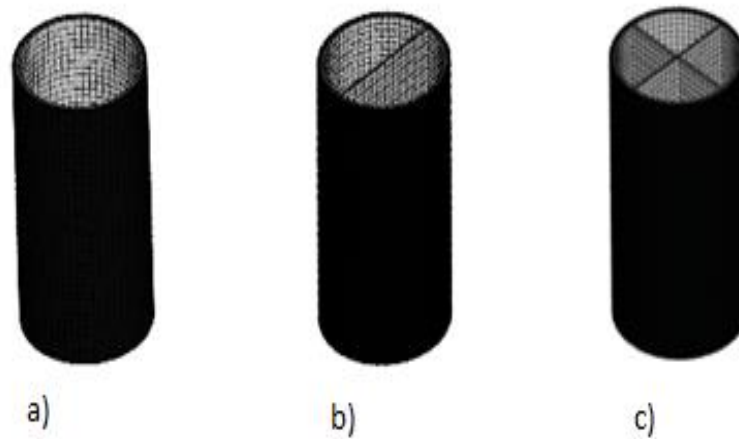
Fig. 3.12: Finite element models for hybrid specimens: a) H-SCT, b) H-DCT, c) H-QCT.

The contact between the CFRP sheets and the AA6061 tube was modeled by 'CONTACT_AUTOMATIC_SURFACE_TO_SURFACE_TIEBREAK', And this contact interface allows delamination at the interface between shell element layers. The normal failure stress (NFLS), shear failure stress (SFLS) and critical distance (CCRIT) [31] were assigned to describe the status of the contact surfaces. Damage occurs once the stresses on the interface satisfied the failure criterion in Eq. 5 [26].

$$\left(\frac{|\sigma_n|}{NFLS}\right)^2 + \left(\frac{|\sigma_s|}{SFLS}\right)^2 \geqslant 1 \tag{3.5}$$

Where, σ_n is the normal stress, and σ_s is the shear stresses acting on the contact surfaces. Once the damage has begun, the two surfaces start to detach, and the interfacial stresses decrease as a linear function of the separation distance. The critical distance

symbolized by CCRIT, was implemented to examine whether the failure occurs or not and is given by Eq. (6) [26].

$$CCRIT = \frac{2 \times E_{tie}}{S} \tag{3.6}$$

where:

$$S = \sqrt{\max(\sigma_n, 0)^2 + |\sigma_s|^2} \tag{3.7}$$

and E_{tie} is the energy released due to the failure of the interface. The critical distance can be calculated from [26]:

$$CCRIT = \frac{2 \times G_{IIC}}{SFLS} \tag{3.8}$$

where G_{IIC} is the fracture energy release rate. No standard procedures were available to get the value of G_{IIC} [29]. Numerical simulations of the CFRP/AA6061 hybrid tube under axial compression with different NFLS and SFLS were executed to obtain a proper value for G_{IIC}. The numerical simulations were performed until the deviation between the experimental data and simulation results were acceptable.

3.3.3   Numerical results

Numerical simulations of the axial quasi-static compression test were performed using the abovementioned models utilizing LS-DYNA/WORKBENCH ANSYS. The results obtained were compared with those from the experimental work. Figure 3.14 shows the force-displacement histories acquired from both the experiments and simulations. It can be observed that the peak force obtained from the numerical simulations was higher than that from the experimental work. This may be due to some flaws during the manufacturing of the specimens. In spite of that, numerical results exhibit reasonably good agreement with the experimental results. The experimental and FEA simulation of the multi-cell tubes are displayed in Figs. 3.13 and 3.14. There is a decent agreement between the experimental results and the FEA results. A maximum discrepancy of 6.75%, and 10.69% attained for the peak crushing force and energy absorptions respectively for the metallic specimens. While for the hybrid samples the maximum discrepancy of 7.40% attained for the energy absorption. Table 3.4 summarizes the results obtained from both the experimental and numerical investigation of multi-cell tubes.

Experimental

Diamond lobes

Simulation

Experimental

Petal shape fragmentation
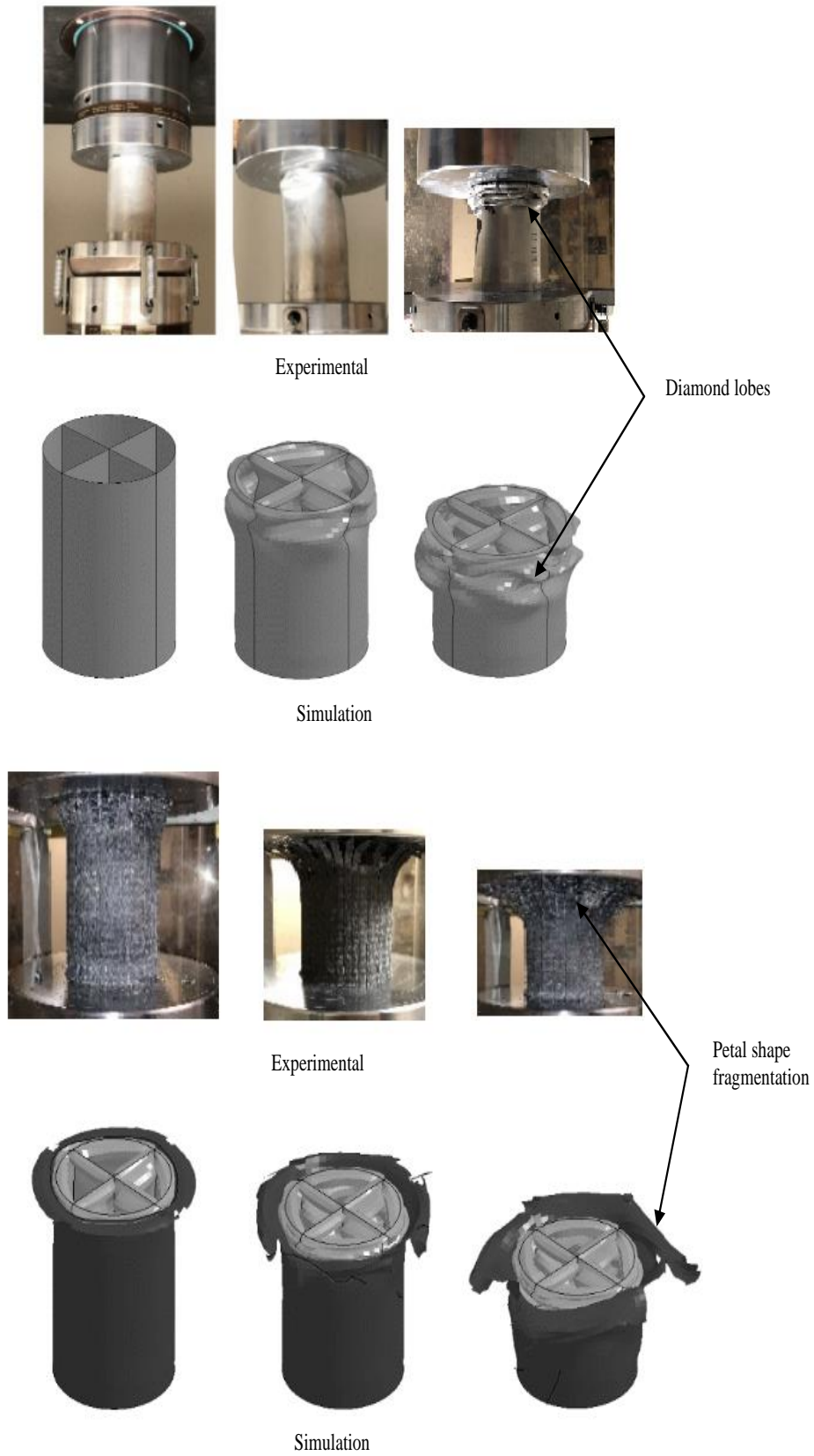
Simulation

Fig. 3.13: Experimental and FE simulations for the metallic and hybrid multi-cell tubes subjected to quasi-static test.
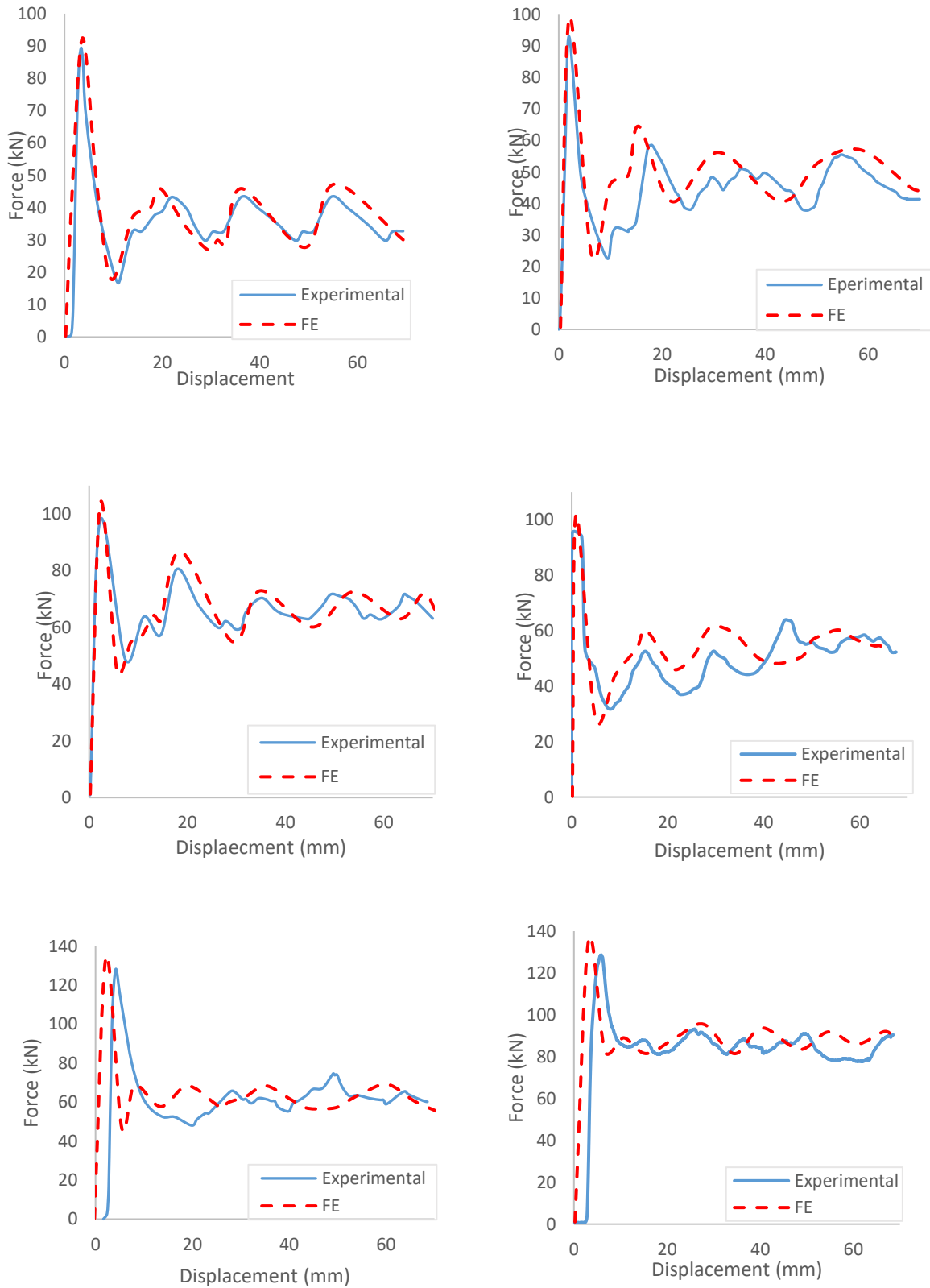
Fig. 3.14: Experimental and numerical Force-displacements histories for; a) Al-SCT, b) Al-DCT, c) AL-QCT, d) H-SCT, e) H-DCT, f) H-QCT.

Table 3.3: The material of CFRP adopted in LS-DYNA/WORKBENCH ANSYS

Density (kg/m³)	Rho	1.45
Young's modulus X direction [MPa]	E_1	121000
Young's modulus Y direction [MPa]	E_2	6800
Young's modulus Z direction [MPa]	E_3	6800
Poisson's ratio XY	ν_{12}	0.27
Poisson's ratio YZ	ν_{23}	0.4
Poisson's ratio XZ	ν_{13}	0.27
Shear modulus XY (MPa)	G_{12}	4700
Shear modulus YZ (MPa)	G_{23}	3100
Shear modulus XZ (MPa)	G_{13}	4700
Axial tensile strength (MPa)	X_T	2245.3
Axial compressive strength (MPa)	X_C	1924.06
Transverse tensile strength (MPa)	Y_T	55.6
Transverse compressive strength (MPa)	Y_C	198.5

Table 3.4: Experimental and FE results.

Specimen ID	Exp. *EA* (kJ)	Num. *EA* (kJ)	Discrepancy (%)	Exp. Peak crush force P_{max} (kN)	Num. Peak crush force P_{max} (kN)	Discrepancy (%)
Al-SCT	2.51	2.65	5.58%	89.40	92.45	3.41%
Al-DCT	3.16	3.49	10.44%	93.01	99.29	6.75%
Al-QCT	4.25	4.70	10.69%	97.64	103.89	6.40%
H-SCT	3.39	3.55	4.72%	94.05	101.86	8.30%
H-DCT	4.19	4.50	7.40%	126.29	134.65	6.62%
H-QCT	5.80	6.04	4.14%	128.60	135.60	5.44%

3.4   Conclusions

In this study, the crushing behavior and the corresponding energy absorption capabilities of metallic and hybrid thin-walled circular tubes have been studied. Hybrid CFRP/AA6061 multi-cell tubes were presented in this paper. The presented hybrid tubes were manufactured by wrapping the CFRP sheets around the Al 6061-T6 tubes. Finite element models of multi-cell tubes were conducted. The energy absorption and the peak

force of the multi-cell tubes were shown in detail. Some of the main conclusions were as following:

(1) The ply orientations of the CFRP sheets had a considerable influence on the energy absorption capacity of the hybrid tubes as CFRP sheets with orientation [0°/90°/0°/90°] improved the *EA* by 35% compared with [90°/0°/90°/0°].

(2) The number of cells controls the behavior of the hybrid and the metallic tubes. The crashworthiness parameters were improved by increasing the number of cells.

(3) For each hybrid tube, the energy absorption of the hybrid configuration exceeded the sum of those of metallic components. The novel CFRP/AA6061 hybrid quadruple-cell tube (H-QCT) was the highest of the six metallic and hybrid structures. The improvement in energy absorption of H-QCT has increased by 131.70% compared to the control AL tube.

(4) The *SEA* of the H-QCT was 70.7 % higher than the *SEA* of the Al-SCT tube. Thus, providing multiple cells within the tube and wrapping the tube with composite layers creates the most efficient energy absorber structures for blast and crashworthiness applications.

(5) Finite element simulation can be adapted to run an optimization for the design of hybrid multi-cell tubes.

(6) The hybrid multi-cell tubes can be adopted from this detailed study as a novel configuration for the core of the vulnerable sacrificial layers for protecting structures from blast hazards.

3.5   References:

1.   Guruprasad, S. and A. Mukherjee, Layered sacrificial claddings under blast loading Part I—analytical studies. International Journal of Impact Engineering, 2000. 24(9): p. 957-973.

2.   Palanivelu, S., et al., Crushing and energy absorption performance of different geometrical shapes of small-scale glass/polyester composite tubes under quasi-static loading conditions. Composite structures, 2011. 93(2): p. 992-1007.

3.   Ma, G. and Z. Ye, Energy absorption of double-layer foam cladding for blast alleviation. International Journal of Impact Engineering, 2007. 34(2): p. 329-347.

4.   Vinson, J.R., Sandwich structures. Applied Mechanics Reviews, 2001. 54(3): p. 201-214.

5.   Davies, J., Sandwich panels. Thin-walled structures, 1993. 16(1-4): p. 179-198.

6.   Li, X., et al., Response of aluminum corrugated sandwich panels under air blast loadings: experiment and numerical simulation. International Journal of Impact Engineering, 2014. 65: p. 79-88.

7.   Ahmed, S. and K. Galal, Effectiveness of FRP sandwich panels for blast resistance. Composite Structures, 2017. 163: p. 454-464.

8.   Liu, J., Z. Wang, and D. Hui, Blast resistance and parametric study of sandwich structure consisting of honeycomb core filled with circular metallic tubes. Composites Part B: Engineering, 2018. 145: p. 261-269.

9.   Liu, T., Z. Deng, and T. Lu, Design optimization of truss-cored sandwiches with homogenization. International Journal of Solids and Structures, 2006. 43(25-26): p. 7891-7918.

10.   Alghamdi, A., Collapsible impact energy absorbers: an overview. Thin-walled structures, 2001. 39(2): p. 189-213.

11.   Lu, G. and T. Yu, Energy absorption of structures and materials. 2003: Elsevier.

12.   Nia, A.A. and M. Parsapour, Comparative analysis of energy absorption capacity of simple and multi-cell thin-walled tubes with triangular, square, hexagonal and octagonal sections. Thin-Walled Structures, 2014. 74: p. 155-165.

13.   Baroutaji, A., et al., Crush analysis and multi-objective optimization design for circular tube under quasi-static lateral loading. Thin-Walled Structures, 2015. 86: p. 121-131.

14. Zhang, H. and X. Zhang, Crashworthiness performance of conical tubes with nonlinear thickness distribution. Thin-Walled Structures, 2016. 99: p. 35-44.

15. Wu, S., et al., Crashworthiness analysis and optimization of sinusoidal corrugation tube. Thin-Walled Structures, 2016. 105: p. 121-134.

16. Chen, B., et al., Experimental study on energy absorption of bionic tubes inspired by bamboo structures under axial crushing. International Journal of Impact Engineering, 2018. 115: p. 48-57.

17. Tabacu, S., Analysis of circular tubes with rectangular multi-cell insert under oblique impact loads. Thin-Walled Structures, 2016. 106: p. 129-147.

18. Zhang, X. and H. Zhang, Energy absorption of multi-cell stub columns under axial compression. Thin-Walled Structures, 2013. 68: p. 156-163.

19. Zahran, M., P. Xue, and M. Esa, Novel approach for design of 3D-multi-cell thin-walled circular tube to improve the energy absorption characteristics under axial impact loading. International Journal of Crashworthiness, 2017. 22(3): p. 294-306.

20. Huang, H. and S. Xu, Crashworthiness analysis and bionic design of multi-cell tubes under axial and oblique impact loads. Thin-Walled Structures, 2019. 144: p. 106333.

21. Mirzaei, M., et al., Experimental and analytical assessment of axial crushing of circular hybrid tubes under quasi-static load. Composite Structures, 2012. 94(6): p. 1959-1966.

22. Zhu, G., et al., On crushing characteristics of different configurations of metal-composites hybrid tubes. Composite Structures, 2017. 175: p. 58-69.

23. Sun, G., et al., Experimental investigation of the quasi-static axial crushing behavior of filament wound CFRP and aluminum/CFRP hybrid tubes. Composite Structures, 2018. 194: p. 208-225.

24. ANSYS, I., ANSYS LS-DYNA user's guide. 2017, ANSYS, Inc Pennsylvania, US.

25. Zhang, X., G. Cheng, and H. Zhang, Numerical investigations on a new type of energy-absorbing structure based on free inversion of tubes. International Journal of Mechanical Sciences, 2009. 51(1): p. 64-76.

26. Zahran, M., et al., A new configuration of circular stepped tubes reinforced with external stiffeners to improve energy absorption characteristics under axial impact. Latin American Journal of Solids and Structures, 2017. 14(2): p. 292-311.

27. Hallquist, J., LS DYNA Theoretical Manual–Livermore Software Technology. USA: Corporation Livermore, 2005.

28.   Zahran, M., et al., A novel tailor-made technique for enhancing the crashworthiness by multi-stage tubular square tubes. Thin-Walled Structures, 2018. 122: p. 64-82.

29.   Yu, H., H. Shi, and S. Chen, A novel multi-cell CFRP/AA6061 hybrid tube and its structural multiobjective optimization. Composite Structures, 2019. 209: p. 579-589.

30.   Chang, F.-K. and K.-Y. Chang, A progressive damage model for laminated composites containing stress concentrations. Journal of composite materials, 1987. 21(9): p. 834-855.

31.   Siromani, D., J. Awerbuch, and T.-M. Tan, Finite element modeling of the crushing behavior of thin-walled CFRP tubes under axial compression. Composites Part B: Engineering, 2014. 64: p. 50-58.

Chapter 4: Improving Blast Performance of Reinforced Concrete Panels using Sacrificial Cladding with Hybrid-Multi Cell Tubes

4.1   Introduction

The investigation of buildings and their structural elements capability to tolerate explosions has become an active area of research in structural engineering fields. Blast loads result from terrorist attacks and industrial or transportation-related accidents that may have flammable materials such as petroleum, propane, etc. These accidents destroy these buildings resulting in significant human casualties. Thus, protecting structures against blast hazards become inevitable for military and civilian governments in many countries.

A few of the available solutions for shielding structures against blast risks are as follows: (a) Attaching a thick concrete covering to steel members. Unfortunately, this approach has many drawbacks, such as adding a large deadweight added to the structure. Furthermore, explosion tests showed that concrete completely pulverizes and causes casualties due to flying fragmentations [1], (b) Coating the structure's internal walls by LINE-X or POLYUREA; however, this technique is costly. (c) Applying glass laminated aluminum reinforced epoxy (GLARE), a metallic sheet consisting of many very thin layers of aluminum interspersed with layers of prepreg glass-fibers, bonded with an epoxy matrix. It has excellent resistance against impact, blast loading, and fire [2]. However, this material is expensive. (d) Applying nanomaterials can contribute to the blast mitigation of concrete structures. However, producing nanomaterial is a costly process, and the quantities required for the construction industry are massive.

Recently, sacrificial cladding structures have attracted more attention as effective blast alleviation techniques due to their superior energy absorption capabilities and low cost [3-5]. The sacrificial cladding structure has two layers (an outer plate and an inner core layer), as illustrated in Fig.1a. The face plate's function is to evenly distribute the blast pressure across the crushable core layer, which gradually deforms and absorbs a large amount of impact energy. Thus, the pressure transferred to the structure is attenuated. To safeguard structures from these devasting impulses, the proposed cladding structures must be installed at the façade of those structures, as shown in Fig. 1a. During the explosion, the sacrificial cladding layers will be exposed to a high load pulse (P_0) of a short duration. The objective of the sacrificial cladding structure is to convert a high impulsive load with a short duration to a lower load with a longer duration, as illustrated in Fig. 1b. Thus, the applied load conveyed to the main structure is minimized [6, 7] to avoid permanent damage to the

unprotected structure (main structure), the failure load on the sacrificial cladding structure (Fmax) must be less than the minimum elastic capacity of the main structure. The efficiency of the sacrificial cladding structures mainly depends on the amount of energy absorbed by its core [8]. TW structures with various materials and shapes have been employed as effective energy absorber components in crashworthiness applications. They can attenuate a large portion of impact energy by converting it into plastic energy when it is deformed by the applied pressure produced by the shock wave [9]. Hence, they can be exploited as an effective core layer for sacrificial cladding structures.

Several studies have been performed to understand and evaluate the blast behavior of protected structural elements under the impact of blast loads. Hanssen et al. [10] used aluminum foam (ALF) with different densities as sacrificial layers. They found that the transmitted energy and impulse vary according to the foam density. Mazek et al. [11] experimentally and numerically investigated the performance of the RC panels with and without aluminum foam (ALF) layers and rigid polyurethane foam (RPF) layers to fortify the RC panels subjected to blast loads. The blast performance of the RC panel was improved by 45% and 70% for the panels strengthened by RPF and ALF layers, respectively, with respect to the bare RC panel. Van et al. [7] executed a detailed numerical and experimental study on the blast performance of a sacrificial cladding with various configurations of composite tubes. They found that using sacrificial cladding maintains structural integrity. Codina et al. [12] introduced a novel sacrificial cladding for minimizing blast damage of RC columns by covering the structural element with reinforced resin panels. The experimental findings implied a reduction in the final deflection compared to the un-protected column of 57.4% for the steel jacket and 66% for the reinforced resin panels. Al Rifaie et al. [13] numerically investigated the blast performance of novel sandwich panels with unconnected graded layers. They found that sandwich structures with graded layers had a superior blast performance than those with upgraded core layers.

This chapter presents sacrificial cladding structures with a core layer consisting of three different groups of hybrid multi-cell tubes. The new proposed sacrificial cladding structures were mounted in front of the RC concrete panel to enhance the RC panel's blast behavior. An unprotected RC panel exposed to close-range free air blast test executed by Wang et al. [14] was selected to be a control panel to highlight the impact of the new proposed mitigation techniques.
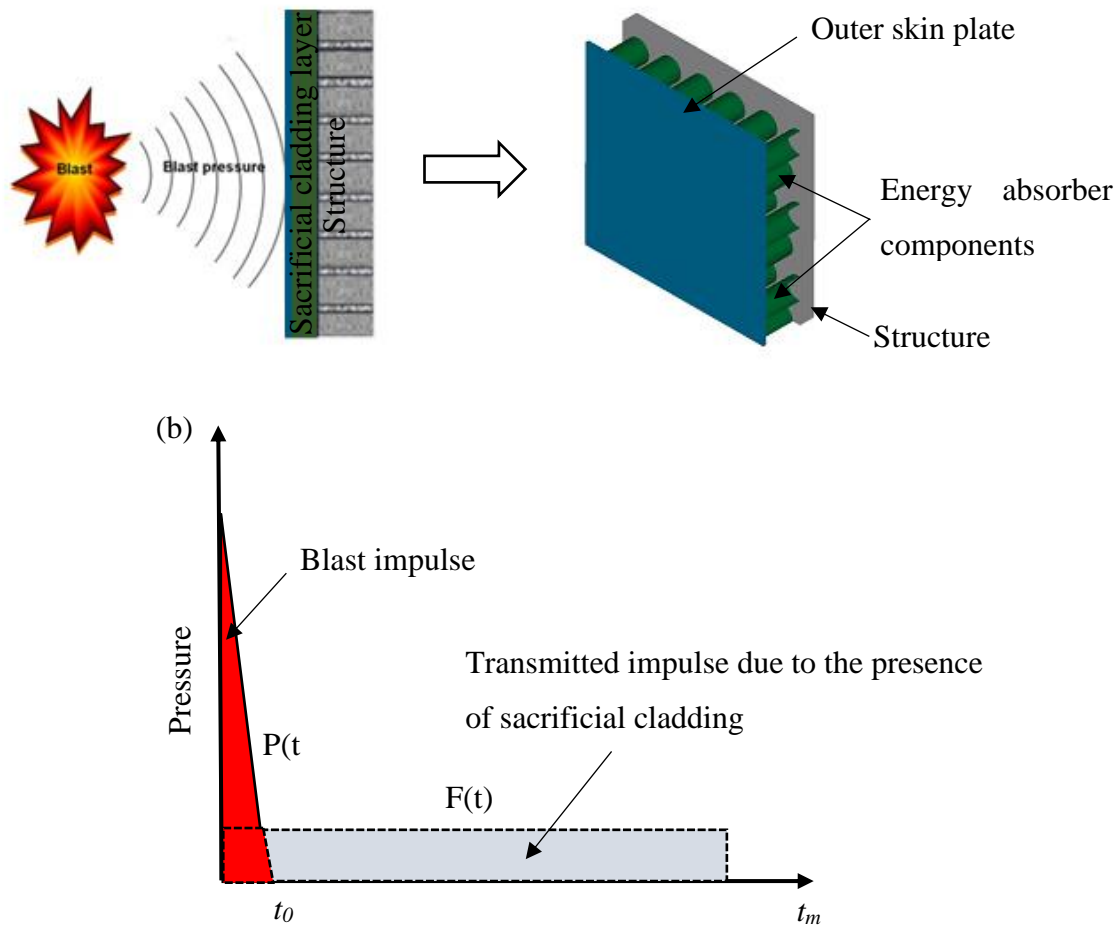
Fig. 4.1: a) Schematic of sacrificial cladding layers, b) sacrificial cladding structure concept.

4.2 Numerical model validation

Recently, numerical modeling has been replaced the blast field tests in the predesign stage of structures as well as investigating their performance under extreme load conditions. The field blast tests are reliable approach to examine the dynamic performance of blast-resistant structures. However, the blast field tests are expensive to conduct in some cases, and sometimes it is impossible to carry out such field tests because of their size, complexity, safety, and cost [15].

In this study, the numerical approach was adopted to examine the dynamic performance and the failure of the presented structures under blast loading. All numerical models were carried out by utilizing the commercial explicit finite element program Autodyn/ANSYS 2019 Version R2. Numerical results obtained by the FEA were verified by the data obtained from the field blast test executed by Wang et al. [14]. Three one-way square RC slabs subjected to close-in blast loadings with different scaled distances (Z) of 0.518 and 0.591 m/kg1/3 were considered in this study. The dimensions of the panels are shown in Table 4.1.

The setup of the field blast test is shown in Fig. 4.2.a. The specimens' reinforcements were constructed using 6 mm steel bars in both directions with the spacing of 75 mm in-between bars, as shown in Fig. 4.2.b. The reinforcement ratio in both directions was 1.43%. The concrete had a compressive strength of 39.5 MPa, tensile strength of 4.2 MPa, and Young's modulus of 28.3 GPa. The reinforcement had a yield strength of 600 MPa and Young's modulus of 200 GPa. The test rig was constructed, as illustrated in Fig. 4.2. The RC slabs were fixed on the sides to avoid lifting during testing [14]. TNT explosive charges were hung above the center point of the specimens at a specific stand-off distance (*SoD*) [300, 400, and 500 mm] measured from the center of the explosives to the upper surface of the slab. Table 4.1 summarizes the experimental program.

Table 4.1: Blast field test data [13].

Panel	Dimensions (mm)	Charge weight (gm)	*SoD* (mm)	Z (m/kg1/3)
Panel A	750×750×30	130	300	0.591
Panel B	750×750×30	190	300	0.518
Panel C	1000×1000×40	310	400	0.591
Panel D	1000×1000×40	460	400	0.518
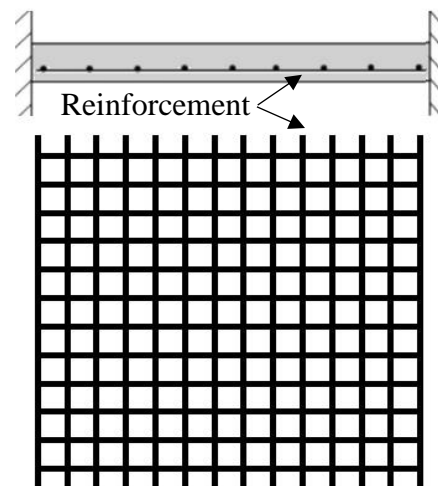
Fig. 4.2: a) Setup of the experimental blast test [13], b) Slab cross-section and reinforcement.

4.3   Numerical Modeling

4.3.1   Material models

4.3.1.1 Concrete model

Dynamic modeling for concrete structures exposed to blast load still a challenge and needs high fidelity computer simulations. It is important to have a precise finite element model representing concrete material characteristics for the high-stress rate effect. In this study, Riedel-Hiermaire-Toma (RHT) model was utilized to simulate the hydrodynamic behavior and crack trajectory of the concrete under the impulsive blast load. RHT model is a complex plasticity model established by Riedel et al. [16] and adopted for brittle materials (concrete). This model considers numerous features, for instance, strain hardening, pressure hardening, strain softening, strain rate hardening, and third invariant dependence. The RHT model adopts three strength surfaces to define the failure surface, elastic limit surface, and residual surface, as shown in Fig. 4.3.
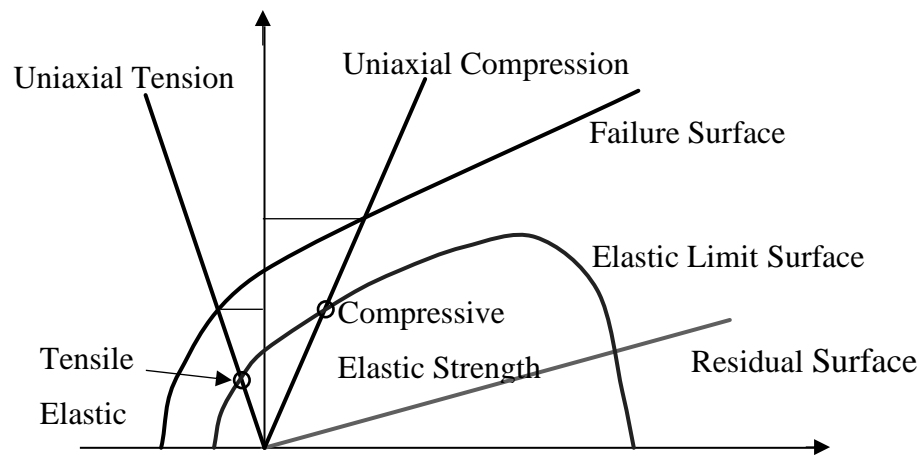
Fig. 4.3: Three strength surfaces of RHT model [16].

The failure surface Y_f can be expressed as a function of pressure P, the lode angle θ, and strain rate $\dot\varepsilon$,

$$Y_{fail}(p^*, \theta, \dot\varepsilon) = Y(p^*) \times R_3(\theta, p^*) \times F_{rate}(\dot\varepsilon) \tag{4.1}$$

where $Y(p^*)$ is the compressive meridian and is defined as:

$$Y(p^*) = f_C \times [A\,(p^* - p^*_{spall} \times F_{rate}(\dot\varepsilon))\,N] \tag{4.2}$$

in which f_c is the material's uniaxial compressive strength, A is the failure surface constant, p^* is the pressure normalized by f_C, $p^*_{spall} = p^*(f_t/f_C)$ (f_t is the material's uniaxial tensile strength), $F_{rate}(\dot\varepsilon)$ stands for the dynamic increase factor (*DIF*) function, and N is the

failure surface exponent. $R_3(\theta, p^*)$ is the failure surface (Y_{fail}) reduction factor, which is a function of the Lode angle (θ). The elastic limit surface is scaled from the failure surface,

$$Y_e = Y_{fail} \times F_e \times F_{cap} \tag{4.3}$$

where F_e is the ratio of the elastic strength to failure surface strength. F_{cap} controls the elastic deflection stresses under hydrostatic compression and fluctuates in the range of (0,1).

The residual failure surface is defined as:

$$Y_{residual} = f_C \times B \times (p^* / f_C)\, M \tag{4.4}$$

Where B is the residual failure surface constant, and M is the residual failure surface exponent.

The parameters (B and M) control the residual stress and affect the post-failure surfaces. while D_1, D_2 and e_{min}^{fail}, as illustrated in Eqs. (4.5), (4.6), and (4.7) control the concrete post-softening behavior.

$$D_1 = \int_0^{\varepsilon_p} \left(\frac{\Delta\varepsilon_p}{D_1 \left(P^* - P_{spall}^* \right)^{D_2}} \right) \quad \text{for } D_1 \left(P^* - P_{spall}^* \right)^{D_2} > e_{min}^{fail} \tag{4.5}$$

$$D_2 = \int_0^{\varepsilon_p} \left(\frac{\Delta\varepsilon_p}{e_{min}^{fail}} \right) \quad \text{for } D_1 \left(P^* - P_{spall}^* \right)^{D_2} < e_{min}^{fail} \tag{4.6}$$

$$e_{min}^{fail} = \frac{2G_f}{\sigma_t \times L_{eq}} \tag{4.7}$$

G_f; is the fracture energy; σ_t; is the tensile failure stress, and L_{eq}; is the characteristic length of the element (the diameter of a sphere with the exact size of the *3D* element [17]).

The modified concrete model adopted in this research is illustrated in Table 4.3.

4.3.1.2 Material model for reinforcement steel

The Johnson and Cook's material model was utilized to simulate the reinforcement steel [18]. This model is ideal for material under high strain rates and elevated temperatures. The model of its flow stress is expressed by Eq. 4.8:

$$\sigma_y = [A + B(\varepsilon_p^{eq})^n][1 + c\,ln(\frac{\dot{\varepsilon}_p^{eq}}{\dot{\varepsilon}_0})][1 - (T^*)^m] \tag{4.8}$$

where σ_y is the dynamic stress, ε_p^{eq} and $\dot{\varepsilon}_p^{eq}$ are the equivalent plastic strain and equivalent plastic strain rate, respectively. While m is the thermal softening exponent. *A*, *B*, *n*, *c*, $\dot{\varepsilon}_0$, and m are constants obtained from the flow stress data. T* is the homologous temperature calculated from Eq. 4.9.

$$T^* = \frac{T - T_r}{T_m - T_r} \tag{4.9}$$

T is the material temperature, T_m is the material melting temperature, and T_r is the room temperature. To capture the rupture of the reinforced concrete, a failure criterion was adopted on the basis of equivalent plastic strain.

The constants of the steel material developed in this research were obtained from data of steel 4340 material. The mechanical properties are bulk modulus, K = 159 GPa; reference density, ρ = 7.83 g/cm³; reference room temperature, T_{room} = 300 K; specific heat = 477 J/kg K; shear modulus, G = 81.8 GPa; yield stress, A = 792 MPa; hardening constant, B = 510 MPa; hardening exponent, n = 0.26; strain rate constant, C = 0.014; thermal softening exponent, m = 1.03; and melting temperature, T_{melt} = 1793 K.

4.3.1.3 Material model for Air and TNT

In blast models, the surrounding air and the product of the TNT explosion were assumed to behave like an ideal gas. An ideal gas equation of state (*EOS*) was used to describe air and was expressed by:

$$P = (\gamma - 1)\rho_g e_0 \tag{4.10}$$

where P is the hydrostatic pressure, γ is the ideal gas constant and is 1.4 for air, ρ_g is the density of the air, and e_0 is the specific internal energy. The internal energy of air was used as 2.068×10^5 kJ/kg. This internal energy initialized the air medium to an atmospheric pressure of 101.3 kPa.

The Jones–Wilkins–Lee (JWL) equation of state was used to model high explosive material such as TNT [18], which is in the form of:

$$P = A\left(1 - \frac{\omega}{R_1 V}\right)e^{-R_1 V} + B\left(1 - \frac{\omega}{R_2 V}\right)e^{-R_2 V} + \frac{\omega E}{V} \tag{4.11}$$

where *A, B, R_1, R_2*, and ω are empirically derived constants that depend on the type of explosives, V is the volume of charge, and E is the detonation energy per initial unit volume [20]. TNT's material properties used in the present study *A, B, R_1, R_2,* and ω are 373.75 GPa, 3.747 GPa, 4.15, 0.9, and 0.35, respectively.

Table 4.2: Constitutive material models adopted in *Autodyn.*

Reinforced concrete (*p- α EOS*, *RHT* strength, *RHT* failure)			
EOS	*p- α*	Compressive strength, f_c *(MPa)*	39.5
Reference density *(kg/m³)*	2.75×10^3	Tensile strength, ft/fc	0.1
Porous density *(kg/m³)*	2.31×10^3	Failure surface constant, *A*	1.6
Porous sound speed *(m/s)*	2.92×10^3	Failure surface exponent, *N*	0.61
Initial compaction pressure, *(GPa)*	0.0233	Meridian ratio, *Q*	0.68

Solid compaction pressure, (*GPa*)	6.0	Brittle to ductile transition	0.0105
Compaction exponent	3.0	Fractured strength constant, B_c	1.6
Bulk modulus, A_1 (*GPa*)	35.27	Fractured strength exponent, M_c	0.61
Parameter, A_2 (*GPa*)	39.58	Damage constant, D_1	0.04
Parameter, A_3 (*GPa*)	9.04	Damage constant, D_2	1.0
Parameter, *Bo*	1.22	Minimum strain to failure	0.01
Parameter, B_1	1.22	Residual shear modulus fraction	0.13
Parameter, T_1 (*GPa*)	35.27	Principal tensile failure stress (*GPa*)	0.015
Parameter, T_2 (*GPa*)	0.0	Fracture energy, G_f (*J/m²*)	100.0
Reference temp. *(K)*	295.0	Erosion criteria	Geometric strain
Specific heat (*J/kg K*)	654.0	Erosion limit	0.60

<div align="center">Reinforcement steel bars (Linear EOS, Johnson cook strength)</div>

Reference density (*kg/m³*)	7.83×10^3	Strain rate constant, c	0.014
Bulk modulus (*GPa*)	159	Thermal softening exponent, m	1.03
Shear modulus (*GPa*)	81.8	Indoor temperature, $T_m(K)$	300
Yield stress, A(*GPa*)	0.792	Melting temperature, $T_r(K)$	1793
Hardening constant, B(*GPa*)	0.51	Ref. strain rate, ε^0	1
Hardening, exponent, n	0.26		

<div align="center">Al 6061-T6 (linear EOS, Johnson cook strength, plastic strain failure)</div>

Reference density (*kg/m³*)	2.7×10^3	Strain rate constant, c	0.01
Bulk modulus (*GPa*)		Thermal softening exponent, m	1
Shear modulus (*GPa*)	27.6	Indoor temperature, $T_m(K)$	300
Yield stress, A(*GPa*)	0.34	Melting temperature, $T_r(K)$	1220
Hardening constant, B(*GPa*)	0.32	Failure	plastic
Hardening, exponent, *n*	0.41	Plastic strain	0.42
Ref. strain rate, ε_0	1		

<div align="center">GFRP composite (ortho EOS, elastic strength)</div>

Reference density, (*kg/m³*)	1.45×10^3	Shear modulus, G_{12} (*GPa*)	4.70
Young's modulus, E_{11} (*GPa*)	12.10	Shear modulus, G_{23} (*GPa*)	3.10
Young's modulus, E_{22} (*GPa*)	6.80	Shear modulus, G_{31} (*GPa*)	4.70
Young's modulus, E_{33} (*GPa*)	6.80	Tensile failure stress, f_{u11} (*GPa*)	0.261
Poisson's ratio, $\nu_{12,}\ \nu_{13}$	0.27	Tensile failure stress, f_{u22} (*GPa*)	0.0261
Poisson's ratio, ν_{23}	0.4	Erosion criteria	Material failure

4.3.1.4 Numerical model

For blast loading, the shock wave interacts with the structure through fluid-structure interaction (FSI). Explicit finite element programs are able to simulate this kind of interaction. In this research, all the numerical simulations were performed utilizing ANSYS/Autodyn V-19. R2. which is engineering hydrocode software designed to solve nonlinear dynamic problems, using Eulerian, Lagrangian, and Arbitrary Lagrange‑Euler (ALE) solvers [17].

The computational cost of the 3D model for explosion simulations is quite expensive (consuming time and needing high computer storage). Two techniques were adopted in this study to overcome this problem while maintaining precise results. The first was taking advantage of symmetry, by modeling one quarter of the structure. The second was using the remapping technique. This technique allows a 2D model with fine mesh to be mapped into a 3D model with a coarser mesh. The remapping is usually done through a 2D axisymmetric model with a 1mm element size to simulate the detonation of the explosive charge, as shown in Fig. 4. The 2D model was run until the shock vector just before reaching the concrete panel. Next, a remap file was created and then imported to fill the 3D Eulerian domain (air block) as an initial condition, as shown in Fig. 4.5.

The Lagrange solver was employed to simulate solid continua (concrete panel) as the mesh move with the material distortion. The Euler solver was adopted to model the gas flow resulting from an explosion as the Euler model assumes that the material can flow through a fixed grid. At the same time, beam element was utilized to simulate the reinforcement steel bars. The FE model consists of air domain in which the explosion was initiated. The Euler sub-grid (air domain) boundary condition was set as a flow-out boundary at the four faces of the air block, as illustrated in Fig. 5. In the area supporting the slab, a fixed boundary condition was applied by restraining all the translational degrees of freedom for the nodes located on that edge. A reinforcement bond is considered between the steel bars and the concrete. And the element size was selected to be 5 mm to attain consistent results. This size was selected relying on an executed mesh sensitivity study. The erosion technique was implemented to model the severe damage that occurred to the panels, such as spalling that might occur at the slabs' bottom surface. An instantaneous geometric strain of 0.6 was adopted in this study.
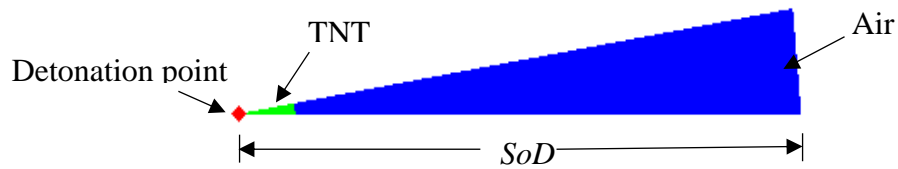
Fig. 4.4: Geometry of 1D wedge filled with TNT and air with axial symmetry.
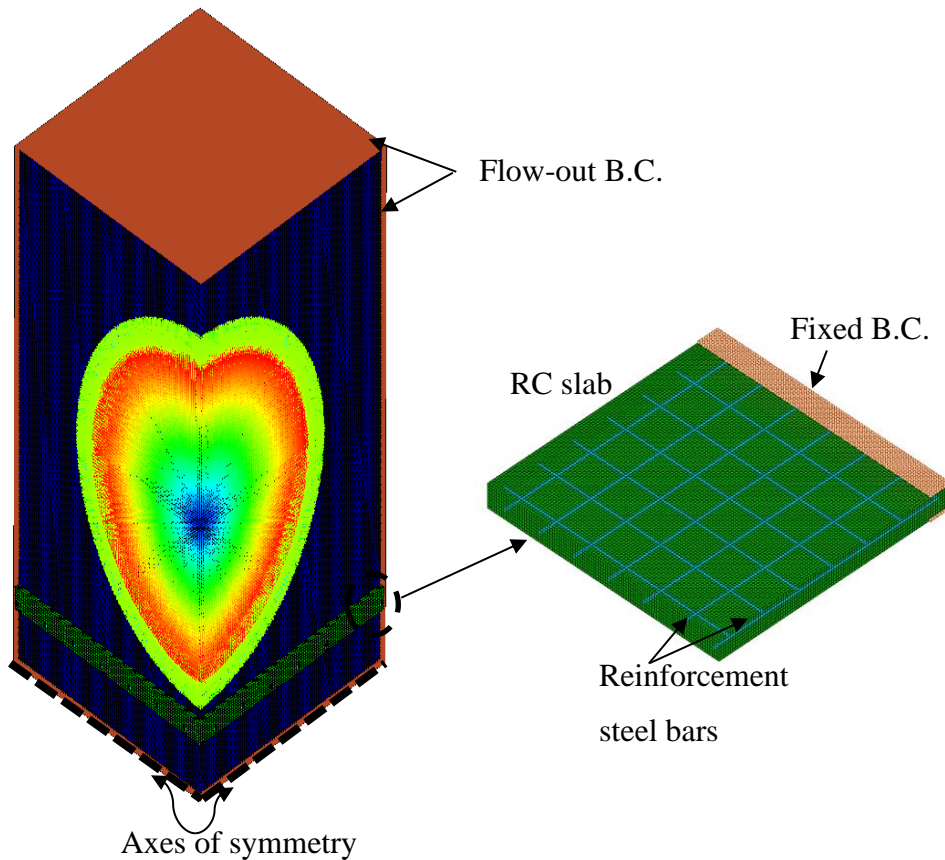
Fig. 4.5: 3D FE model for RC panels under blast impact.

4.3.2 Results and discussion

4.3.2.1 Midspan deflection of the panels

The displacement-time histories at the mid-span of the concrete panel structures due to blasting load were captured using the finite element models, as shown in Fig. 4.6. The performance of the RC panels was investigated under the effect of ignition of several TNT charges at different SoD, as stated in Table 4.1. In each case, the displacement-time history at the mid-span is plotted. Panels exhibit more extensive deformation in conjunction with the increasing TNT charge. Panel A attained 8.74 mm residual deformation obtained from the numerical simulation whereas, the experimental residual displacement was 9 mm with

an error of around 3%. Panel B showed 25.4 mm central residual deflection versus 26 mm based on the experimental result with a difference of 2.3%. In addition, panel C showed 14.8 residual central deflections compared to a 15 mm resulting from the experiments with a discrepancy of 1.3%. Finally, Panel D demonstrated 33.5 mm residual displacement while it deflected by 35 mm in the field blast test with a difference of 4.2%. The central numerical deflections are less than the experimental deflections, and this difference may be due to the boundary conditions are always an idea in the numerical simulation, and also a full bond assumed between the concrete and the rebars. However, these ideal conditions do not exist in the field test.
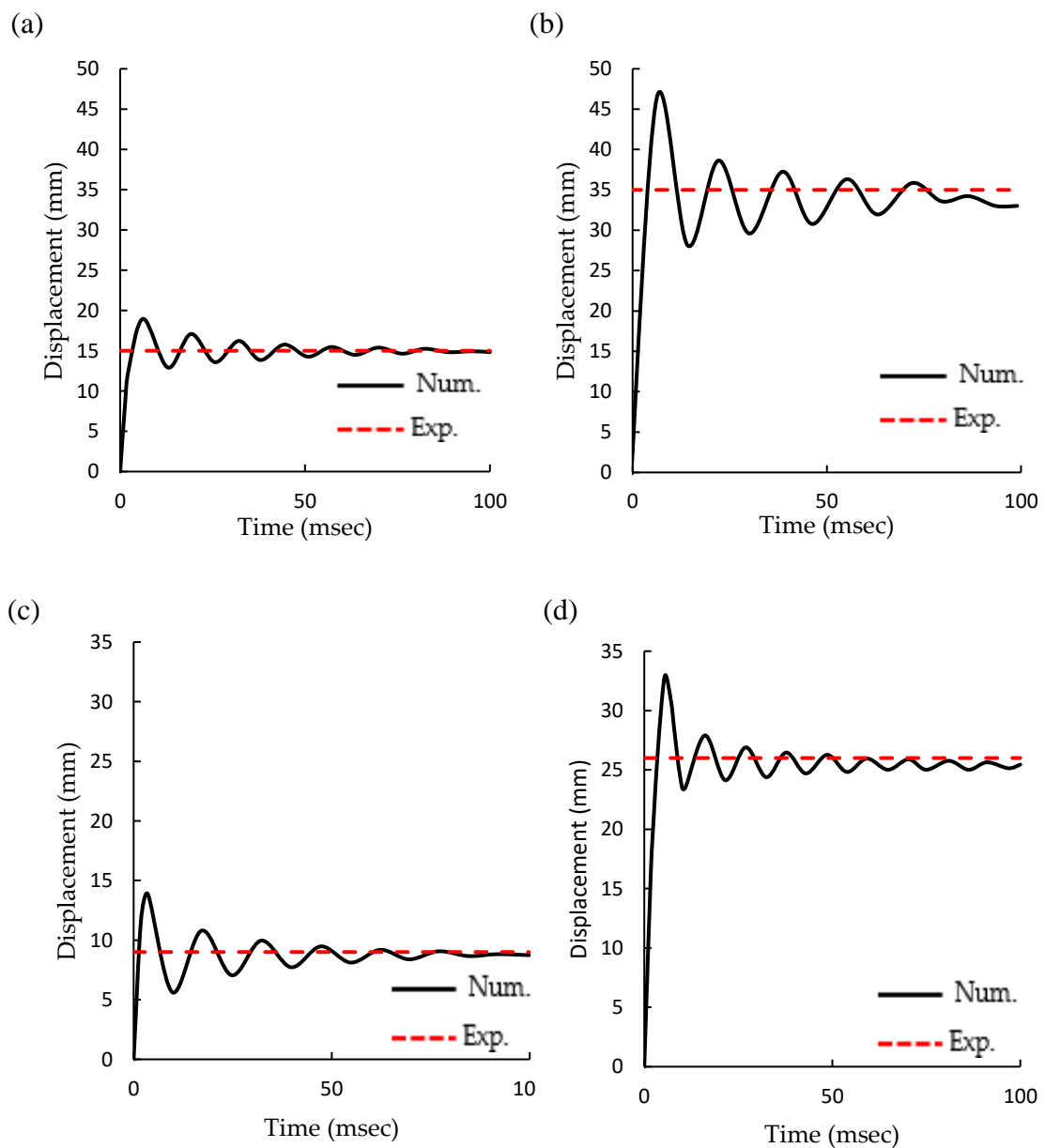

Fig. 4.6: Numerical displacement time history and experimental deformations for; a) Panel A, b) Panel B, c) Panel C, d) Panel D.

4.3.2.2 Damage patterns

Figures 4.7 and 4.8 show that the damage that occurred at the top and bottom faces of the concrete slabs. The damage level rises with increasing the TNT charge. For comparison purposes, the damage contours obtained from numerical simulations and the damaged experimental panels were displayed. The damaged areas for the top of the panels are as follos; those from Panel A under a 0.13 kg TNT charge and with SoD 0.3 m showed no evident damage, except for some minor cracks at the center of the slab surface. For panel B subjected to the detonation of 0.19 kg TNT charge with SoD 0.3 m, several small cracks were also observed in the center area, which resulted from the high pressure of the explosion. Panel C, under the impact of 0.31 kg TNT charge with SoD 0.4 m, showed a 3 mm crack through the mid-span of the slab. For panel D, there were circular and radial cracks with a small damaged area in the center of the upper side of the slab, matching the test results. In the numerical simulation, only cracks occurred at the top surface of the concrete panels while the bottom surface experienced spalling.
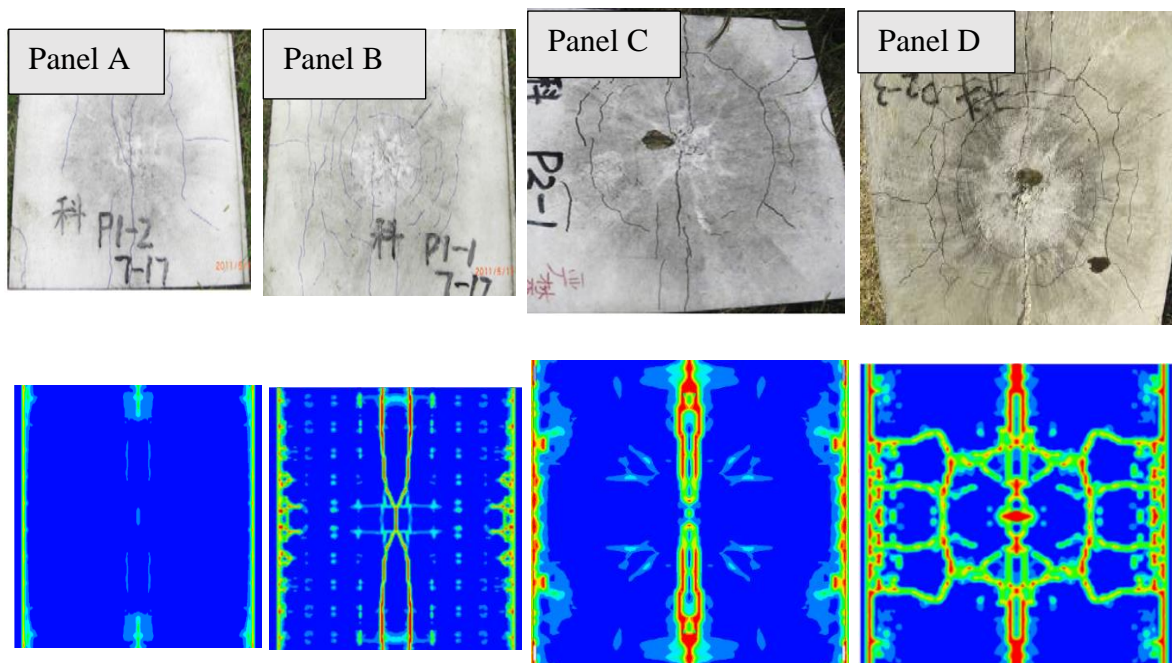

Fig. 4.7: The upper surface damage of the RC slabs; a) Experimental examination [13], b) FE simulations.
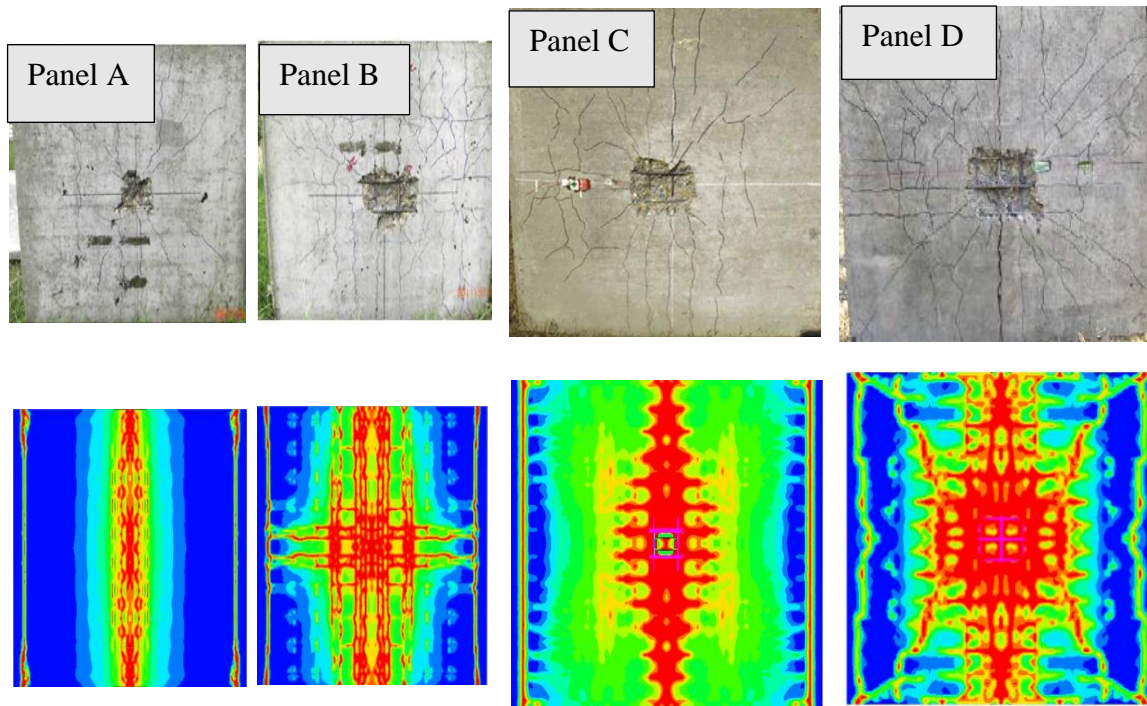
Fig. 4.8: The bottom surface damage of the RC slabs; a) Experimental examination [13], b) FE simulations.

The bottom surface of the slab panels suffered from higher damage compared to the upper surface. The bottom damage area and patterns are shown in Fig. 8, which compares the damaged areas for the panels' bottom surface obtained from the numerical simulation and the field blast tests. Panel A spalled with a radius of 45 mm lower than the exact value by 10%. For panel B, the numerical simulation presents the radius of the damaged area as 95 mm, which is wider than the experimental damage radius by 11.7%.

Similarly, spalling occurred on panel C's bottom surface in the test, as shown in Fig. 4.8. The computed damage area was approximately 100 mm with a 10% discrepancy from the test results, which is in good agreement with the numerical approach. This panel experienced moderate damage.

Spalling also occurred in panel D bottom surface as illustrated in Fig. 4.8. The computed damage area on the lower surface was approximately 135 mm, wider than the experimental by about 12.5%. The slab also showed severe damage. The numerical radii of the spalled area were slightly larger than the experimental test, which might be due to erosion arithmetic and material constants. Nevertheless, these differences are within the limit and reasonable to assess the blast performance of the panels. Table 4.3 illustrates the experimental and simulation results.

Table 4.3. Experimental test and numerical model results.

Panel	Mid-span deflection (mm)		Discrepancy (%)	Spall radius (mm)		Discrepancy (%)
	Exp. [13]	Numerical		Exp. [13]	Numerical	
Panel A	9	8.74	3.0%	50	45	10.0%
Panel B	26	25.4	2.3%	85	95	11.7%
Panel C	15	14.8	1.3%	90	100	10.0%
Panel D	35	33.5	4.2%	120	135	12.5%

Panel D was selected to highlight the competence of the new proposed sacrificial cladding structures for protecting RC panels from blast hazards.

4.4   Proposed Sacrificial cladding structure

This section presents a sacrificial cladding structure consisting of a set of thin-walled hybrid structures. Numerical models have been analyzed for three configurations of the hybrid tubes; hybrid single cell tube (H-SCT), hybrid double cell tube (H-DCT), and hybrid quadrable cell tube (H-DCT) as illustrated in Fig. 4.9. It is crucial to determine the behavior and characteristics (energy absorption, deformation pattern, peak crush load, etc.) of the standalone crushable core layer before designing a full-scale cladding structure. The authors themselves have investigated the energy absorption capabilities for metallic and hybrid multi-cell tubes [21]. They all showed a progressive crushing performance and desirable energy absorption capacity compared to solo metallic tubes. The sacrificial layer is designed with r (tube radius) distance in-between tubes, as shown in Fig. 4.9. To allow the incidence of the progressive failure of the core layers. The core layer was covered with a front skin sheet made of aluminum with a 2 mm thickness. In contrast, the core layers presented in this study were fabricated from hybrid tubes wrapped with four uni-directional CFRP sheets. The CFRP layers had [$0^\bullet/90^\bullet/0^\bullet/90^\bullet$] layout around the AA6061-T6 tubes with three different configurations as illustrated in Fig. 4.9. The tubes' dimensions were 1.2 mm wall thickness, 60 mm inner diameter, and 120 mm in total length. The inner ribs were done to suit the tubes' inward diameter to obtain the desired multi-cell tubes' configuration. The RC panel's blast performance was numerically investigated utilizing ANSYS/Autodyn. Panel D experienced the highest level of damage, so it was selected to highlight the effectiveness of the new

proposed sacrificial cladding structures for protecting RC panels from blast hazard. four-noded Belytschko-Tsay shell elements were used to model the front skin plate and the metallic tubes; however, a composite shell was adopted to represent the wrapped composite sheets. The RC panel was modeled as specified before. In the model, stress-criteria breakable bonded face connection was assumed between the structural elements (front skin, metallic tubes, CFRP tubes, and RC panel). The failure parameters listed in Table 3 were assumed for different breakable contact types. The constitutive models for the materials are listed in Table 3. The whole structure was located in the modeled air domain and exposed to the blast loading produced by detonating 0.46 kg of TNT located at 0.4 m from the upper surface of the concrete and 0.386 m from the front skin plate.
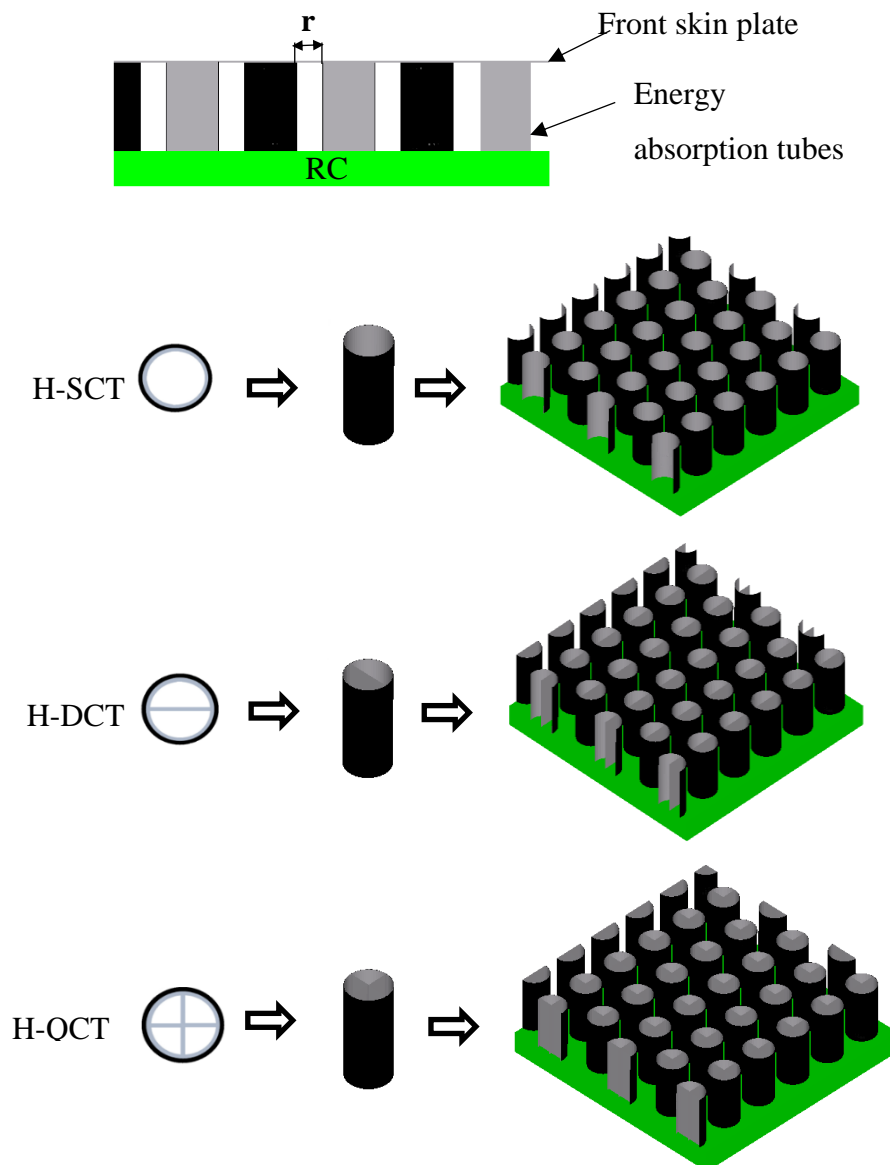

Fig. 4.9: Schematic and inner core structures of the proposed sacrificial cladding layers.

4.5   Blast performance of Protected RC panels

ANSYS/Autodyn V-19.0. R2 was also adopted to study the dynamic performance of the protected RC panels subjected to the impact of blast loading. The blast wave firstly struck the front skin plate, where fluid-structure interaction (FSI) took place. The front skin face acquired an initial velocity once the shock wave impacted on it and deformed. Then, the skin plate distributed the blast load more evenly on the core layer which was shaped from hybrid multi-cell thin-walled tubes. The tubes mitigated a significant portion of the blast load (pressure) through the AL components' progressive plastic deformation and the wrapped CFRP layers' delamination and fracture. Consequently, the pressure was attenuated before it reached the RC panel. The entire structure went into oscillation until the kinetic energy was gradually dispersed by stretching, and plastic bending. Finally, the panels underwent residual deformation, as shown in Fig. 10.

In this study, the plastic deformation and damage patterns were displayed to highlight the effectiveness of applying novel sacrificial cladding structures to the concrete structures. Figure 10 shows that the RC panel shielded with sacrificial layer has attained residual deformations of 12.69, 7.31, and 4.52 mm for H-SCT, H-DCT, and H-QCT cores, respectively. It is concluded from the results that the front skin plate suffered from larger deformations than the RC deformation due to the energy dissipated by the cladding structure cores. Thus, a sacrificial cladding structure is a distinctive approach to protect structures from blast hazards. Also, damage patterns were displayed in Fig. 4.11. Applying this technique is very useful as the cladding structure prevents the RC panel from spallating and the bottom of the RC panels only had tiny cracks. The level of damage gradually decreased from extreme damage for the bare concrete to just tiny cracks for the RC panel protected by H-QCT sacrificial structure. Table 4.4 indicates the damage level for the protected and unprotected RC panels.
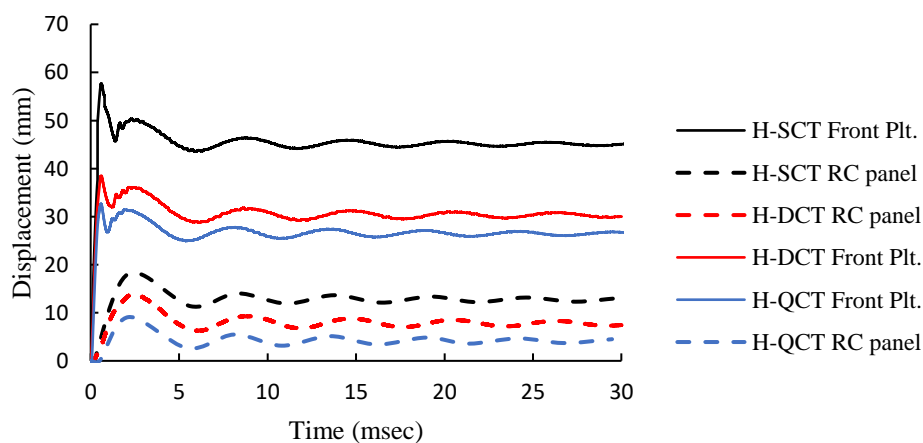
Fig. 4.10: Mid-span displacement time history for Panels with different cladding structures (H-SCT, H-DCT, and H-QCT cladding structures).

(a)
(b)
(c)
(d)
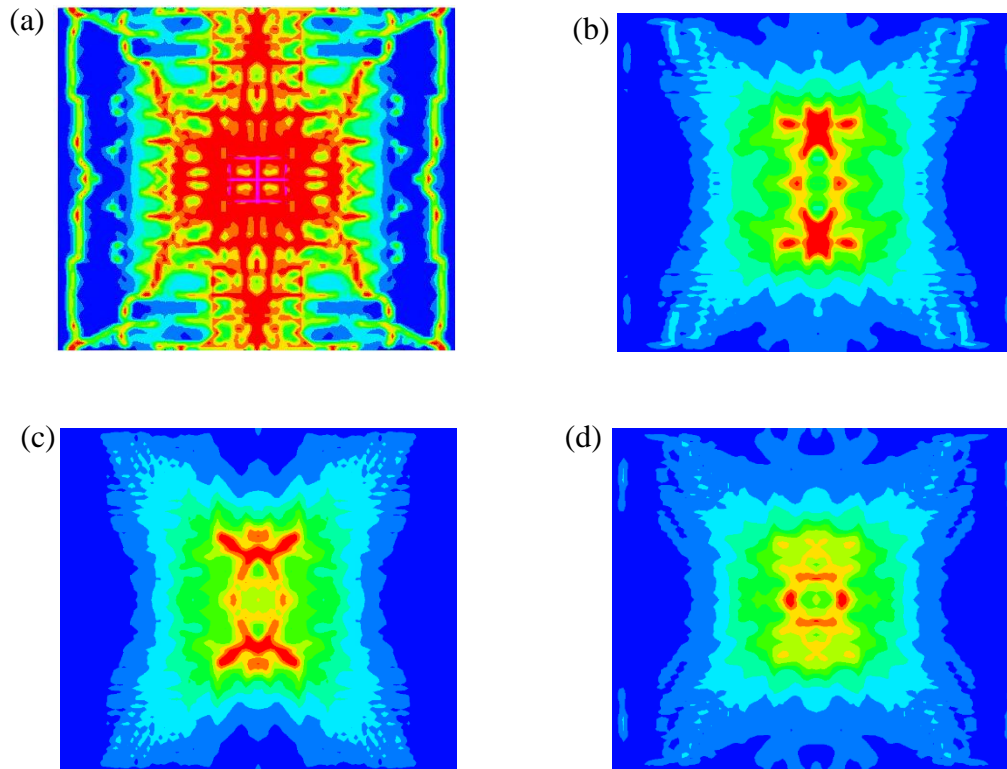
Fig. 4.11: Damage patterns on the lower surface of the RC slabs: a) un-protected panel, b) Panel with H-SCT cladding structure, c) Panel with H-DCT cladding structure, d) Panel with H-QCT cladding structure.

Table 4.4: Panels' damage levels.

Panel	Damage level
Un-protected RC panel	Severe damage
H-SCT protected panels	Moderate damage
H-DCT protected panels	Low damage
H-QCT protected panels	Low damage

Also, the sacrificial cladding layers were compared with previously implemented sacrificial cladding structures in order to highlight the effectiveness of the cladding structures presented in this study. The improvement for the final maximum deflections was used to assess the difference between other systems and the proposed technique, as displayed in Table 4.5.

Table 4.5: Improvement percent for different cladding systems.

Reference	Cladding Structure	Improvement
Mazek et al. [11]	rigid polyurethane foam (RFP) cladding layers	45.0%
	Aluminum foam (ALF) cladding layers	70.0%
Codina et al. [12]	Steel jacketing	57.4%
	Reinforced resin panels	66.0%
Current work	H-SCT cored layers	62.0%
	H-DCT cored layers	78.0%
	H-QCT cored layers	87.0%

4.6   Effect of front plate thickness variation on the blast behavior of the sacrificial layers

The front skin plate has a crucial contribution to the sacrificial cladding structures' behaviour as it is responsible for distributing the impact load on the core layer. Thus, this study was extended to investigate the influence of varying the front plate thickness on the cladding structures' blast behavior. Four different front plate thicknesses were applied 2, 4, 6, and 8 mm. The peak deformation of the skid plate and the relative energy dissipated by each core configuration were numerically calculated and are displayed in Figures 4.12-4.14. The energy dissipated by the core layer came out from the variance between the total energy (ET) and the initial energy (EI). Figure 12 demonstrates the peak deflections for the four different scenarios of the H-SCT cores and the energy dissipated by them. The results show that the contribution of the front skin sheet was significant for the peak deflections of the front plate. Overall, the peak deflection has decreased by increasing the front skin thickness (reduction of about 74.5% by increasing the thickness from 2 mm to 8 mm). In comparison, it had less effect on the RC panels' peak deflection as it was decreased by 40%. For the energy dissipated by the core layer, increasing the front skin thickness had a negative impact on it as the energy was dissipated by the core layer reduced by 90.8%. For H-DCT cores, the results followed the same trend as peak deflection, where the energy of the front plate has decreased by 58%, and the peak deflection of the RC panel has also decreased by 33.1%. In addition, the energy dissipated by the tubes was reduced by 92.8%, as shown in Fig. 4.13. Figure 4.14 displays the results obtained for the H-QCT cores. The peak deflection of the front plate has decreased by 53.5%, and the peak deflection of the RC panel decreased by

64.8%. Also, the energy dissipated by the tubes decreased by 85.8%. The results indicate that when using a 2 mm thick front plate shell, the energy dissipated attains the highest value and decreases until it reaches the minimum when the front plate thickness is 8 mm. The energy dissipation decreases when the thickness of the front panel increases. In conclusion, sacrificial cladding structures with a thin front skin plate improve the energy absorption capabilities of the structure. However, under intense blast loading, the thinner front face may rupture.
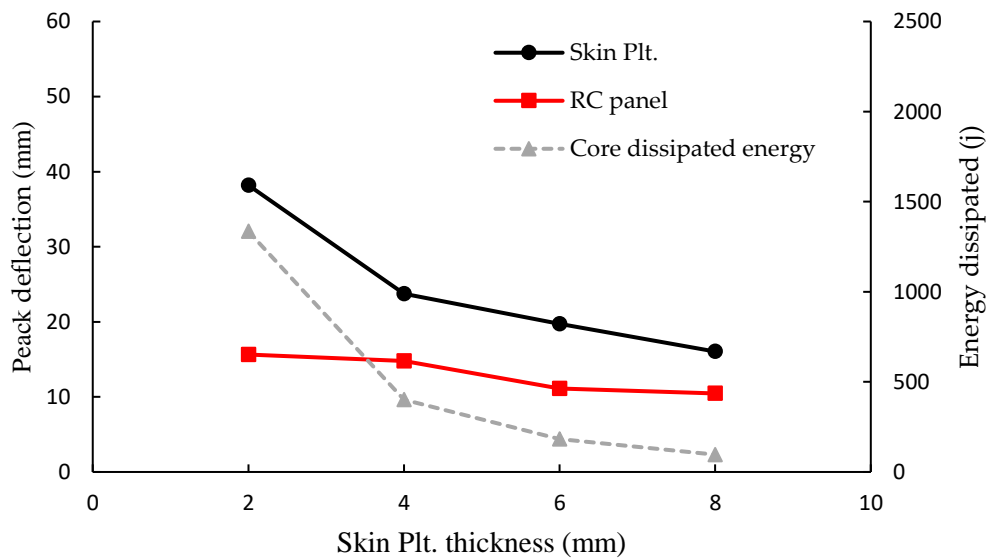

Fig. 4.12: Peak deflections and energy dissipated with skin plate thickness variation for RC Panel with H-SCT cladding structure.
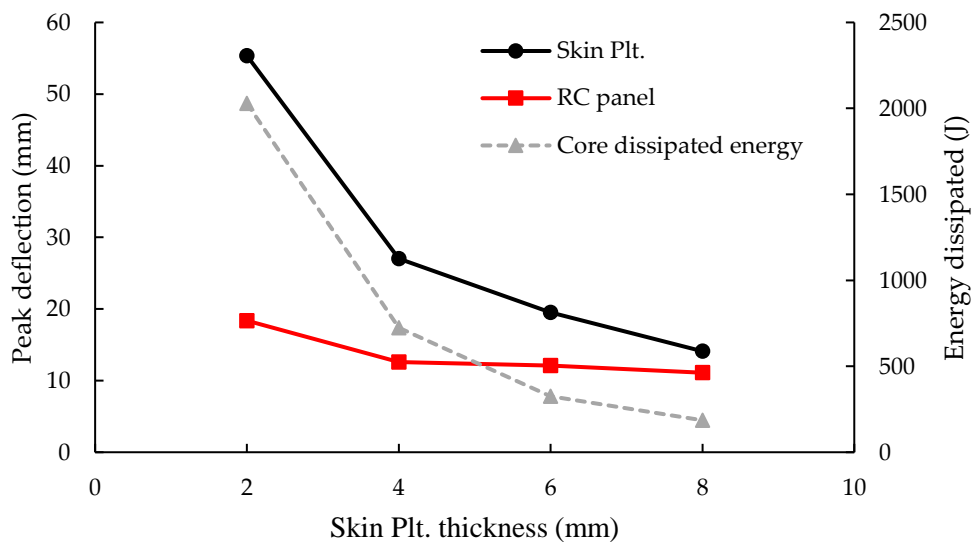
Fig. 4.13: Peak deflections and energy dissipated with skin plate thickness variation for RC Panel with H-DCT cladding structure.
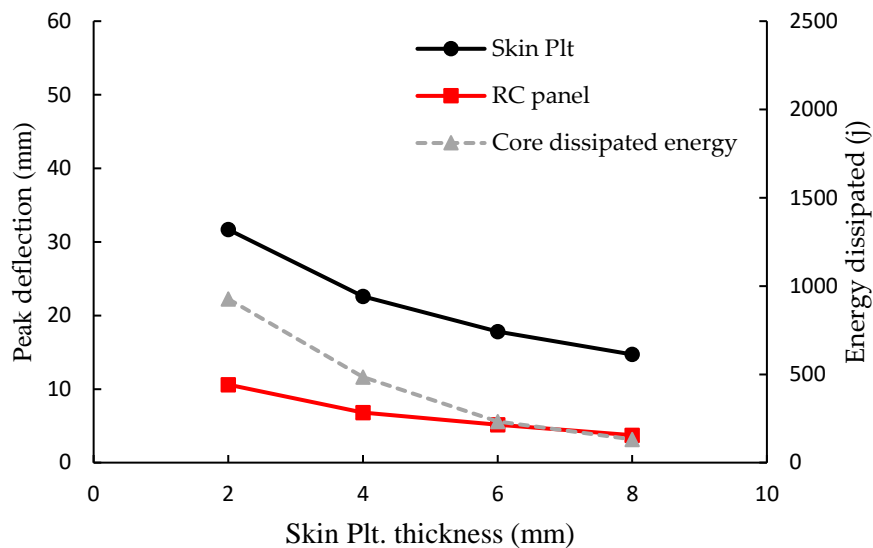

Fig. 4.14: Peak deflections and energy dissipated with skin plate thickness variation for RC Panel with H-QCT cladding structure.

4.7   Conclusion:

This study's main contribution is to present a new sacrificial structure with hybrid multi-cell tubes as an effective energy absorber component. The sacrificial structure has been proposed for protected and unprotected concrete panels. Numerical simulations of four blast tests were executed to verify the damage patterns of RC panels subjected to a close-in blast loading under various TNT charges. Non-linear 3D explicit FE models consisted of air domain, explosive, and RC slab (reinforcing steel bars inside plain concrete), were generated to validate experimental results obtained by Wang et al. [14]. The advanced models of concrete material and reinforcing bars, taking into account the effects of the high strain rate and proper coupling interface between the Euler and Lagrange elements (the explosion domain and the structure), were exploited to simulate the RC slab's dynamic behavior. The erosion technique was also used to model the damage process.

A good agreement was accomplished through numerical models to predict the deformation/damage patterns of the blast field-tested panels. Results were attaining a maximum deviation of 4.2% and 12.5% for the mid-span deflection and spall radius, respectively. The behavior of the proposed protective structures was invcestigated under the same conditions as the experimental tests to highlight the effectivness of using sacrificial

cladding structures. Three different core configurations (H-SCT, H-DCT, and H-QCT) were adopted as core layers for the cladding structures. The dynamic performance of the protected RC panels was studied under in-close blast load by adopting a nonlinear explicit finite element model. Results revealed that the cladding structure attained a desired protection for the RC panel as the residual deformations decreased by 62%, 78%, and 87% for H-SCT, H-DCT, and H-QCT cores, respectively, compared to the unprotected panel, which indicates that a large portion of the blast energy was mitigated. Furthermore, the damage pattern for the shielded panels improved from severe damage and spalling to just minor cracks on the back face of the RC panel. A parametric study was performed to investigate the effect of skin plate thickness on the blast performance of the cladding structure. Slab deflection has decreased as the front skin plate thickness and stiffness increased. However, it had a negative impact on the deformation of the core layer and its energy dissipation. A larger portion of energy was dissipated by the skin plate as the thickness of the skin plate increased, so the core layer did not engage with its full capacity. To conclude, the novel proposed sacrificial structures have shown superior blast shielding for the RC structures.

4.8   References

1.   Halleux, F., et al. Resistance Analysis of Steel and Mixed Steel-Concrete Columns Subjected to Close-Contact Explosions. in Proceedings 16th DYMAT Technical meeting, Brussels. 2005.

2.   Lemanski, S., et al., Understanding the behaviour of fibre metal laminates subjected to localised blast loading. Composite Structures, 2006. 76(1-2): p. 82-87.

3.   Guruprasad, S. and A. Mukherjee, Layered sacrificial claddings under blast loading Part I—analytical studies. International Journal of Impact Engineering, 2000. 24(9): p. 957-973.

4.   Guruprasad, S. and A. Mukherjee, Layered sacrificial claddings under blast loading Part II—experimental studies. International Journal of Impact Engineering, 2000. 24(9): p. 975-984.

5.   Kotzialis, C., C. Derdas, and V. Kostopoulos, Blast Behavior of Plates with Sacrificial Cladding. Proceedings of GRACM 05, 2005: p. 199.

6.   Starr, C.M. and T. Krauthammer, Cladding-structure interaction under impact loads. Journal of Structural Engineering, 2005. 131(8): p. 1178-1185.

7.   Van Paepegem, W., et al., Blast performance of a sacrificial cladding with composite tubes for protection of civil engineering structures. Composites Part B: Engineering, 2014. 65: p. 131-146.

8.   Ousji, H., et al., Air-blast response of sacrificial cladding using low density foams: Experimental and analytical approach. International Journal of Mechanical Sciences, 2017. 128: p. 459-474.

9.   Alghamdi, A., Collapsible impact energy absorbers: an overview. Thin-walled structures, 2001. 39(2): p. 189-213.

10. Hanssen, A., L. Enstock, and M. Langseth, Close-range blast loading of aluminium foam panels. International Journal of Impact Engineering, 2002. 27(6): p. 593-618.

11. Mazek, S.A. and A.A. Mostafa, Impact of composite materials on performance of reinforced concrete panels. Computers and Concrete, 2014. 14(6): p. 767-783.

12. Codina, R., D. Ambrosini, and F. de Borbón, New sacrificial cladding system for the reduction of blast damage in reinforced concrete structures. International Journal of Protective Structures, 2017. 8(2): p. 221-236.

13. Al-Rifaie, H., et al., A New Blast Absorbing Sandwich Panel with Unconnected Corrugated Layers—Numerical Study. Energies, 2021. 14(1): p. 214.

14. Wang, W., et al., Experimental study on scaling the explosion resistance of a one-way square reinforced concrete slab under a close-in blast loading. International Journal of Impact Engineering, 2012. 49: p. 158-164.

15. Abada, M. and A. Ibrahim, Metallic Ribbon-Core Sandwich Panels Subjected to Air Blast Loading. Applied Sciences, 2020. 10(13): p. 4500.

16. Riedel, W., 10 years RHT: a review of concrete modelling and hydrocode applications. Predictive modeling of dynamic processes, 2009: p. 143-165.

17. Autodyn, A., Theory manual revision 4.3. Century Dynamics, Concord, CA, 2005.

18. Johnson, G.R. and W.H. Cook. A constitutive model and data for metals subjected to large strains, high strain rates, and high temperatures. in Proceedings of the 7th International Symposium on Ballistics. 1983. The Netherlands.

19. Zukas, J., Introduction to hydrocodes. 2004: Elsevier.

20. Dobratz, B.M., Properties of chemical explosives and explosive simulants. 1972, comp. and ed.; California Univ., Livermore (USA). Lawrence Livermore Lab.

21. Abada, M. and A. Ibrahim, Hybrid multi-cell thin-walled tubes for energy absorption applications: Blast shielding and crashworthiness. Composites Part B: Engineering, 2020. 183: p. 107720.

Chapter 5: Metallic Ribbon-Core Sandwich Panels Subjected to Air Blast Loading

5.1   Introduction

This chapter numerically investigates the performance of the sandwich structures under the impact of air blast loading. The hydro-code program (Autodyn) supported by the finite element program (ANSYS) is adopted to study the response of the structure under the impact of blast load. The accuracy of the FE models was verified using experimental results available in the literature. The results show that the finite element model can be reliably exploited to simulate the dynamic behavior of the sandwich structure with the new proposed core topologies under the impact of blast load.

Sandwich structures are widely used in blast dissipation applications due to their excellent physical and mechanical properties [1–5]. They are adopted as sacrificial cladding structures, which are designed to attach at the façade of structures in order to absorb energy through the progressive plastic deformation of the front-facing plate and the inner core layer minimizing the transfer of the peak force to the non-sacrificial structure [6–8]. Sandwich panels are three-layer composite structures consist of two outer plates made of metals or composite materials and a crushable core layer in between. The plate faces blast wave distributes blast pressure more evenly across the core layer that deforms progressively and absorbs most of the energy.

The core layer could have several topologies, such as corrugated [5,9], honeycomb [5,10], trusses [11,12], hybrid cores [13], and functionally graded cores (FGC) [14]. Under those topologies, several configurations could be used to shape the core of the sandwich panels to provide adequate stiffness and strength to support structural loads. For instance, the corrugated topology can have trapezoidal-folded, diamond-folded, Y-frame-folded, and triangular-folded core configurations [7], a zig-zag trapezoidal corrugated core [15], and woven corrugated cores [16].

Research work has been dedicated to examining the impact of assorted core topologies on the blast performance of sandwich structures. Wei et al. [17] examined the response of metallic triangular honeycomb sandwich panels and equivalent solid plates under localized blast loads. They noticed that the sandwich panels were superior to a solid plate when subjected to blast load. Moreover, they proposed a sandwich panel with a double-corrugated softcore, which surpasses the performance of a triangular honeycomb core. As an attempt to investigate the effect of the core topology; Dharmasena et al. [18] examined

the behavior of metallic sandwich panels with diverse core topologies; square honeycomb, triangular honeycomb, multi-layer pyramidal truss, triangular corrugation, and diamond corrugation core topologies with a core relative density of approximately 5%. They found that truss and corrugated cores had a significantly lower strength with a long plateau, like metal foams, while honeycomb cores revealed a high initial strength with a softening post-peak response. Moreover, they found that crushable cores reduce the transmitted impulse by 25% compared with high rigid cores.

Liang et al. [19] investigated three core topologies (square honeycomb, I-core, and corrugated) for a sandwich structure subjected to a blast load. They concluded that the best overall performance was attained by the soft cores (corrugated). Alberdi et al. [7] numerically investigated the performance of six different core topologies for metallic sandwich panels under blast loading. They concluded that folded shapes attenuate more energy than honeycomb shapes.

Ahmed et al. [20] conducted a comprehensive numerical analysis on the response of metallic sandwich structures with different core configurations under the impact of blast load. They also introduced woven shapes as a novel core topology for the metallic sandwich structures. The study revealed that woven shapes achieved superior energy dissipation capability compared to the folded and honeycomb shapes; however, this novel pattern required more core relative density compared to corrugated cores.

Various researchers focused on the far-field blast; however, close-in explosions often cause a severe damage to various structural components. The American Society of Civil Engineers (ASCE) classifies explosions with a scaled distance (Z) of less than 1.2 m/kg1/3 as a close-in explosion [21]. The scaled distance is defined as $Z = R/W^{1/3}$, where R is the range (distance between the explosive and the target) and W is the charge weight equivalent to a TNT explosive [21]. As opposed to far-field explosions, blast waves released from close-in explosions can produce both localized and global failure for the structural elements. The localized failure takes place in the form of localized punching and spalling, while global failure usually occurs as a flexural failure.

The field blast tests are a reliable experimental approach to investigate the dynamic behavior of blast-resistant structures. Blast tests conducted in the field face many challenges, such as test setup, high cost, people injury, environmental risks, and measurement accuracy. Alternatively, finite element analysis (FEA) using hydro-code programs allows researchers to observe the response and failure modes of structural components subjected to blast loading [22]. Numerical results obtained by the FEA are usually verified by the data obtained from

the field blast test. So reliable numerical models validated against measured field data is an effective tool to analyze structural performance under blast impact. In this study, the numerical model is validated using the experimental work done by Zhang et al. [23,24]. Once the numerical model has been validated, detailed numerical models were conducted to investigate the behavior of the proposed core topology.

This chapter proposes a new ribbon core topology for sandwich structures. This configuration aims to provide a sandwich structure with many advantages, such as being very lightweight, the least expensive, simplicity in manufacturing, great flexibility, and curvature that can be built in two directions. The ribbon configuration consists of folded strips placed in two perpendicular directions forming the ribbon pattern as illustrated in Fig. 5.1. This technique exploits the material for better stress distribution, enhancing the ribbon cores' capability against blast loads. Various blast mitigation parameters such as front and backplate deflection and energy absorption were assessed to highlight the outstanding behavior of the ribbon configuration compared with ordinary corrugated cores. A parametric study has been conducted considering design parameters such as the front plate's thickness, back plate's thickness, the core layer's thickness, the height of the core layer, and the angle of corrugation to investigate their influence on its blast performance
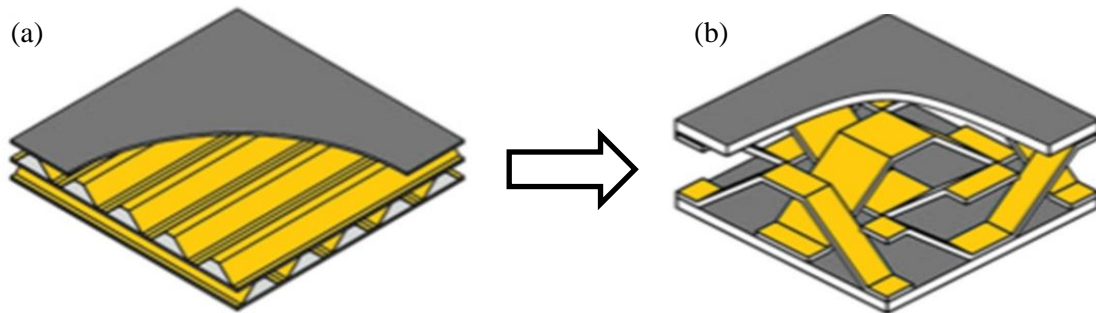

Fig. 5.1: a) conventional corrugated core sandwich panel, b) ribbon core sandwich panel

5.2   Structure Configuration and Finite Element Model Validation

5.2.1   Geometric Description

Figure 1 shows a typical set-up for the field blast test just before detonation. Based on the field blast tests carried out by Zhang et al. [23,24], The target structures adopted for the current validation were trapezoidal (TZ) and triangular (T) corrugated sandwich panels. They consist of front and back plates and a corrugated folded shape core layer made of annealed 304 stainless steel alloy. The tested panels were clamped along the four edges, providing a 288×300 mm^2 exposure area to the shock wave, as shown in Figure 5.2. In the

present study, only the exposure area of the panel was modeled, as the outer region of the panels was used for clamping purposes, as depicted in Figure 5.2. The geometric parameters of the panels are demonstrated in Table 5.1. The blast wave was generated by the detonation of a 55 g cylindrical TNT charge located over the center of the panel with a given standoff distance (SoD). The *SoD* is the distance between the center of the explosive and the front face of the target. Three different *SoD*s of 50 mm, 100 mm, and 150 mm were adopted to validate the deformation and failure mechanisms of the sandwich panel under air blast loading. The *SoD*s of 100 and 150 mm generated localized plastic deformation. However, the blast intensity under the *SoD* of 50 mm was to simulate the fracture and failure of the panel.

Table 5.1. Parameters of the sandwich panels.

Panel	Explosive	Geometric Parameters							
	SoD (mm)	W (g)	t_f (mm)	h_c (mm)	t_c (mm)	t_b (mm)	B (mm)	φ (°)	$\bar{\rho}$ (%)
TZ-1	50	55	1.38	14	0.7	1.38	7	45	6.34
TZ-2	100	55	1.38	14	0.7	1.38	7	45	6.34
TZ-3	150	55	1.38	14	0.7	1.38	7	45	6.34
T-1	50	55	1.38	14	0.7	1.38	-	45	6.6
T-2	100	55	1.38	14	0.7	1.38	-	45	6.6
T-3	150	55	1.38	14	0.7	1.38	-	45	6.6

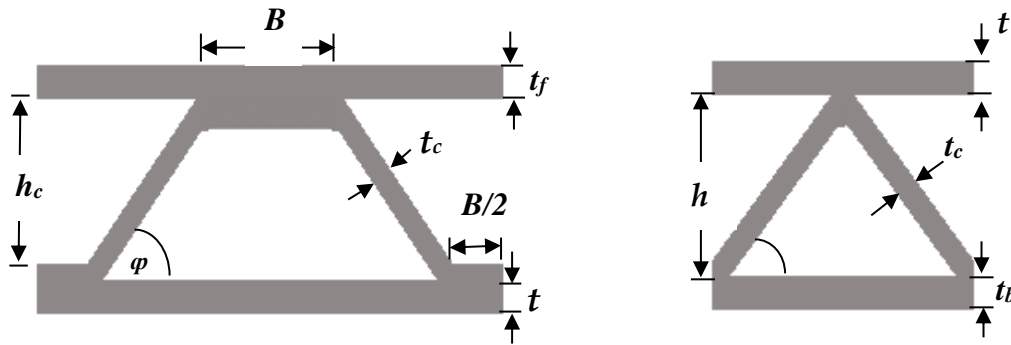*data from Zhang et al. [23,24].
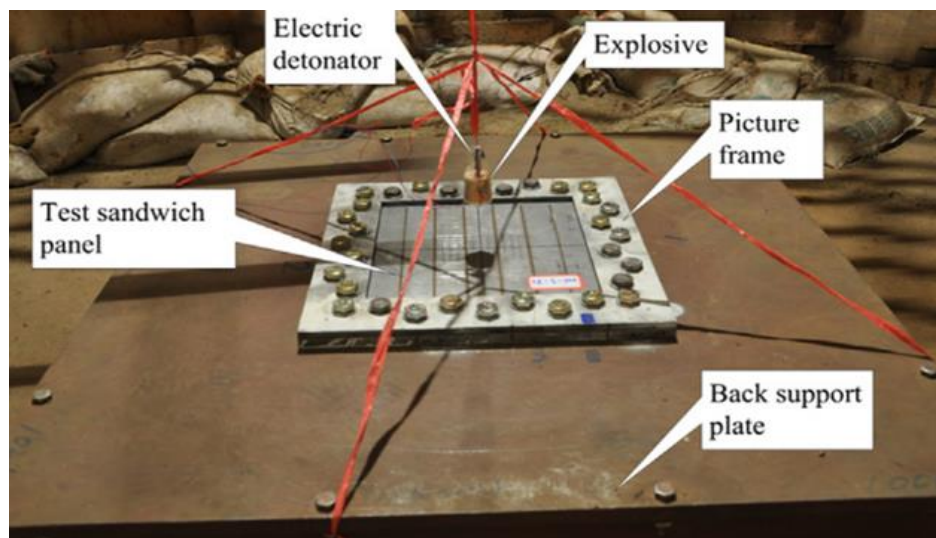
(a)

Figure 5.2. Schematics of (a) an experimental set-up, (b) trapezoidal (TZ)-panel cross-section unit cell, and (c) triangular (T)-panel cross-section unit cell. (Reproduced from refs. [23,24]).

5.2.2   FE Modeling

Numerical investigation works well in analyzing the dynamic response of structures, especially the deformation mechanisms and fluid-structure interaction (FSI). Numerical models were conducted, and their results were compared with the experimental results for validation purposes.

There is an interaction between the shock wave and the target structure (FSI) in blast loading. Hydrodynamic codes are capable of simulating this type of interaction. In this study, the numerical simulations were performed by using ANSYS/Autodyn V-19.0. R2 which is designed to solve non-linear dynamic problems such as impact, penetration, and blast events using Lagrangian, Eulerian, and Arbitrary Lagrange–Euler (ALE) solvers [22]. Generally, the Lagrange solver is used for modeling solid continua (structures) as the mesh moves with the material as it deforms, while the Eulerian solver is preferred to describe the gas flow from an explosion as it assumes that a grid is fixed in space through which material can flow. The FE model comprised the air block in which the explosion occurred. The target panel either with a Trapezoidal (TZ) or triangular (T) corrugated core suited between two facing sheets.

The computational time for the 3D model of blast simulations is very high. Two techniques were used in this study to reduce the computational time while maintaining accurate results. The first was using symmetry to model a quarter of structure. The second was adopting remapping to overcome the complete 3D structure's meshing problem as fine mesh in 3D model consume much time till the blast wave reaches the structure and starts to interact with it. This technique allows a 2D model with fine mesh to be mapped into a 3D model with a coarser mesh. The remapping is usually done through three steps. First, a 2D axisymmetric model is created to simulate the detonation of the explosive charge, as depicted

in Figure 5. 3(a). The 2D model is run until the shock vector just arrives before striking the front face of the target. Next, a remap file is created and then imported to fill the 3D Eulerian domain (air block) as an initial condition, as shown in Figure 5.3(d). Finally, the 3D model is executed to solve from that point.
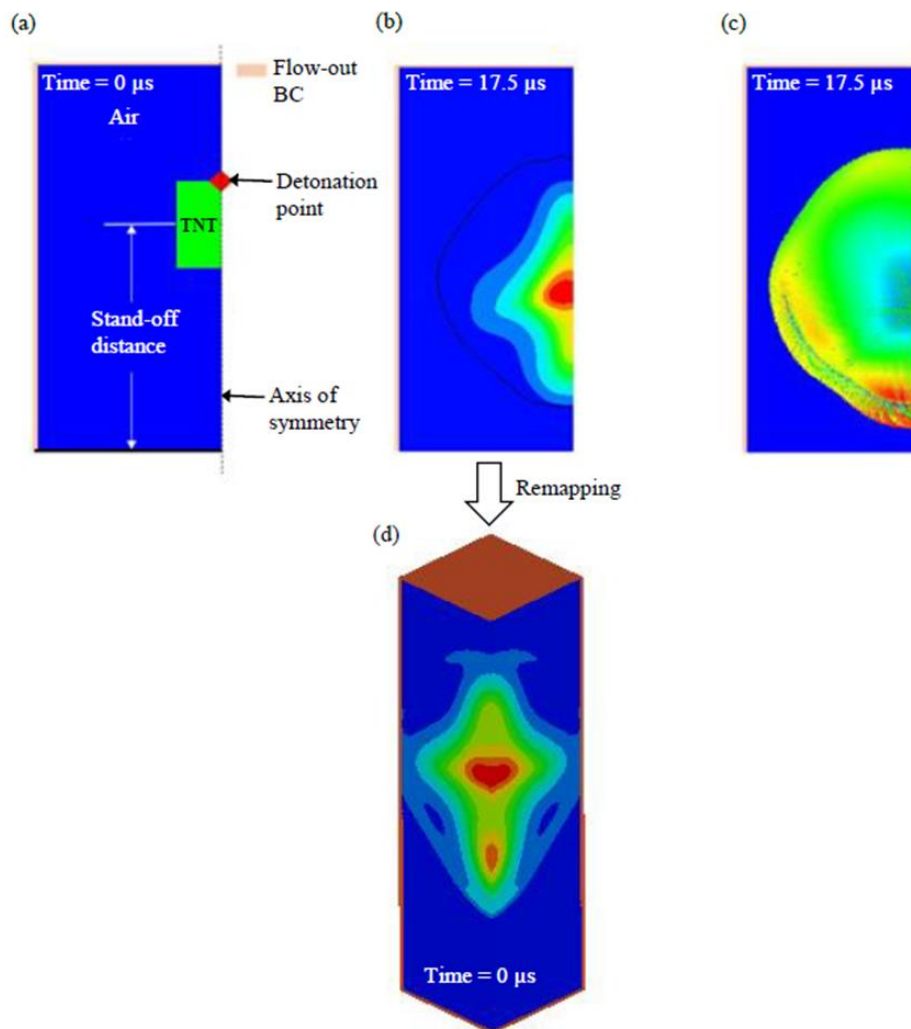

Figure 5.3: Remapping blast pressure from a 2D model to a 3D model. (a) The 2D model before detonation. (b) The pressure contour of the 2D model before striking the target. (c) The pressure vectors of the 2D model before remapping. (d) The pressure contour of the 3D model after remapping just before hitting the structure.

The air block was only generated over the center part of the panel due to the localization of the blast wave [25]. A typical air block with 70 mm × 70 mm × 250 mm was created by the Euler solver. The boundary conditions were selected to flow out at the four faces of the air block. Thus, any pressure flowing over the structure during the blast will flow out from

the boundary of the air block. A flow-out boundary was used to reduce the reflection of stress waves from the numerical boundaries back to the structure which might be considered an internal detonation problem. Belytschko-Tsay shell elements modeled the sandwich structure. After executing mesh sensitivity, the following element sizes were selected, 0.1 mm for 2D models, 1 mm for 3D models, and 1 mm for the shell elements. The Lagrange solver was used to model the shell elements of the structure. A fixed boundary condition was applied to the outer edges of the panel as illustrated in Figure 5.4. Euler elements (air) were assumed to be intersected by the Lagrange interface (structure). To deal with this interaction, a fully coupling algorithm was used to connect the Lagrange solver and Eulerian solver with a cover fraction limit of 0.5 [26]. The contact between the sandwich structural elements (face sheets and core) was considered in simulations and defined by CONTACT_AUTOMATIC_SURFACE_TO SURFACE. The contact algorithm was formulated using the penalty method, and the contact state was taken to be frictionless. Moreover, gauges were applied to the facing plates to track their response (same locations for the experimental measuring). The CPU times for the 2D simulations used to create the remapping files to fill the 3D domain for three different stand-off distances (50, 100, and 150 mm) are 5, 10 and 13 min, respectively. Most of the 3D simulations in the present study ran CPU time between 20 and 22 hrs.
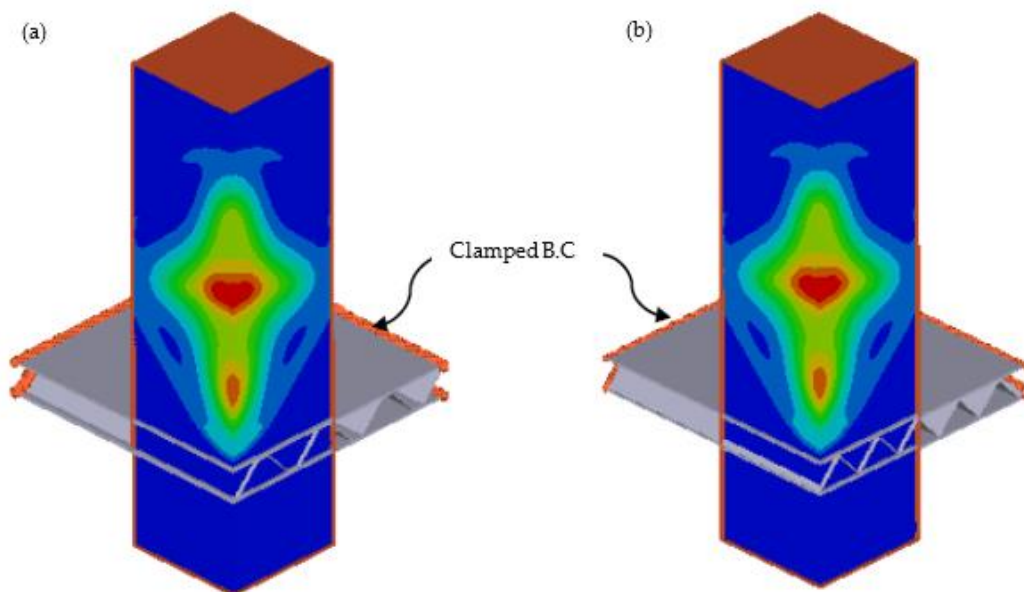

Figure 5.4: Three-dimensional FE models for the sandwich structures. (a) TZ-panel. (b) T-panel.

5.2.3   Material Models

5.2.3.1 Air and TNT

To model, the TNT explosion in Ansys Autodyn, the surrounding air, and the product of the TNT explosion were assumed to behave as an ideal gas. An ideal gas equation of state (EOS) was used to describe air and was expressed by:

$$P = (\gamma - 1)\rho_g e_0 \tag{1}$$

where P is the pressure, γ is the ideal gas constant and equals 1.4 for air, ρ_g is the air density, and e_0 is the specific internal energy. The internal energy of air was used as 2.068×10^5 kJ/kg. This internal energy initialized the air medium to an atmospheric pressure of 101.3 kPa. Table 5.2 includes the material properties adopted for air [22].

Table 5.2. Ansys/Autodyn material model for the air.

EOS	γ	Reference density (g/cm^3)	Reference energy $(\mu\text{J/mg})$
Ideal gas	1.4	1.225×10^{-3}	2.068×10^5

The Jones‑Wilkins‑Lee (JWL) equation of state was used to describe the explosive material [27], which is in the form of:

$$P = A\left(1 - \frac{\omega}{R_1 V}\right)e^{-R_1 V} + B\left(1 - \frac{\omega}{R_2 V}\right)e^{-R_2 V} + \frac{\omega E}{V} \tag{2}$$

where *A, B, R₁, R₂, and ω* are empirically derived constants that depend on the type of explosives, *V* is the volume of charge, and *E* is the detonation energy per initial unit volume [28]. The material properties used for TNT were tabulated in Table. 3. [28].

Table 5.3. The JWL model used to define the TNT material model in Ansys/Autodyn.

ρ (g/cm^3)	A (GPa)	B (GPa)	R_1	R_2	ω
1.63	373.75	3.747	4.15	0.90	0.35

5.2.3.2 Annealed 304 Stainless Steel

The Johnson-Cook (J–C) material model was elected to describe the flow stress of the annealed 304 stainless steel. This model is ideal for a material subjected to large strains, high strain rates, and high temperatures. The flow stress model is expressed by Equation 5.3 [29].

$$\sigma_y = [A + B(\varepsilon_p^{eq})^n][1 + c\ln(\frac{\dot{\varepsilon}_p^{eq}}{\dot{\varepsilon}_0})][1 - (T^*)^m] \tag{5.3}$$

where σ_y is the dynamic flow stress, ε_p^{eq} is the equivalent plastic strain, $\dot{\varepsilon}_p^{eq}$ is the equivalent plastic strain rate, and m is the thermal softening exponent. The constants A, B, n, c, $\dot{\varepsilon}_0$, and m are material parameters and can be determined from an empirical fit of flow stress data. T^* is the homologous temperature and it could be calculated from Equation 5.4.

$$T^* = \frac{T - T_r}{T_m - T_r} \tag{5.4}$$

T is the material temperature, T_m is the melting temperature of the material, and T_r is the room temperature. In order to capture the rupture, the failure criterion based on equivalent plastic strain was adopted. This criterion has gained popularity due to its simple and effective formulation and has been proven to provide results with satisfying accuracy [24]. Table 4 shows the *J-C* material model parameters for the 304 stainless steel material. A fixed boundary condition was applied to the outer edges of the panel. Also, gauges were applied to the facing plates to track their response.

Table 5.4. Constitutive model of 304 stainless steel adopted in Ansys/Autodyn.

Parameter	Unit	Value
Reference density	g/cm^3	7.85
EOS	-	Linear
Bulk modulus	kPa	1.67×10^8
Strength	-	Johnson Cook
Shear modulus	kPa	6.69×10^7
Yield stress, A	kPa	3.10×10^5
Hardening constant, B	kPa	1.00×10^5
Hardening, exponent, n	-	0.65
Strain rate constant, c	-	0.07
Ref. strain rate, $\dot{\varepsilon}_0$	s^{-1}	1.00
Thermal softening exponent, m	-	1.00
Indoor temperature, T_m	K	292
Melting temperature, T_r	K	1672
Failure	-	Plastic strain
Plastic strain	-	0.42

5.2.4   Results and Discussion

Generally, permanent deformation/failure of the faceplates is considered the most important attribute of the structural response, as all other parameters (impulse transfer and energy dissipation) rely on it. From the field blast test, it can be observed that the face sheets were plastically deformed for the 150-mm and 100-mm *SoD*, and no failure has occurred. However, for the 50 mm *SoD*, the panel was damaged. Experimental and numerical central deflections of the corrugated core sandwich panels were compared and summarized in Table 5.5. Figure 5.5 shows the comparison of the deformation/failure modes of the experimental and numerical models. The comparison was focused on the permanent deflection between simulation and experiments. results of the numerical model were highly accurate since the standard deviation of results varied between 1.83% and 11.93%, as shown in Table 5.5. At this point, the proposed models can be used reliably to investigate the performance of the ribbon topology as new core configuration for sandwich structures subjected to air blast loading.
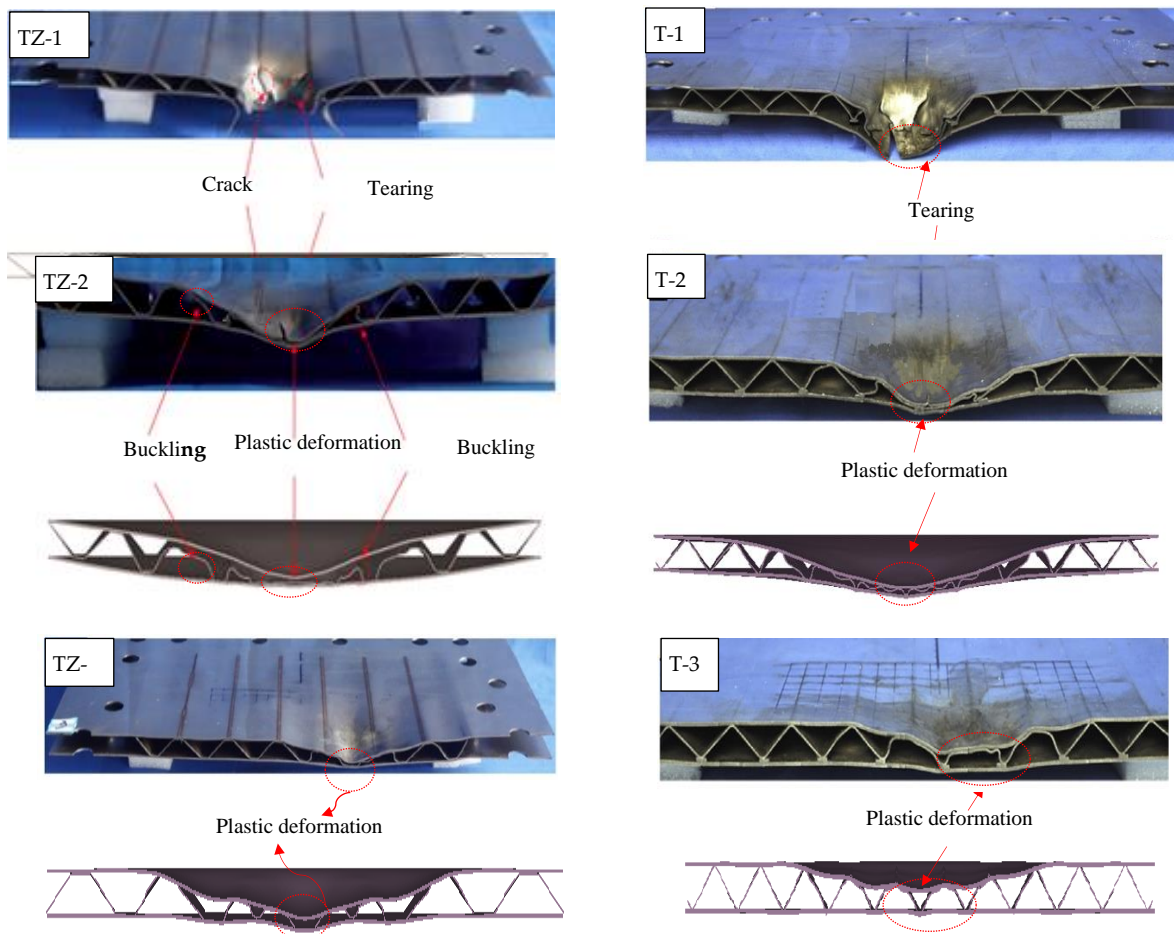
Figure 5.5: Comparison between the experimental and numerical results of deformation/failure modes due to detonation at stand-off distances (*SoD*s) of 50, 100, and 150 mm. (a) TZ-panel. (b) T-panel.

Table 5.5. Experimental and numerical results.

Panel	Front-Plate Deflection δ_f (mm)		Discrepancy (%)	Back Plate Deflection δ_b (mm)		Discrepancy (%)
	Experimental*	Numerical		Experimental*	Numerical	
TZ-1	Failure	Failure	-	Failure	Failure	-
TZ-2	28.89	29.42	1.83	14.14	14.64	3.54
TZ-3	18.99	20.55	8.21	7.69	8.21	6.76
T-1	Failure	Failure	-	Failure	Failure	-
T-2	22.71	24.70	8.76	10.31	11.54	11.93
T-3	12.91	14.11	9.31	5.18	5.63	8.69

*Data from Zhang et al. [23,24].

5.3   Proposed Sandwich Panels

Corrugated cores are stiff and strong in the longitudinal direction but weak in the transverse direction [30]. The simplest approach to overcome this is by placing corrugated cores aligned with the panel's longitudinal and transverse directions. The new configuration consists of corrugated strips placed in two perpendicular directions, forming the ribbon core (RC) depicted in Figure 5.5. Two different geometries for RC were used in this study, the trapezoidal ribbon core (TZRC) and the triangular ribbon core (TRC). They were designed with the geometric parameters for the TZ and T cores in order to capture the impact of the new technique on the blast performance of sandwich structures. The width of each strip (*b*) was 7 mm, the height (*h*) was 14 mm, and the thickness (*t_c*) was 0.7 mm. The relative density ($\bar{\rho}$) for the TZRC and TRC were 2.28 and 2.84, respectively. The novel topologies use less material compared with the traditional corrugated cores by about 64% for the TZRC and 56.9% for TRC. The panel had the same dimensions used for the TZ and T panels.

The RC structures were exposed to a detonation of 55 g of TNT explosive charge located over the center of the panel with 100 mm SoD. Autodyn was used to numerically investigate the dynamic response of the RC panels under the impact of the blast load.
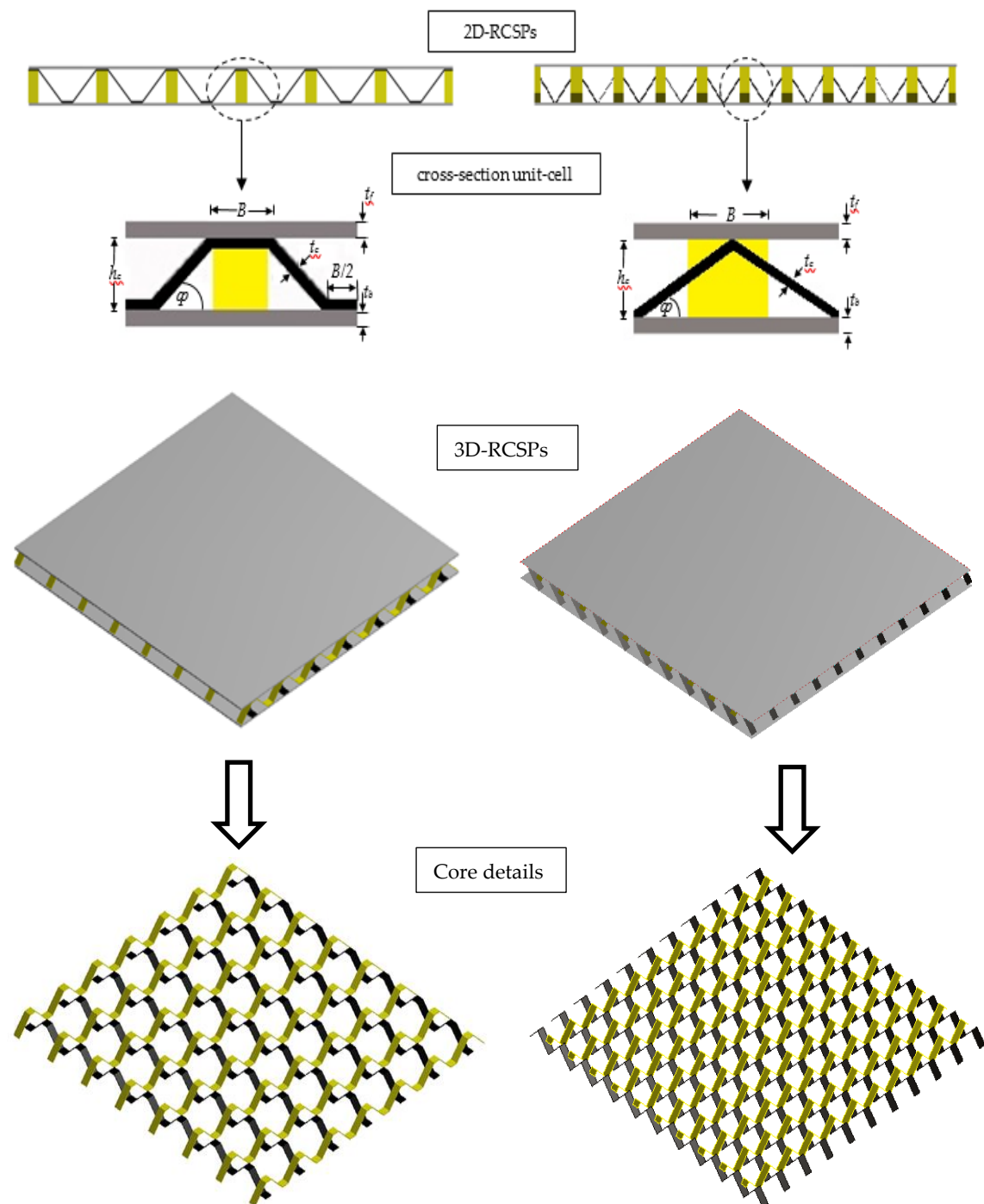
Figure 5.6: Schematic and inner core configuration of the ribbon core sandwich structures. (a) Trapezoidal corrugated ribbon core (TZRC)-panel. (b) Triangular ribbon corrugated core (TRC)-panel.

Previous studies [14] revealed that the behavior of the sandwich structure subjected to blast loads could be split into three stages, namely the fluid-structure interaction stage, core compression stage, and structural dynamic response stage. Figure 5.6 shows a series of

deformation processes of TZRC and TRC panels subjected to the detonation of 55 g TNT with a stand-off distance of 100 mm. Figures. 5.7 and 5.8(a) show the panel at time t = 0 after remapping the final state of the 2D model to a 3D model just before the impulse is imparted to the front-face sheet of the sandwich panel. Then, at t = 0.001 msec, the shock wave firstly strikes the center of the front-face sheet. From this moment on, the front face was starting to interact with the explosive product. During the fluid-structure interaction stage, the front face reached an initial velocity when the shock wave impinged on it, while the core and back face kept still. A dent deformation was first formed in the central area of the front face, Figures 5. 7 and 5.8(b). Then, the high compression velocity generated by the front face induced a shock wave into the core, and the core compressed gradually at t = 0.03 msec. It could be seen that the compression of the core decreased from the center to the peripheral region, as displayed in Figures 5.7 and 5.8(c). During this stage, the front face was decelerated by the core while the core and the back face were accelerated. At the end of the core compression stage, the panel components reached the same velocity and went into a phase of structural dynamic response under their own inertia. The dent deformation extended outwards and downwards with the transfer of momentum, Figures 5.7 and 5.8 (d). Then, the panel went into an oscillation until the kinetic energy was gradually dissipated by plastic bending and stretching. Finally, at t = 10 msec, the panel underwent residual deformation as shown in Figures 5.7 and 5.8 (e).
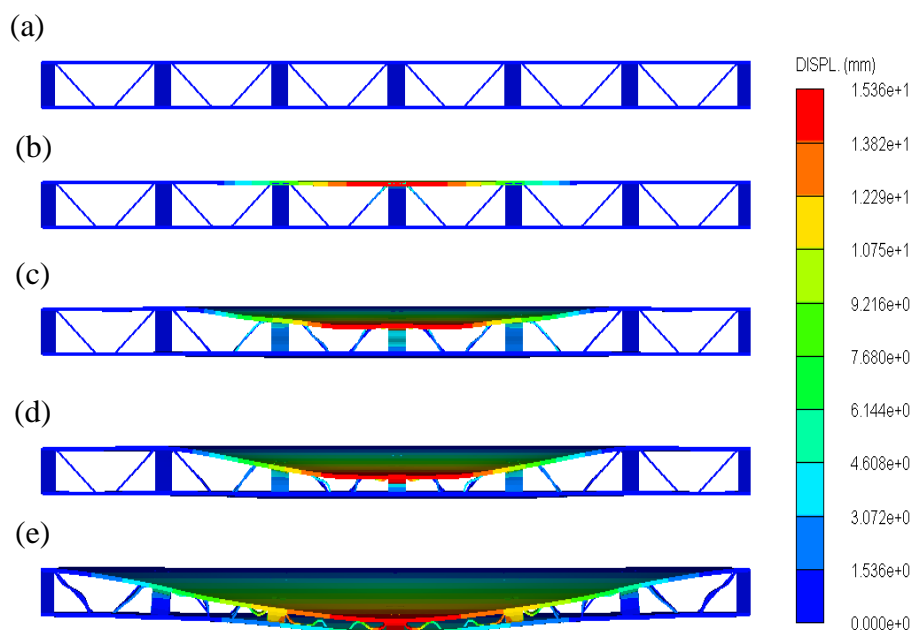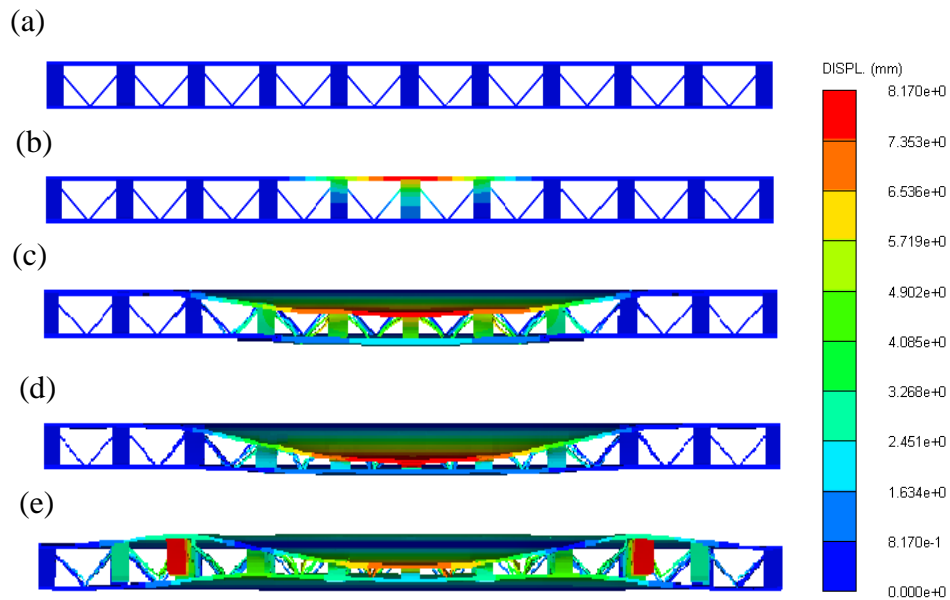

Figure 5.7: Dynamic response of the TZRC.

Figure 5.8: Dynamic response of the TRC.

Figure 8 illustrates the midpoint velocity and deformation/time histories of face sheets. As exhibited in Figure 5.9(a), the velocity at the midpoint of the front-face sheet quickly reaches its maximum value at the beginning of the response and then gradually decreases due to core compression. The midpoint velocity of the rear-face sheet started to increase by 0.03 msec after the front-face sheet deformed, and at 0.16 msec, the midpoint velocity of the rear face sheet caught up with that of the front-face sheet. Figure 5.9(b) shows the displacement–time history of the face sheets. It can be noticed that the compression remains unchanged when the face sheets reached the same deformation velocity. Finally, the panel entered an oscillating state to disperse the residual energy.
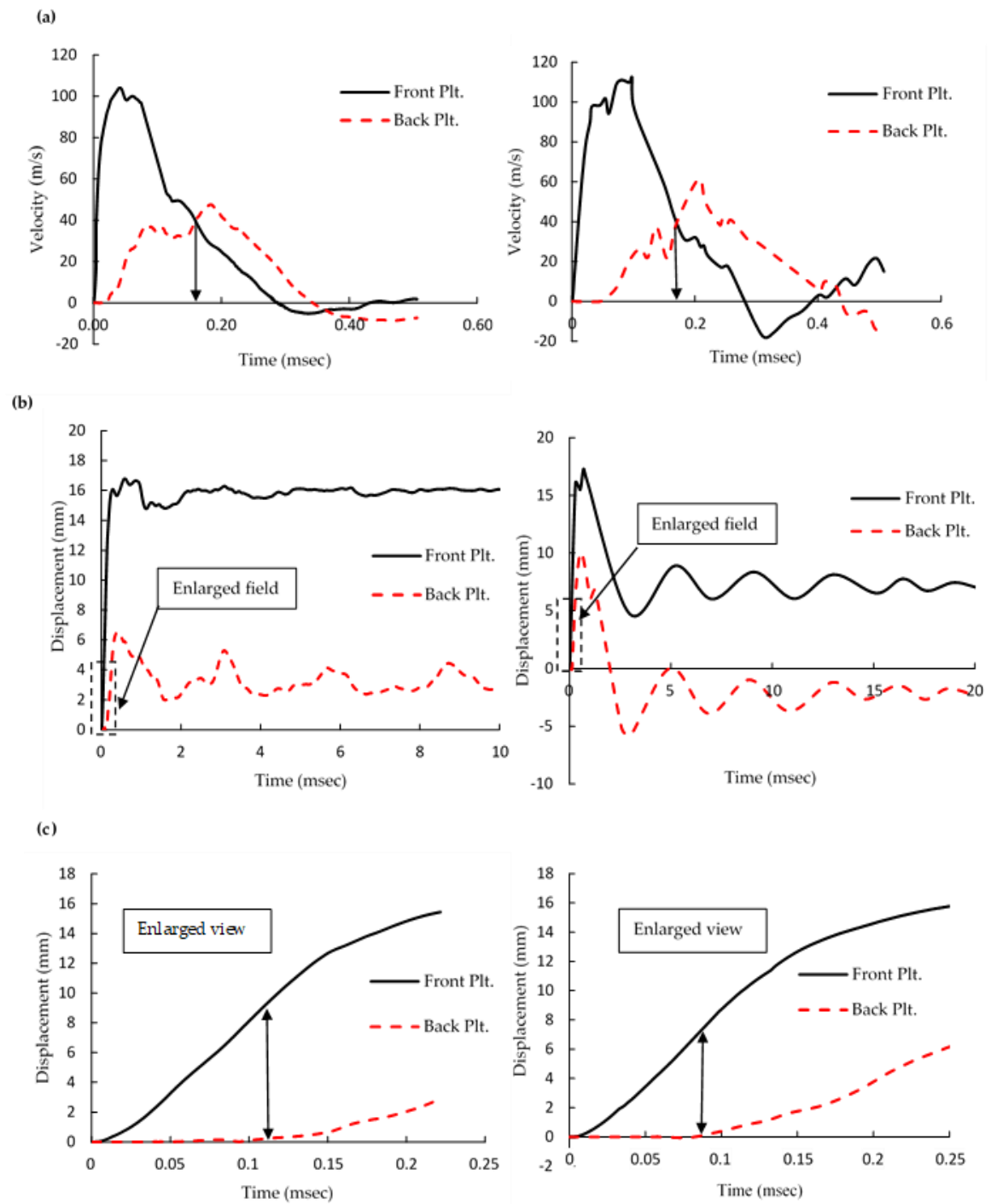
Figure 5.9: (a) Velocity and (b) displacement–time histories for the facing sheets at midspan. (c) Enlarged view for displacement–time histories within (0–0.25 msec) time interval, TZRC (left column), and TRC (right column).

The face sheet deformations were used as a blast performance parameter to compare between the ribbon and traditional corrugated core sandwich structures as shown in Figure 5.10. The results indicate that applying the ribbon core topology to the TZ-corrugated core reduced the facing plates' deformations by 45.3% for the front-plate deflection and 76.5%

for the back-plate deflection, while for the T-corrugated core, the plate defections decreased by 69.3% for the front plate and 112.1% for the backplate. The response of the Ribbon-Core Sandwich Panel (RCSP) is in accord with the "strong core" regime defined by Liang et al. [19], which means that the ribbon cores are more efficient than ordinary corrugated cores for sandwich structures subjected to blast load. Ribbon core sandwich structures can suffer a larger impulse as they absorb more energy and have less deformations than the conventional cores.
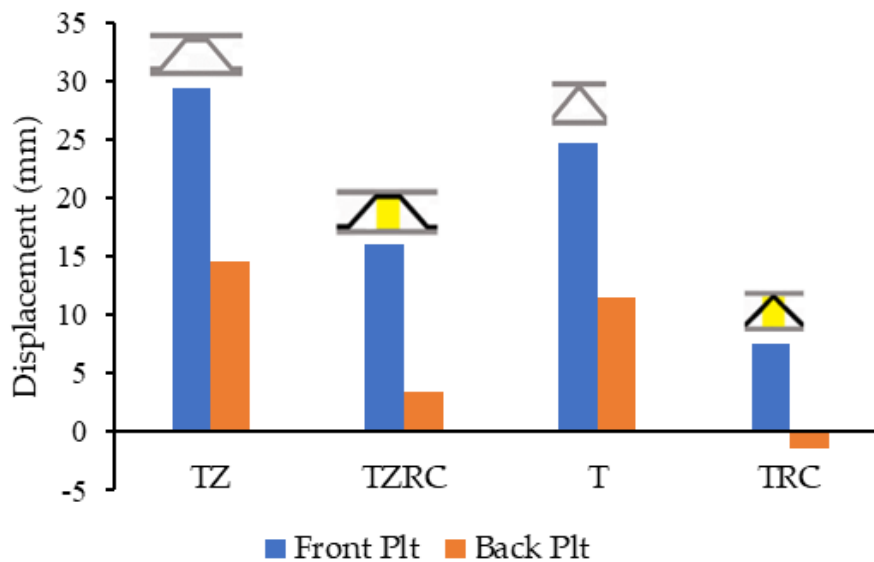
Figure 5.10: Residual midspan deflections for the facing sheets of sandwich structures with different core configurations under the impact of detonation of 55 g TNT at SoD 100 mm.

5.4   Parametric Study

5.4.1   Influence of Varying Face Sheets Thickness on RCSPs' Face Sheets Deformations

A parametric study was performed to investigate the effect of face sheets thickness variation on the front- and back-plate deflections of RCSPs. The TZRC sandwich structure was selected for this study. The parametric study aims to enhance the blast resistance of RCSP when the equivalent density increases. The investigation of the influence of face sheet thickness variation performed by two scenarios. The first one is the influence of varying the front-plate thickness on the performance of the RCSP, a constant rear-plate thickness with six different front-plate thicknesses: 0.6, 1, 1.4, 1.8, 2.2- and 2.6-mm.

Figure 5.11 shows the effect of changing the front-plate thickness on the front and rear plates' deflections. Figure 5.11, it can be seen that the front-layer deflection decreases as the front sheet thickness increases while the back-layer deflection decreases. The results

indicate that when using a front sheet with 2.6 mm thickness, the deflection decreases by an average of 75% for the front-face sheet and by an average of 70% for the rear-face sheet. It can be concluded that the rear-plate deflection decreases with increasing front-plate thickness due to the increased stiffness. In the second scenario, the effect of altering the thickness of the rear face sheet on the behavior of the RCSP is investigated by maintaining a constant front-face sheet thickness with six different rear-plate thicknesses: 0.6, 1, 1.4, 1.8, 2.2, and 2.6-mm. From Figure 5.11, it can be seen that changing the rear faceplate thickness has a negligible effect on the front-layer deflection; however, the rear face sheet deflection decreases upon increasing the rear-layer thickness. Comparing the deflection when using a back layer with a 2.6-mm thickness with the deflection when using a back layer with a 0.6-mm thickness, the deflection decreases by an average of 90.6% for the rear face sheet and by an average of 19.36% for the front-face sheet. The core compression is the difference of transverse deflections between the front plate and the rear plate. It can be noticed that more core compression occurs as the rear plate thickness increases due to increasing the stiffness of the core backing.
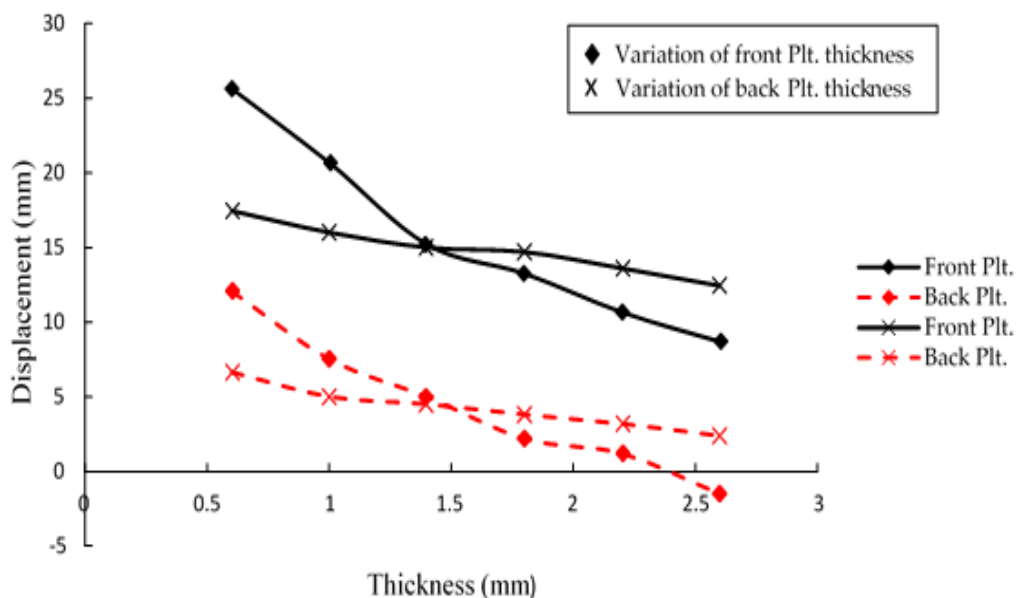

Figure 5.11: Central deformation with the face sheets thicknesses variation.

5.4.2   Influence of Face Sheets Thickness on Energy Dissipation

During the interaction between the explosion product and the structure, the energy of the explosion is transferred to the sandwich panel and then dissipated through the panel deformation. The energy dissipated by each component is numerically obtained and indicated in a stack bar diagram in Figure 5.12. The energy dissipated by each component is essentially the difference between the total energy (ET) and initial energy (EI) of each component.

Figure 5.12(a) shows the energy dissipated by each component of the RCSP for the first scenario. The figure demonstrates the contribution of the front plate, the inner core, and the rear plate in the energy dissipated by the RCSPs. When using a front sheet with thickness of 0.6 mm, the results imply that the energy dissipated attain the highest value and then reduced till reaching the minimum when the front plate thickness is 2.6 mm. It can be concluded that with increasing the front-plate thickness, the energy dissipation decreases.

Figure 5.12(b) illustrates the energy dissipated by the RCSP components for the second scenario. The results indicate that the rear plate has a negligible influence on the energy dissipated by the sandwich structure as the rear plate participates with a small portion in the energy dissipation of the structure relative to the other components (the front-face sheet and the inner core). The inner core layer dissipates a major portion of the energy. Increasing the rear plate thickness boosts the core layer's energy dissipation; however, it does not enhance the total energy dissipated by the sandwich structure. The highest level of energy dissipation was achieved when the front-plate thickness was 0.6 mm. Therefore, the sandwich panel with a thinner front-face sheet can improve the energy-absorbing capabilities of the structure. However, under large blast loading, tearing damage may develop on the thinner front face.
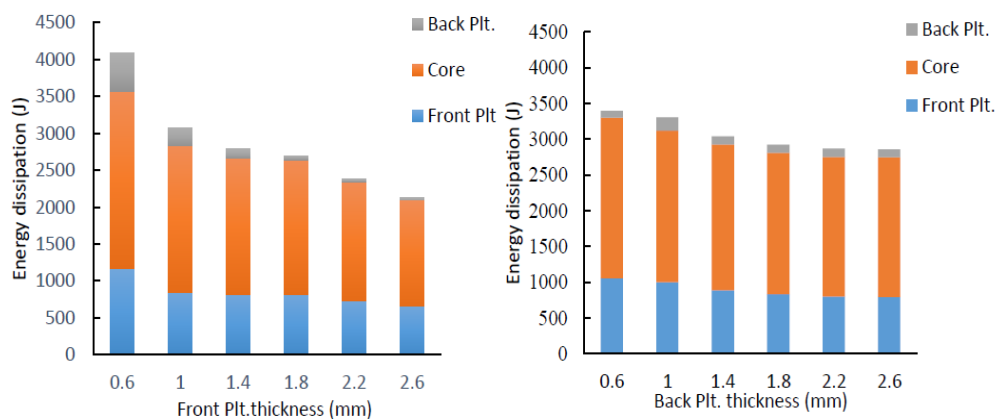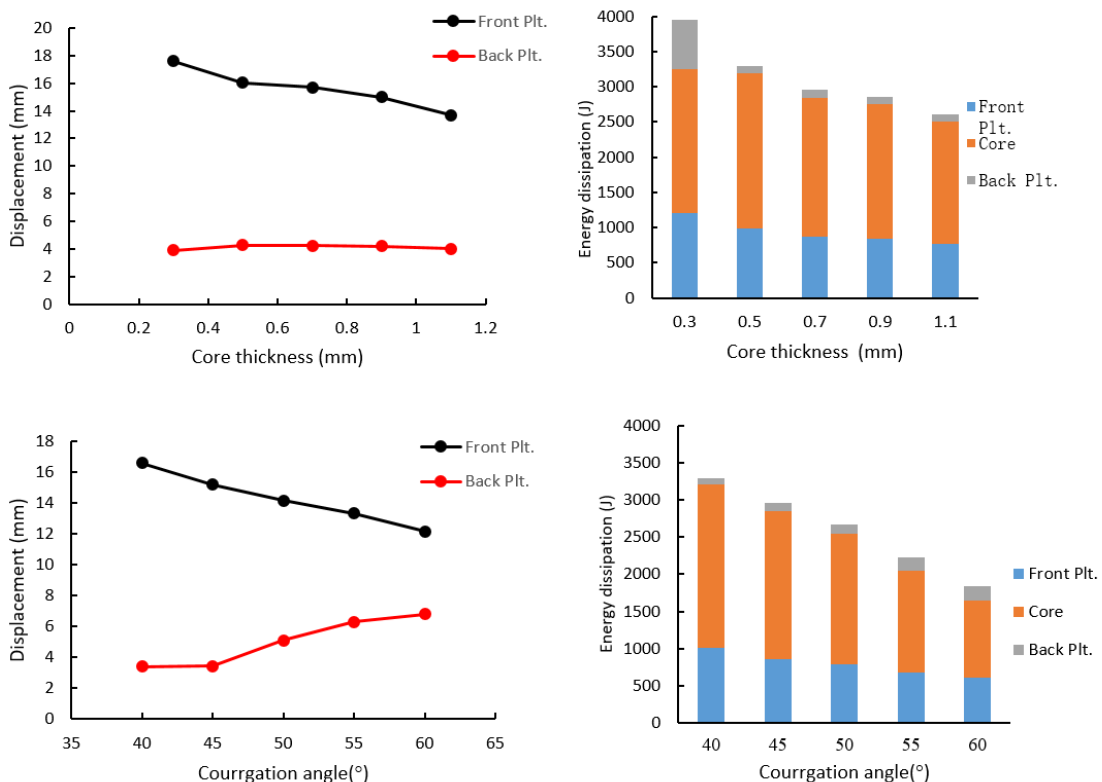
Figure 5.12: energy dissipation for Ribbon-Core Sandwich Panel (RCSP) components with a variation of (a) front-plate thickness. (b) Back-plate thickness.

5.4.3   Variation of Core Parameters on the Blast Performance of the RCS

The geometric parameters covered in this study were core thickness t_c, the angle of corrugation ϕ (º), and core height h_c. The effect of the core thickness runs through varying the thickness of the corrugated ribbon core: 0.3, 0.5, 0.7, 0.9, and 1.1mm. Figure 5.13(a) illustrates the influence of the core thickness on both facing sheet deflections and energy dissipated by the structure component due to the blast loading. It can be observed that the front-layer deflection decreases upon increasing the core thickness; however, the back-layer deflection increased slightly.

Moreover, the energy dissipated by the RCS decreased, which means that a softer core dissipates more energy. Increasing the corrugation angle from 40º to 60º, decreased the deformation of the facing sheets deformations decreased by about 30% and the dissipated energy decreased by an average of 25%, as indicated in Figure 5.13 (b). The core height of the TZRC sandwich varied between 10, 12, 14, 16, and 18 mm as shown in Figure 5.13 (c). The deflections of the facing sheets of the sandwich structure increased by an average of 27% by increasing the core height by 40%.
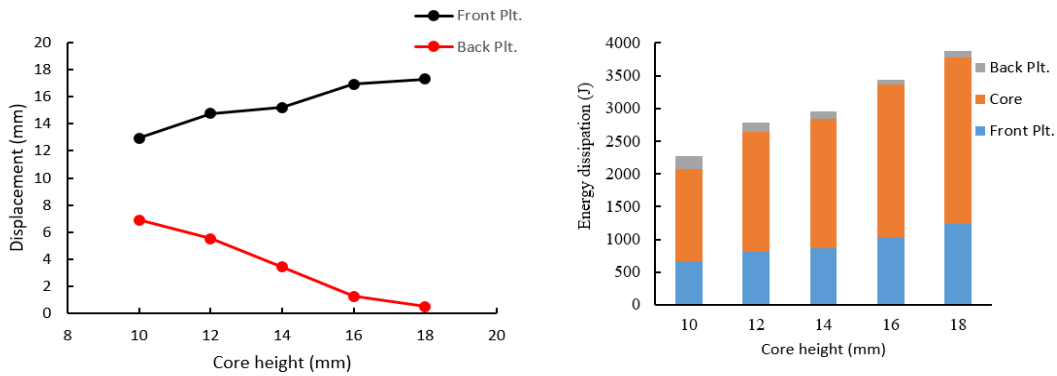
Figure 5.13: Facing sheets mid-span deflection and energy dissipation For RCSP components with variation in (a) core thickness, (b) the angle of corrugation and (c) core height.

5.5   Conclusions

This paper presents a new core topology that can be applied as an inner core layer for metallic or composite sandwich structures. This study investigated the effectiveness of two different core sandwich structure topologies (folded and ribbon) for blast load attenuation. The dynamic behavior of the novel RCSP was investigated under air blast loading by employing a nonlinear explicit finite element simulation. The numerical model has been validated using the experimental field blast test for trapezoidal- and triangular-corrugated core sandwich panels. A good agreement between simulations and experimental tests was achieved by the numerical models for predicting the deformation/failure patterns for the field-tested panels with a maximum deviation of 11.93% for the back-plate defection. ANSYS/Autodyn was utilized to investigate the performance of the proposed structure under the same experimental test conditions.

The blast performance of the investigated topologies was assessed in terms of the front-plate deflection, back-plate deflection, and energy dissipation. The results reveal that the ribbon core has a comparable blast resistance relative to the traditional corrugated core sandwich structures. The sandwich panel can suffer a larger impulse utilizing less material than the traditional corrugated cores by about 64% for the TZRC and 56.9% for TRC. A parametric study was conducted to investigate the effect of design parameters on the blast performance of the novel core configuration, and the following was observed:

- The back-plate deflection decreases with increasing front-plate thickness due to the increased stiffness. For instance, using a front sheet with 2.6 mm thickness, the deflection decreases by an average 70% for the rear face sheet.

- The back-plate thickness has a negligible effect on the front-layer deflection; however, the back-plate deflection decreases upon increasing the back-plate thickness.

- The sandwich panel with the thinner front-face plate could improve the energy-absorbing capabilities of the structure. However, under large blast loading, tearing damage may take place on the thinner front face.

- Increasing the core thickness has a negative impact on the blast behavior of the structure,

- Increasing the angle of corrugation more than 45° reduces the efficiency of the structure under the impact of blast loading.

To conclude, the newly proposed ribbon core panels have shown superior blast performance than the traditional folded cores. The parametric study provides guidelines for designing the ribbon core sandwich structures according to the required protection level.

5.6   References:

1.   Wiernicki, C.J., et al., Structural analysis methods for lightweight metallic corrugated core sandwich panels subjected to blast loads. Naval Engineers Journal, 1991. 103(3): p. 192-202.

2.   Gibson, L.J. and M.F. Ashby, Cellular solids: structure and properties. 1999: Cambridge university press.

3.   Lu, G. and T. Yu, Energy absorption of structures and materials. 2003: Elsevier.

4.   Jing, L., et al., The dynamic response of sandwich beams with open-cell metal foam cores. Composites Part B: Engineering, 2011. 42(1): p. 1-10.

5.   Zhang, P., et al., Dynamic response of circular metallic sandwich panels under projectile impact. Journal of Sandwich Structures & Materials, 2017. 19(5): p. 572-594.

6.   Palanivelu, S., et al., Close-range blast loading on empty recyclable metal beverage cans for use in sacrificial cladding structure. Engineering structures, 2011. 33(6): p. 1966-1987.

7.   Alberdi, R., J. Przywara, and K. Khandelwal, Performance evaluation of sandwich panel systems for blast mitigation. Engineering Structures, 2013. 56: p. 2119-2130.

8.   Abada, M. and A. Ibrahim, Hybrid multi-cell thin-walled tubes for energy absorption applications: Blast shielding and crashworthiness. Composites Part B: Engineering, 2020. 183: p. 107720.

9.   Li, X., et al., Response of aluminium corrugated sandwich panels under air blast loadings: experiment and numerical simulation. International Journal of Impact Engineering, 2014. 65: p. 79-88.

10.   Liu, J., Z. Wang, and D. Hui, Blast resistance and parametric study of sandwich structure consisting of honeycomb core filled with circular metallic tubes. Composites Part B: Engineering, 2018. 145: p. 261-269.

11.   Deshpande, V.S., N.A. Fleck, and M.F. Ashby, Effective properties of the octet-truss lattice material. Journal of the Mechanics and Physics of Solids, 2001. 49(8): p. 1747-1769.

12.   Liu, T., Z. Deng, and T. Lu, Design optimization of truss-cored sandwiches with homogenization. International Journal of Solids and Structures, 2006. 43(25-26): p. 7891-7918.

13. Cheng, Y., et al., Numerical investigation on the dynamic response of foam-filled corrugated core sandwich panels subjected to air blast loading. Journal of Sandwich Structures & Materials, 2019. 21(3): p. 838-864.

14. Jing, L. and L. Zhao, Blast resistance and energy absorption of sandwich panels with layered gradient metallic foam cores. Journal of Sandwich Structures & Materials, 2019. 21(2): p. 464-482.

15. Kooistra, G.W., V. Deshpande, and H.N. Wadley, Hierarchical corrugated core sandwich panel concepts. 2007.

16. Ahmed, S. and K. Galal, Effectiveness of FRP sandwich panels for blast resistance. Composite Structures, 2017. 163: p. 454-464.

17. Wei, Z., et al., The resistance of metallic plates to localized impulse. Journal of the Mechanics and Physics of Solids, 2008. 56(5): p. 2074-2091.

18. Dharmasena, K., et al., Dynamic compression of metallic sandwich structures during planar impulsive loading in water. European Journal of Mechanics-A/Solids, 2010. 29(1): p. 56-67.

19. Liang, Y., et al., The response of metallic sandwich panels to water blast. 2007.

20. Ahmed, S. and K. Galal, Response of Metallic Sandwich Panels to Blast Loads. Journal of Structural Engineering, 2019. 145(12): p. 04019145.

21. ASCE, Blast protection of buildings: ASCE/SEI 59-11. 2011.

22. AUTODYN, T., Theory Manual Revision 4.3, Concord, CA: Century Dynamics. 2003, Inc.

23. Zhang, P., et al., Dynamic response of metallic trapezoidal corrugated-core sandwich panels subjected to air blast loading–An experimental study. Materials & Design (1980-2015), 2015. 65: p. 221-230.

24. Zhang, P., et al., Experimental and numerical investigations on laser-welded corrugated-core sandwich panels subjected to air blast loading. Marine Structures, 2015. 40: p. 225-246.

25. Yuen, S.C.K., et al., Response of V-shape plates to localised blast load: Experiments and numerical simulation. International journal of impact engineering, 2012. 46: p. 97-109.

26. Autodyn, A., Theory manual revision 4.3. Century Dynamics, Concord, CA, 2005.

27. Zukas, J., Introduction to hydrocodes. 2004: Elsevier.

28. Dobratz, B.M., Properties of chemical explosives and explosive simulants. 1972, comp. and ed.; California Univ., Livermore (USA). Lawrence Livermore Lab.

29.   Lee, S., et al., Dynamic failure of metallic pyramidal truss core materials–experiments and modeling. International Journal of Plasticity, 2006. 22(11): p. 2118-2145.

30.   Xiong, J., et al., Sandwich Structures with Prismatic and Foam Cores: A Review. Advanced Engineering Materials, 2019. 21(1): p. 1800036.

Chapter 6: Conclusions and recommendations

Conclusions

Protecting structures against accidental or intentional blast events is a sophisticated task in structural engineering. Many efforts have been devoted to protecting structures from such devasting events. Several techniques have been proposed as effective methods for blast shielding. One of the best effective techniques is sacrificial layers compromising sandwich structures. This study mainly focuses on studying structures under blast impact and proposing new sacrificial layers for blast mitigation. The core layer in both sacrificial layers and sandwich structures is responsible for the significant portion of energy absorption. Consequently, the construction of core layers with more energy absorption capacity is an effective approach to setup an effective blast shield.

This research presents an innovative energy-absorbing component applicable to energy absorption applications. The developed structure comprises a superposition of two different energy absorption techniques to enhance the energy absorption capacity of a novel core structure. The proposed core structure can be applied to extensive blast-resistant and crashworthiness applications. Thus, experimental, and numerical investigations have been conducted to investigate the influence of applying internal stiffeners and staking composite layers on the behavior of aluminum (AL) thin-walled tubes. Single, double, and quadruple thin-walled metallic and hybrid tubes were tested under axial quasi-static compression test. The specimens were fabricated from unidirectional CFRP, epoxy resin, and aluminum alloy T6061-T6. Various crashworthiness parameters were assessed, such as the absorbed crash energy, specific energy absorption, crush force efficiency, average crushing load, and peak load absorbed, to highlight the effectiveness of the novel configurations. Also, in this study, a novel thin-walled core structure technique was developed and experimentally and numerically investigated.

The experimental test was simulated by using LSDYNA/Workbench software, and the material models were verified for investigating the dynamic behavior of global behavior of the sacrificial structures.

Incorporating these novel components have shown effective performance, with the following conclusions drawn:

- The energy absorption of the proposed techniques has been significantly improved, with the most effective configuration (Hybrid quadruple-cell) showed 131.70% more than the control single-cell AL tube.

- Numerical simulations showed very good agreement with the experimental results, which could be used as a confidential tool for the pre-manufacturing process.

- The novel sacrificial layers implied superior blast protection for the reinforced concrete panels under the impact of the close-in blast test. The Dynamic performance has been captured by utilizing a hydrodynamic code-named Autodyn based on a convergence study to choose the convenient mesh size. The cladding structures achieved the desired protection for the RC panels where the mid-span deflection significantly decreased by 62%, 78%, and 87% for H-SCT, H-DCT, and H-QCT cores, respectively, compared to the unprotected panel.

This study also introduced another effective novel core topology for composite and metallic sandwich structures named Ribbon Cores. These cores expressed a highly effective technique for saving material compared to the conventional corrugated cores and the superior structural performance for blast-loaded sandwich structures.

The trapezoidal (TZ) and triangular (T) corrugated core topologies were selected to highlight the blast-resistant performance of the new ribbon core topology. Applying the ribbon topology to the traditional corrugated core topologies improved their blast performance. The facing front plate's deflection of the trapezoidal corrugated ribbon core sandwich structure (TZRC) has been improved by 45.3% and by 76.5% for the back-plates deflection, while for the triangular ribbon corrugated core (TRC), the front plate's defection has been enhanced by 69.3% and by 112.1% for the backplate. The effect of various design parameters on the blast behavior of the Ribbon-Core Sandwich Panels (RCSPs) was investigated. Finally, based on the parametric study, the results of this study were recommended to be used as a guide for designing metallic ribbon sandwich structures with different protection levels.

Recommendations

The results have demonstrated the effectiveness of Hybrid multi-cell tubes and ribbon topology as a core layer for cladding and sandwich structures. This research presents a strong starting for many future lines of research that can arise from this work. The following topics could be pursued:

- Even though the application of numerical simulation helps reduce experimental work in terms of effort, time, and resources, especially under impulsive loads such as those caused by an explosion, new configurations need to be examined

experimentally.

- However, the new hybrid multi-cell tubes attain desired results by using four composite laminates, the effect of laminate number can be investigated.

- The effect of using filling material for the hybrid multi-cell tubes needs to be investigated.

- Another composite material such as GFRP and Kevlar can replace the CFRP.

- The ribbon topology can be applied for composite sheets instead of metals.

Appendix A- Permissions and copy rights clearance

1. Permission for publishing, "Hybrid Multi-Cell Thin-Walled Tubes for Energy Absorption Applications: Blast Shielding and Crashworthiness" Journal paper.

Rightslink® by Copyright Clearance Center

Copyright Clearance Center | RightsLink® | Home | Help | Email Support | Sign in | Create Account

Hybrid multi-cell thin-walled tubes for energy absorption applications: Blast shielding and crashworthiness

Author: Mahmoud Abada, Ahmed Ibrahim

Publication: Composites Part B: Engineering

Publisher: Elsevier

Date: 15 February 2020

© 2019 Elsevier Ltd. All rights reserved.

Journal Author Rights

Please note that, as the author of this Elsevier article, you retain the right to include it in a thesis or dissertation, provided it is not published commercially. Permission is not required, but please ensure that you reference the journal as the original source. For more information on this and on your other retained rights, please visit: https://www.elsevier.com/about/our-business/policies/copyright#Author-rights

BACK   CLOSE WINDOW

2. Permission for publishing, "Metallic Ribbon-Core Sandwich Panels Subjected to Air Blast Loading". Journal paper.

3. Permission for publishing, "Improving Blast Performance of Reinforced Concrete Panels Using Sacrificial Cladding with Hybrid-Multi Cell Tubes". Journal paper.

Copyright and Licensing